

**ESTIMATING THE TURBULENT SENSIBLE AND LATENT HEAT  
FLUXES BETWEEN THE ATMOSPHERIC BOUNDARY LAYER AND  
THE OCEAN SURFACE**

Elizabeth Kent

Oceanography Department M.Phil./Ph.D. Upgrading Report

September 1994

## **ABSTRACT**

<b>SECTION I</b>	<b>INTRODUCTION</b>	<b>I 1</b>
<b>1</b>	<b>BACKGROUND</b>	<b>I 1</b>
<b>2</b>	<b>THE PLAN</b>	<b>I 1</b>
2.1	Overview	I 1
2.2	Assessment of Present Bulk Formula Flux Estimates	I 2
2.3	Determination of Factors Affecting Boundary Layer Structure	I 2
2.4	Data sources for Flux Estimation	I 3
2.5	Comparison of Flux Estimates from Boundary Layer Structure with those from Bulk Formulae	I 4
2.6	Regions and Conditions of Applicability of Flux Estimates	I 4
<b>SECTION II</b>	<b>BACKGROUND AND LITERATURE REVIEW</b>	
<b>1</b>	<b>PREVIOUS METHODS OF FLUX CALCULATION</b>	<b>II 1</b>
1.1	Ship data - The Bulk Formulae	II 1
1.1.1	Bulk Formulae	II 1
1.1.2	Transfer Coefficient Schemes	II 1
1.1.3	Sampling and Classical Methods of Flux Calculation	II 3
1.1.4	Accuracy of the Fluxes	II 4
1.2	Satellite data - Latent Heat Flux	II 5
1.2.1	Measurement of Near-Surface Humidity	II 5
1.2.2	Direct Retrieval	II 6
1.3	Satellite Data - Sensible Heat Flux	II 6
1.4	Fluxes from Ocean heat budgets	II 6
1.5	Fluxes Deduced from Boundary Layer Structure	II 7
<b>2</b>	<b>STRUCTURE OF THE BOUNDARY LAYER</b>	<b>II 7</b>
2.1	Boundary Layer Processes	II 7
2.2	Observational studies of the inversion capped boundary layer	II 9
<b>3</b>	<b>ATMOSPHERIC BOUNDARY LAYER MODELS</b>	<b>II 9</b>
3.1	Lilly-type Slab Models	II 9
3.2	Stage and Businger Model	II 10
3.3	Higher-order Turbulence Closure Model	II 10
3.4	Met-Office Single Column Model	II 12

<b>4</b>	<b>MODEL INVESTIGATIONS RELATING BOUNDARY LAYER STRUCTURE TO SURFACE FLUXES</b>	<b>II 13</b>
4.1	Schubert (1976)	II 13
4.2	Kraus and Schaller (1978)	II 13
<b>SECTION III SUMMARY OF PROGRESS TO DATE</b>		
<b>1</b>	<b>BULK FORMULAE</b>	<b>III 1</b>
1.1	Errors in VOS data	III 1
1.2	Averaging Methods	III 3
1.3	Experimental Transfer Coefficients	III 3
<b>2</b>	<b>MODELLING</b>	<b>III 4</b>
2.1	<b>Koracin and Rogers Model</b>	<b>III 4</b>
2.1.1	Model Characteristics: Koracin and Rogers (1990)	III 4
2.1.2	Model Development	III 5
	2.1.2.1...Mixing coefficients	III 5
	2.1.2.2...Vertical Advection	III 5
	2.1.2.3...Gradient boundary condition for $\theta_l$	III 6
	2.1.2.4...Vertical motion profile	III 7
	2.1.2.5...Description of present model status	III 7
2.1.3	Model Resolution	III 8
	2.1.3.1...Vertical Resolution	III 8
	2.1.3.2...Time Step	III 9
	2.1.3.3...Effect of Resolution on the Surface Fluxes	III 9
2.1.4	Mean Profiles and Variability	III 9
2.1.5	Numerical Experiments: The Surface Fluxes	III 10
2.1.6	Summary	III 11
2.2	<b>Met Office Single Column Model</b>	<b>III 11</b>
<b>SECTION IV CONCLUSIONS AND FUTURE WORK</b>		
<b>1</b>	<b>SUMMARY</b>	<b>IV 1</b>
<b>2</b>	<b>CONCLUSIONS</b>	<b>IV 1</b>
<b>3</b>	<b>FUTURE WORK</b>	<b>IV 2</b>
<b>APPENDIX A - MONIN-OBUKHOV SIMILARITY THEORY AND TRANSFER COEFFICIENTS</b>		
		<b>A 1</b>
<b>APPENDIX B - TRANSFER AND VERTICAL MIXING COEFFICIENTS IN THE SCM</b>		
		<b>B 1</b>
<b>REFERENCES</b>		
		<b>R 1</b>



## **ABSTRACT**

The idea of relating surface fluxes and processes in the atmospheric surface layer to large-scale forcing has been introduced. Previous research has been reviewed to provide evidence that boundary layer structure and surface fluxes are linked.

Present methods of surface flux determination have been assessed and the best method of flux calculation chosen for use in validation of fluxes derived from boundary layer structure.

Two atmospheric boundary layer models have been implemented with a view to determining the surface flux dependencies by numerical experimentation; validation of the models has begun.

A plan for future work has been outlined with both short term and long term objectives.



## **SECTION I INTRODUCTION**

### **1 BACKGROUND**

Monthly mean surface fluxes are required to an accuracy of  $10\text{W/m}^2$  over the global ocean for use as forcing fields for general circulation models of the ocean and for heat budget studies. Fluxes are presently estimated using bulk formulae (described in Section II, 1.1) using input parameters of routine merchant ship meteorological observations from Voluntary Observing Ships (VOS); in many regions however the available data is too sparse to do this. In these data sparse areas some parameters may be remotely sensed using satellite instruments but at present not all the required parameters can be obtained in this manner. In addition the bulk formulae cannot be used over sea ice where the presence of leads means that fluxes vary rapidly over very short spatial scales.

It has been suggested (Taylor, 1984b) that the best way to define the fields globally may be a combination of in-situ data from the VOS and remotely sensed data interpolated with the aid of the output of numerical models. However this study will explore a different approach, the possibility of linking the surface fluxes to boundary layer structure in terms of variables which can be estimated using satellite remote sensing.

### **2 THE PLAN**

#### **2.1 Overview**

In order to test a new approach to the calculation of the surface turbulent heat fluxes the present methods of flux calculation must first be assessed. Estimates of mean surface fluxes vary greatly and the values obtained using experimentally determined transfer coefficients usually must be increased significantly when the overall heat balance of the ocean is considered. The best flux estimates to be used to verify the proposed method of flux determination need to be chosen.

This study aims to relate surface fluxes over the open ocean to the parameters that are available from satellite data. The idea that the marine atmospheric boundary layer (MABL) structure is coupled to the surface turbulent fluxes will be explored using numerical simulations of the MABL. If it can be shown that the fluxes are determined by the MABL structure it may be possible to parameterise the fluxes in terms of the large-scale forcing (see Section I, 2.3) that determines this structure. It is hoped that sufficiently accurate fluxes to give monthly mean values can be obtained in this way. The ability of the atmospheric models chosen to

numerically simulate the boundary layer processes will be tested by comparison with data collected over the North Atlantic from the JASIN experiment (Pollard et al., 1983), the SOFIA experiment (part of ASTEX, see ASTEX Operations Plan) and data from the Ocean Weather Ship Cumulus at Station "Lima". Using the models, a flux parameterisation will then be developed to enable the surface fluxes of sensible and latent heat to be estimated from large-scale parameters.

If fluxes can be parameterised in this manner, the data sources for input to flux calculation will be assessed. The possibility of obtaining the input data from microwave satellite measurements will be explored. The fluxes calculated from satellite data (either real or simulated) will then be compared to those predicted by the bulk formulae using VOS or buoy data as input.

If the fluxes cannot be adequately determined in this way progress may be possible by including an estimate of near surface humidity derived from passive microwave estimates of integrated atmospheric water content. Including the effect of boundary layer structure may improve estimates of the surface humidity from this source over the statistical approach of Liu and Niiler (1984).

Figure 1 is a flow chart summarising the steps that will be followed in this study. Further detail is given in the remainder of this Section.

## **2.2 Assessment of Present Bulk Formula Flux Estimates**

The flux estimation method will be initially tested in the North Atlantic Ocean; a region with good ship data coverage and where a well defined boundary layer structure is commonly found. The best bulk transfer coefficients will be selected following a comparison of schemes proposed in the literature (Kent and Taylor, 1994). Accuracy of ship data input to the bulk formula will be considered. The validity of using averaged input data with these formulae will also be investigated, this will be particularly important if the Liu and Niiler (1984) approach involving estimating monthly mean near-surface humidity from satellite integrated water content is followed.

## **2.3 Determination of Factors Affecting Boundary Layer Structure**

Numerical models of the atmospheric boundary layer will be used to determine the large-scale parameters that determine the size of the surface fluxes of sensible and latent heat. The performance of the models will be assessed by their ability to reproduce the evolution and steady state of the lower atmosphere in response to external forcing. As the models used are 1-dimensional (representing a single column of air above a sea surface temperature (SST)) an

important factor in their performance will be the manner in which effects of advection and horizontal gradients are incorporated. Two models have been initially considered; firstly a second-order turbulence closure model of the lower atmosphere as described by Koracin and Rogers (1990); and secondly the UK Meteorological Office 'Single Column Model' (SCM) which parameterises the turbulence in terms of a bulk Richardson number. The SCM has the advantage of including levels higher in the atmosphere but the kinetic energy balance is not treated explicitly. A simple 'slab-model' of the boundary layer may also be written and implemented. This would have the advantage of having simple relationships between the physical processes included and the resulting structure.

The performance of the models will be assessed initially in general terms by the ability to reach a physically plausible steady state. The dependence on the initial input profiles and setup must be examined to find sensitivities to internal parameters not predicted by the model. Once the model has proved to be robust and the optimum setup determined, the more rigorous test of comparison to field data can be made. The datasets presently available with radiosonde profiles are the JASIN dataset, ERS-1 validation cruise data, SOFIA experiment data, and the long timeseries of radiosonde data from OWS Lima. From these comparisons in different regions it will be determined whether the models have realistic dependencies on the input data and can correctly predict evolution of the boundary layer.

If the models prove to be internally consistent and are successful in reproducing observed boundary layer structure the relationships between boundary layer structure parameters and the surface fluxes will be investigated by numerical experimentation. Possible dependencies are on: SST and the time-history of the SST below the air column; the large-scale subsidence rate and profile of vertical motion; inversion height and strength; tropospheric lapse rate; and the wind speed. The aim will be to develop a model independent parameterisation.

By following this approach it should be possible to derive meaningful monthly mean flux estimates although instantaneous flux measurements are not likely to be accurate.

#### **2.4 Data sources for Flux Estimation**

Once the factors affecting the structure of the MABL and hence the surface fluxes have been determined, the availability and accuracy of the input data required will need to be assessed, as will the sensitivity of the method to those data limitations. It is expected that data will be remotely sensed; scatterometer data from ERS-1 may provide wind speed and trajectory data and also an estimate of large-scale vertical motion from the divergence of the wind vectors. It may be possible to use SeaSat scatterometer data with JASIN radiosonde data in initial validation of the flux estimates. Wind speed is also derived from altimeter

measurements but as the instrument is nadir view the footprint is small and data coverage will therefore be limited. The SST is also measured by satellites using radiometers, for example, the Advanced Very High Resolution Radiometer (AVHRR) and the Along-track Scanning Radiometer (ATSR). Both instruments measure the skin SST. Total water vapour content is presently available from passive microwave instruments from three satellites. Availability of other parameters will be considered once the dependencies have been found. Table 1 summarises the data sources that are likely to be required in this study.

## **2.5 Comparison of Flux Estimates from Boundary Layer Structure with those from Bulk Formulae**

Finally, the flux estimates will be compared for regions where conditions are compatible with those simulated in the model experiments and the data density for the VOS is high enough for good flux estimates to be made with the bulk formulae. If sufficiently accurate data is not available, the minimum requirements for data accuracy and both temporal and spatial coverages will be determined. Simulated scatterometer data could then be used to demonstrate the approach if necessary.

## **2.6 Regions and Conditions of Applicability of Flux Estimates**

If comparisons with existing methods are favourable then fluxes can be determined for regions identified with sparse VOS data coverage but where similar conditions exist to the test areas in the North Atlantic.

## SECTION II BACKGROUND AND LITERATURE REVIEW

### 1 PREVIOUS METHODS OF FLUX CALCULATION

#### 1.1 Ship data - The Bulk Formulae

##### 1.1.1 Bulk Formulae

Surface fluxes of sensible and latent heat have traditionally been calculated from the bulk formulae (equations 1) which empirically relate the fluxes to the air-sea temperature and humidity difference, see for example Roll (1965).

$$\left. \begin{aligned} H_S &= c_p \rho C_T U (T_{sb} - T) \\ H_L &= L \rho C_E U (q_s - q) \end{aligned} \right\} \quad (1)$$

where  $H_S$  is the sensible heat flux,  $H_L$  is the latent heat flux,  $c_p$  is the specific heat of air at constant pressure,  $\rho$  is the density of air,  $U$  is the wind speed,  $T_{sb}$  is the bulk sea surface temperature, (SST),  $T$  is the air temperature,  $L$  is the latent heat of vaporisation,  $q_s$  is the specific humidity of the air at the sea surface and  $q$  is the specific humidity of air at the measurement height. The transfer coefficients for sensible heat,  $C_T$ , and latent heat  $C_E$ , are determined empirically from air-sea interaction experiments and are functions of wind speed, measurement height and atmospheric stability defined in terms of Monin-Obukhov similarity theory, see Appendix A.

##### 1.1.2 Transfer Coefficient Schemes

Bunker (1976) tabulated transfer coefficients as a function of wind speed and air-sea temperature difference following a critical review of studies up to 1974. He chose  $C_T$  to be equal to  $C_E$  arguing that the sensible heat contribution to the total heat budget is small and errors thus introduced would also be small. These transfer coefficients were intended for use with individual ship observations but Hsiung (1986) used them with monthly mean 5° averages. Bunker then considered the relationship between transfer coefficients appropriate to be used with VOS data as opposed to the data from the towers and buoys used in the experiments considered. The results of BOMEX (Holland, 1972) indicated that the coefficients should be increased by 10%, which was assumed to account for flow distortion and measurement height. Bunker's tabulated transfer coefficients are plotted in Figures 2a and 2b.

Isemer and Hasse (1987) updated the coefficients of Bunker described above to include more recent field data, then applied an adjustment to the fluxes using an inverse calculation with the meridional heat transport estimates of Bryden and Hall (1980) as a constraint. The study was repeated with further constraints by Isemer et al. (1989), but the results for latent and sensible heat remained unchanged. The coefficients are plotted in Figures 2c and 2d. As with Bunker's, these coefficients are intended for use with individual ship reports but Isemer and Hasse (1987) used COADS monthly mean values then adjusted for the errors introduced by this by multiplying values by the ratio of Bunker's estimates to a calculation using Bunker coefficients with monthly mean data.

Large and Pond (1981;1982) derive a set of transfer coefficients based on data from a tower and from research ships. Both the dissipation and eddy correlation techniques were used to estimate the fluxes which were then related to bulk parameters. Stability is described by Monin-Obukhov stability theory, Appendix A. Figures 2e and 2f show the coefficients; the difference between the 'neutral' values of  $C_{TN}$  for stable and unstable cases can be seen.

Oberhuber (1988) although quoting the method of Large and Pond (1981;1982) makes changes to the form of the transfer coefficients which significantly affects their wind speed dependence (Figures 2 g and h). Instead of the linear relationship of  $C_{DN}$  to wind speed used by Large and Pond (1981), the Charnock relationship is used (Appendix A, equation A9) with a Charnock constant of 0.032 (the value used in the operational T-21 model at the Max-Planck Institut, which is much larger than values commonly used). The COADS monthly mean summaries were used as input data (Wright, 1988)

Smith (1988;1989) reviewed measurements of the fluxes and presents transfer coefficients again based on Monin-Obukhov stability theory (Appendix A). A Charnock constant of 0.011 is used.  $C_E$  is found from  $1.2 \times C_T$ . Coefficients are plotted in Figures 2i and j.

Liu et al. (1979) decided to base their parameterisation on the skin temperature of the ocean (see eg Robinson et al., 1984) rather than the bulk SST used in all the other schemes described in this subsection. The skin SST is measured by radiometer and is the parameter that is remotely sensed (although algorithms for obtaining the SST have been based on the bulk values for validation reasons). The formulation therefore would seem to be unsuitable for use with VOS data although Esbensen and Kushnir (1981) used it without adjustment. The Liu et al (1979) coefficients are derived by consideration of molecular effects at the air-sea interface, identified as a 'bottle-neck' in the transfer process. The surface relation is matched to the outer profiles in a transition zone. Figures 2k and 2l show the coefficients; the skin SST has been estimated from parameters reported by the VOS using the method proposed by Hasse (1970).

### 1.1.3 Sampling and Classical Methods of Flux Calculation

Following a study of the different flux calculation methods it was found that an important factor in the accuracy of the flux estimates was the averaging technique used. This has important implications for some methods of flux determination using satellite data and is further discussed in Section III, 1.2.

Sensible and latent heat fluxes can be calculated by either the 'sampling method'; the fluxes are calculated from individual ship reports and are then averaged to give mean values; or the 'classical method'; the mean fluxes are calculated directly from mean values of the bulk parameters. Several papers have been published assessing the validity of using the classical method (Esbensen and Reynolds, 1981; Fissel et al., 1977; Simmonds and Dix, 1989; Weare, 1989; Weare and Strub, 1981).

The validity of the approximation relies on the covariances between the wind speed, transfer coefficient and air-sea temperature or humidity differences and their triple covariance being small or if not small, approximately and consistently cancelling. It is therefore assumed that equations 2 can be replaced by equations 3, Simmonds and Dix (1989) assessed this approximation by comparing fluxes calculated from output of a general circulation model and concluded that the fluxes differ by less than 10W/m<sup>2</sup> at most latitudes in the two months studied.

$$\begin{aligned}
 \overline{H_s} &= c_p \rho \overline{C_T U (T_{sb} - T)} \\
 &= c_p \rho \left( \overline{C_T U (T_{sb} - T)} + \overline{C_T U' (T_{sb} - T)} + \overline{U C_T' (T_{sb} - T)} + \overline{(T_{sb} - T) U' C_T'} + \overline{C_T' U' (T_{sb} - T)} \right) \\
 \overline{H_L} &= L \rho \overline{C_E U (q_s - q)} \\
 &= L \rho \left( \overline{C_E U (q_s - q)} + \overline{C_E U' (q_s - q)} + \overline{U C_E' (q_s - q)} + \overline{(q_s - q) U' C_E'} + \overline{C_E' U' (q_s - q)} \right)
 \end{aligned}
 \tag{2}$$

$$\begin{aligned}
 \overline{H_s} &\approx c_p \rho \overline{C_T U (T_{sb} - T)} \\
 \overline{H_L} &\approx L \rho \overline{C_E U (q_s - q)}
 \end{aligned}
 \tag{3}$$

The results of any study are obviously dependent on the choice of transfer coefficient scheme used as the covariance of the coefficient with wind speed and air-sea temperature (or humidity) difference appears in terms 3 and 4 in equations 2 and the triple covariance in term 5. Budyko (1974), although stating that stability effects were important in determining the surface fluxes, calculated the error involved in using mean values in the bulk formulae was ~7% for monthly mean values.

#### 1.1.4 Accuracy of the Fluxes

Table 2 shows in summary form a survey of the available published estimates of the surface fluxes and heat budgets. As well as using different formulations for the transfer coefficients (see Section II, 1.1.2) ad hoc corrections are applied by some authors to the VOS data. Also the resolution of the fluxes calculated varies between the studies as does the amount of filtering applied to the data.

Blanc (1985) considered the variation of the fluxes at OWS C in the North Atlantic due to the transfer coefficient scheme used. He compared 10 schemes, including Bunker (1976), Liu et al (1979) and Large and Pond (1981;1982). Figures 3a and 3b show the maximum and mean variation of the 10 schemes plotted against the 'consensus' value. Typical uncertainties are seen to be ~20% for both sensible and latent heat fluxes with maximum values of 70% for the modal sensible heat flux and 45% for latent heat.

Blanc (1986) estimated the effects of inaccuracies of weather-ship data on the bulk-derived fluxes by considering the climate around OWS C. Sensor accuracy and ship-induced distortions are considered separately. An error analysis is performed, applying published error estimates to the statistical distribution of input parameters to the bulk formulae. Figures 3c-f show the average errors in sensible and latent heat flux due to sensor inaccuracies and ship distortions. Transfer coefficient schemes used include Liu et al (1979) and Large and Pond (1981;1982). Liu (1987) has however questioned the results reported from the implementation of the Liu et al (1979) scheme for latent heat and suggests that the error estimate should be more similar to the other schemes (Figures 3d and 3f). Liu also comments that the method of presenting the error as a function of the flux modulus is misleading due to the different behaviour of the fluxes in stable and unstable conditions.

Studies have found (eg Bunker, 1982) that an increase in transfer coefficients is required to balance the heat budget; this has been justified by the effects of ship avoidance of high wind speeds. However Quayle (1980) suggested that the increased number of data points resulting from the slowing down of ships in bad weather would compensate for any statistical differences introduced by ship weather routing. In theory the existence of a fair-weather bias might be determined by comparison of ocean weather ship (OWS) and VOS wind speed data. The OWS data should define the wind climate at the station and the VOS data can then be tested against this climate. However it would be difficult to separate errors in determining the winds from the effects of a fair weather bias. For example, the conversion scales for visual winds (WMO1100, CMM IV; WMO (1970) and Kaufeld (1985)) have been derived by comparison of anemometer and visual wind speed distributions, and any fair-weather bias will therefore have been effectively removed from the visual data.

## 1.2 Satellite data - Latent Heat Flux

### 1.2.1 Measurement of Near-Surface Humidity

If the bulk formulae are to be used to calculate the mean latent heat flux over the ocean from satellite data the wind speed, sea surface and near surface humidity need to be determined. Neutral stability is assumed. Taylor (1984a) summarised the accuracy required for each parameter and that obtained from satellite measurements. Wind speed can be determined from scatterometer, altimeter or microwave radiometer and should be sufficiently accurate for flux determination. Sea surface humidity is calculated from the SST assuming saturation of the air, SST can be measured by satellite sensors to better than  $1^{\circ}\text{C}$  (see Table 1) which is close to the requirement for midlatitude regions. The near surface humidity poses the main problem and is commonly estimated from total precipitable water. Total precipitable water is required as a correction to radiometer measurements and is derived from the absorption of radiation in different wavelengths (for Nimbus-7: 18, 21 and 37 GHz, Wagner et al, 1990). The total precipitable water can then be related to surface humidity using relationships derived from statistical analysis of radiosonde humidity profiles.

Taylor (1982) considered the relationship between near surface humidity and total precipitable water using JASIN radiosonde data; he concluded that the errors were likely to be  $30\text{W}/\text{m}^2$  in midlatitudes and  $60\text{W}/\text{m}^2$  in the tropics. He suggested that combinations of satellite, in situ and model data should be used to give the best flux estimate. Liu (1984) found a scatter of  $35\text{W}/\text{m}^2$  between satellite estimates of monthly mean latent heat flux and those from ship data in the Western North Atlantic. The near surface humidity was related to the integrated water vapour using a statistical regression of the integrated water vapour and the humidity at the lowest sounding level for radiosonde measurements at four stations. Liu and Niiler (1984) extended the study to the tropical Pacific and concluded that globally the contribution to the error in the monthly mean latent heat flux from the near surface humidity alone was  $20\text{W}/\text{m}^2$ . Other studies have looked at the errors in individual measurements of near surface humidity. Schulz et al. (1993) however find an error for the near surface humidity equivalent to  $30\text{W}/\text{m}^2$  for the SSM/I on the DMSP satellite. Schulz (1993 unpublished manuscript) combined SSM/I data with AVHRR data and obtained a standard deviation of  $30\text{W}/\text{m}^2$  for the latent heat flux. Wagner et al. (1990) found a retrieval accuracy corresponding to an error in the latent heat flux of  $23\text{W}/\text{m}^2$  for the North Atlantic using data from the SMMR on Nimbus-7.

The problem of using averaged data with the bulk formulae as described in Section II, 1.1.3 must also be addressed when using this method to calculate the heat fluxes.

### 1.2.2 Direct Retrieval

Liu (1990) looked at direct retrieval of the latent heat flux from the Nimbus/SMMR brightness temperatures. The algorithm was based on four months ship data. Latent heat fluxes were predicted for the global ocean for one month using SMMR data with qualitative success but further validation is required. This method of flux determination from satellite data avoids the errors associated with averaged data which are inherent in the method used by Liu and Niiler (1984).

### 1.3 Satellite Data - Sensible Heat Flux

Attempts have been made to relate near surface air temperature to near surface humidity by assuming a constant relative humidity (Liu, 1990). There are however variations in temperature which are not reflected by changes in specific humidity and this approach does not seem promising. Liu suggests that the determination of sensible heat flux may be possible by combining future improved atmospheric sounder data with boundary layer parameterisation.

### 1.4 Fluxes from Ocean heat budgets

Bunker et al. (1982) used VOS data to estimate climatological values of air-sea fluxes in the Mediterranean and Red Seas. The heat budget was balanced by adjusting the net longwave radiation and by increasing the latent heat flux transfer coefficients by 10%; although experimental results (Friehe and Schmitt, 1976) suggested that the coefficient values used were already too high. The increased coefficients were justified on the basis of errors in the ship data and ship avoidance of high wind speeds. Garrett et al. (1993) argue strongly against changing latent heat flux values without consideration of the water budget. In this study the heat and water budgets are balanced using transfer coefficients for sensible and latent heat fluxes from Smith (1988;1989)<sup>1</sup>. The imbalance in the heat budget was removed by the reduction of the insolation; they also account for absorption of radiation by aerosols which is likely to be an important factor close to land.

Isemer et al. (1989) use direct estimates of ocean heat transport by Bryden and Hall (1980) and Hall and Bryden (1982) to constrain the surface fluxes in the North Atlantic. This results in an increase of about 5% in the transfer coefficients above the values they derived

---

<sup>1</sup>Section III, 1.3 contains a comparison of mean fluxes and transfer coefficients for the Smith and Bunker schemes.

from the literature. There is no consideration of the water budget when revising the latent heat flux.

Carissimo et al. (1985) calculate the meridional heat transport in the oceans as a residual of the net radiation balance at the top of the atmosphere and the atmospheric transport rate. This results in an estimate of meridional oceanic heat transport of 3.5 PW at 25°N, 50% greater than Hall and Bryden (1982); this would decrease estimates of air-sea heat transfer. The estimated error ( $\pm 1.5$ -2 PW) however encompasses the Hall and Bryden value.

The FLORENCE programme (Gaspar et al., 1990; Miller, 1981) is an attempt to indirectly estimate the surface turbulent fluxes from the heat budget of the upper oceanic boundary layer using satellite estimates of SST, surface insolation, wind stress and net infrared flux. Data are combined with an ocean boundary layer model using inverse analysis. The ability of the ocean model to correctly predict the thickness of the ocean mixed layer has an important effect on the resulting estimate of the fluxes and advection also needs to be accounted for.

### **1.5 Fluxes Deduced from Boundary Layer Structure**

Chou and Atlas (1982) estimated the heat fluxes during cold air outbreaks using the atmospheric model of Stage and Businger (1981a;1981b). The Stage and Businger model is described in Section II, 3.2. Chou and Atlas related the mean sensible heating in the cloud-free region to the distance from the shore to the first cloud formation and the difference between the land-air temperature and the SST. Latent heat was similarly calculated from the cloud-free path and the land-air and the sea surface specific humidities. The results were related to the atmospheric stability (lapse rate at the shore) which was included via a further parameter, the square of the downwind slope of the boundary layer depth. Fluxes were calculated using an Advanced Very High Resolution Radiometer (AVHRR) image and were compared to those calculated from the bulk formulae using buoy and coastal station data. For the case chosen the fluxes from both methods were identical.

## **2 STRUCTURE OF THE BOUNDARY LAYER**

### **2.1 Boundary Layer Processes**

The boundary layer will be defined as the region of turbulent mixing in the lower atmosphere. Extending from the surface to some height within the boundary layer is the Ekman layer where the wind deviates from its frictionless value. There is a region near the surface where the fluxes are nearly independent with height. This is the surface layer where

the Monin-Obukhov length scale defines the height at which buoyant production equals mechanical production (Tennekes, 1973).

Above much of the ocean is moist air under a strong inversion caused by subsidence of dry upper air over a well mixed region near the sea surface. This type of MABL is often topped by a stratocumulus cloud layer (Stull, 1988). Figure 4 shows diagrammatically some of the processes occurring in this type of boundary layer along with idealised profiles of total water mixing ratio ( $q_t$ ), equivalent potential temperature ( $\theta_e$ ) and potential temperature ( $\theta$ ) for a well mixed marine boundary layer. Processes that are sources and sinks of heat are indicated. Driedonks and Duynkerke (1989) summarise these processes and their important effects.

Longwave radiation effects are concentrated in a shallow layer (about 50 m thick) at the cloud top. Cloud-top radiational cooling is an important source of convective turbulent mixing, leading to entrainment of drier air from the free atmosphere. This can cause evaporation which leads to further cooling. Cooling at the cloud top may however result in condensation and therefore latent heat release that offsets the heat loss and can possibly produce drizzle. In addition there is weak longwave heating at the cloud base.

Short wave heating is diurnal and affects a deeper layer of the cloud, again leading to the possibility of convection. It has been suggested, for example by Nicholls (1984), that the cloud can become destabilised due to the longwave and short wave radiation and become decoupled from the mixed layer below and hence from the source of moisture at the sea surface. Dry air entrained at the cloud top then only mixes within the cloud layer rather than down to the sea surface causing breakup of the cloud deck.

The surface flux of latent heat is the main source of water vapour in the boundary layer. Advection of moister air may also cause the humidity to increase. Both the latent and sensible heat fluxes are sources of buoyancy and turbulence in the surface layer. The variation of the surface fluxes with bulk parameters is described in Section II, 1.1.1.

When warm, dry air is entrained at the cloud top turbulent kinetic energy (tke) is used to bring the warm dry air into the cloud, increasing the potential energy of the air. The amount of entrainment depends on the kinetic energy available (from turbulence produced by wind shear, radiative effects, condensation and surface fluxes for example) and the inversion strength (which defines the amount of potential energy required for the entrainment). The spectrum of length and velocity scales of the turbulence is also important. Additionally the entrainment of dry air may lead to the cloud becoming unstable as the entrained air is cooled by evaporation of the cloud droplets as the air mixes. If the inversion strength is such that  $\theta_e$  does not increase with height at the cloud top the parcel can be cooled to such an extent that it sinks through the cloud. This results in large entrainment rates and the cloud is broken up due

to the mixing of the dry air into the cloud. If wind shear in the boundary layer results in Kelvin-Helmholtz instability this may lead to entrainment at the cloud top.

Subsidence of the overlying dry air will cause the inversion to descend and the cloud will tend to dissipate. The cloud however may remain if the inversion height is maintained by the entrainment of warm, dry air at the cloud top and the humidity is maintained by sufficient evaporation at the sea surface to offset the drying effect of the subsidence.

## 2.2 Observational studies of the inversion capped boundary layer

Stull (1988) tabulates the main field programs that gathered boundary layer data along with the measurements made. The marine studies of interest are BOMEX (Holland, 1972), GATE (the Global atmospheric research programme Atlantic Tropical Experiment), (Keuttner and Parker, 1976), JASIN (Joint Air-Sea Interaction Experiment), (Pollard et al., 1983) and SOFIA (Surface Ocean Fluxes and Interaction with the Atmosphere), (Kent and Pascal, 1992).

More detailed descriptions of observational marine boundary layer studies up to 1983 can be found in Nicholls (1983) and Rogers (1983).

## 3 ATMOSPHERIC BOUNDARY LAYER MODELS

### 3.1 Lilly-type Slab Models

Lilly (1968) used a slab-type model to relate features of a radiatively active turbulent cloud layer over the sea under a strong subsidence inversion. He considered both dry (aerosols, no phase change) and wet clouds, for the wet clouds the wet-bulb potential temperature must increase upwards in the inversion or cloud top entrainment instability can lead to complete erosion of the cloud.  $\theta$  and total water are constant through the mixed layer which contains both clear air and cloud below an inversion. The height of the cloud base depends on the difference in the surface humidity from its saturation value. Motions within the cloud are assumed to be saturated. The change in mixed layer humidity and  $\theta$  with time depends on the difference between the surface flux and the cloud top flux and the depth of the mixed layer. The depth of the mixed layer in turn depends on the subsidence, cloud top fluxes (including net outward radiation) and the inversion strength. Entrainment of air from above the inversion into the turbulent mixed layer is controlled by the subsidence, fluxes, pressure, temperature and the geometry of the mixed and cloud layers. Closure of the energy budget follows Ball (1960) and assumes that the buoyancy flux can be partitioned into a part that produces  $\tau_{ke}$  (a fraction of which is dissipated) and a part that destroys  $\tau_{ke}$ . The ratio of production to dissipation,  $k$ , leads to 'maximum' and 'minimum' entrainment conditions.

Minimum entrainment occurs when the dissipation and transport of tke are negligible. There is no region of net dissipation, all dissipation occurs in the region of generation. The maximum entrainment condition occurs when the regions of tke generation are balanced by regions of tke consumption. Tke is consumed when the potential energy of the air is increased by entrainment of warm air across the inversion. Tke is produced by the surface turbulent fluxes. Closure is necessarily by the buoyancy term only as the model contains no dynamics.

### **3.2 Stage and Businger Model**

This model is a more sophisticated slab model than that of Lilly described in the previous subsection. The model is formulated in terms of  $\theta_e$  and  $q_t$  which are assumed to be constant in the mixed layer and to have a sharp jump in their vertical profiles at the top of the mixed layer. The depth of the mixed layer is another dependent variable. The evolution rate of  $\theta_e$  depends on the depth of the mixed layer, surface sensible heat flux, the entrained flux at the top of the mixed layer and the cloud top and cloud base radiation. The change in  $q_t$  similarly depends on the mixed layer depth, surface latent heat flux and the entrained moisture flux. The depth of the mixed layer depends on the subsidence rate and the entrainment rate.

Transfer coefficients for the surface heat fluxes depend on air-sea virtual temperature differences but have no wind speed dependence; it is argued that although the surface roughness increases with wind speed, increased mixing makes the surface layer less unstable. Only unstable conditions are considered.

Divergence is assumed to be independent of height within the boundary layer. The entrainment rate is calculated assuming that the energy required to entrain air against the buoyancy force comes from the tke of the boundary layer. The tke budget is considered to be composed of a shear production term (assumed small except near the sea surface), buoyant production, dissipation and the rate of tke loss to internal gravity wave production. It is argued that the only important terms are the buoyant production and the dissipation; the change in tke storage is assumed negligible. The closure assumption is that dissipation is a fixed fraction of production but that consumption need not occur within the region of production. The remainder of the tke (assumed to be 20%) is available for entrainment.

### **3.3 Higher-order Turbulence Closure Model**

This subsection will outline a 1-dimensional, second-order turbulence closure model as described by Koracin and Rogers (1990) and Rogers and Koracin (1992) and closely based on Yamada (1978). The model is described as level 2.5 as advection and diffusion terms are assumed to be second order and are neglected in the second-moment equations. The model

equations are applied to a non-viscous, hydrostatic incompressible fluid. The tke equation (equation 4) is solved and the vertical exchange coefficients calculated using equation 5 (see following text for notation used):

$$\frac{1}{2} \frac{Dq^2}{Dt} = \frac{\partial}{\partial z} \frac{1}{2} \left( q_1 S_q \frac{\partial q^2}{\partial z} \right) - \overline{u'w'} \frac{\partial U}{\partial z} - \overline{v'w'} \frac{\partial V}{\partial z} + \beta g \overline{w'\theta'_v} + \frac{q^3}{\lambda_1} \quad (4)$$

$$\begin{aligned} -\overline{v'w'} &= K_m \frac{\partial V}{\partial z} \\ -\overline{w'\theta'_1} &= K_h \frac{\partial \theta_1}{\partial z} \\ -\overline{w'q'_t} &= K_h \frac{\partial q_t}{\partial z} \end{aligned} \quad (5)$$

where  $K_m$  and  $K_h$  are calculated using the kinetic energy and include the effects of stability and mixing (see Yamada 1978 and Yamada 1979 for details).

Algebraic equations for the time evolution of wind speed (equations 6), liquid water potential temperature ( $\theta_1$ , equation 7) and  $q_t$  (equation 8) are solved. The mixing length formulation is from Blackadar (1962), (equations 9).

$$\begin{aligned} \frac{DU}{Dt} - fV &= -\frac{1}{\langle \rho \rangle} \frac{\partial P}{\partial x} + \frac{\partial}{\partial z} \left( K_m \frac{\partial U}{\partial z} \right) \\ \frac{DV}{Dt} + fU &= -\frac{1}{\langle \rho \rangle} \frac{\partial P}{\partial y} + \frac{\partial}{\partial z} \left( K_m \frac{\partial V}{\partial z} \right) \end{aligned} \quad (6)$$

$$\frac{D\theta_1}{Dt} = \frac{\partial}{\partial z} \left( K_h \frac{\partial \theta_1}{\partial z} \right) + \sigma_r \quad (7)$$

$$\frac{Dq_t}{Dt} = \frac{\partial}{\partial z} \left( K_h \frac{\partial q_t}{\partial z} \right) \quad (8)$$

$$\lambda = \frac{k(z+z_0)}{1+k(z+z_0)/A} \quad ; \quad A = \frac{cu_*}{f} \quad (9)$$

where  $q^2/2$  is the tke,  $S_q$  is a stability function,  $U$  and  $V$  are the horizontal wind components,  $w$  the vertical wind speed, and  $u'$ ,  $v'$  and  $w'$  are the fluctuating components of the wind.  $P$  is the air pressure,  $\beta$  is the thermal expansion coefficient ( $=1/\langle \theta \rangle$  where  $\langle \rangle$  denotes a horizontal average),  $K_m$  and  $K_h$  are the vertical exchange coefficients.  $\sigma_r$  is the net radiative heating rate.  $c$  is a constant and is typically taken as 0.3,  $f$  is the coriolis parameter,  $g$  the acceleration due to gravity and  $\lambda$  is the mixing length ( $\lambda_1 = 16.6\lambda$ ).  $u_*$  is the friction velocity, see Appendix A.

Surface fluxes are treated using Monin-Obukhov similarity theory, see Appendix A: the fluxes are related to gradients in the surface layer.

The cloud parameterisation is probabilistic, based on Gaussian distributions of water vapour mixing ratio and liquid water potential temperature within each cloudy layer (Mellor 1977). Divergence of the net longwave radiative flux and the distribution of shortwave heating within the cloud are described in Rogers and Koracin (1992).

### **3.4 Met-Office Single Column Model**

The UK Met. Office Single Column Model (SCM) contains the physics of the normal weather forecast model (the Unified Model) but is run at a single grid point. Large-scale forcing effects are simulated either statistically from climate datasets or using measured increments from specific observational datasets. Observational forcing has been used in the present study.

The model (when run over a sea point) predicts the horizontal wind components,  $\theta$ , specific humidity, cloud water and ice, surface pressure, boundary layer depth, sea surface roughness and the convective cloud amount, its base and top. The model is formulated in terms of 'cloud conserved variables'; the liquid/frozen water temperature and the total water content. Model equations are from White and Bromley (1988).

In the boundary layer stability is defined in terms of a bulk Richardson number which avoids the iteration required to calculate the Monin-Obukhov length (which depends on the fluxes which depend on the stability). Appendix B details how the surface transfer coefficients are derived in terms of  $Ri_B$ . The heating and moistening due to the divergence between the surface fluxes and the fluxes at the top of the boundary layer are linearly distributed within the boundary layer; this is to allow mixing within the model which is not directly due to local gradients, non-local fluxes. The mixing due to local gradients (as in equations 10 and 11) is then performed using mixing coefficients based on  $Ri_B$  and a Blackadar formulation for the mixing length, see previous subsection. The form of the vertical mixing coefficients is described in Appendix B. Near the surface a modified mixing length is used to improve the accuracy of the finite difference scheme in the region where profiles have a logarithmic form. The depth of the boundary layer is defined by the lowest model interface where  $Ri_B > 1$ . The possibility of deepening is then tested by considering  $Ri_B$  across the current boundary layer top. If the boundary layer can be deepened the process is repeated until no further expansion is possible. The sea surface roughness parameterisation is by the Charnock relation (see Appendix A) with a Charnock constant,  $a$ , of 0.012.

The convection scheme is applicable to all types of moist and dry convection. A single cloud model is used to represent an ensemble of convective clouds with different characteristics and extents. The model atmosphere is tested from the bottom level upwards until a certain amount of excess buoyancy is found, an air-parcel then rises, entraining environmental air and detraining cloudy air until equilibrium is attained or the parcel is completely detrained. In each layer a proportion of the parcel (representing a buoyant plume) is assumed to have reached zero buoyancy and to completely detrain; the proportion being set by allowing the remainder of the parcel to have the required amount of buoyancy to be allowed to rise further.

#### **4 MODEL INVESTIGATIONS RELATING BOUNDARY LAYER STRUCTURE TO SURFACE FLUXES**

##### **4.1 Schubert (1976)**

Schubert (1976) used a model based on Lilly's model (see Section II, 3.1) to examine the sensitivity of the boundary layer to large-scale divergence, SST, and the closure assumption. The transfer coefficient used for surface fluxes is constant. Schubert used a weighted average of the maximum and minimum entrainment conditions and investigated the sensitivity to the entrainment parameter  $k$ .  $k=1$  corresponds to the maximum entrainment condition. Figure 5 shows the dependence of the fluxes on the entrainment parameter which defines the proportion of  $k\epsilon$  which is available to drive entrainment. The latent heat flux can be seen to increase as the amount of entrainment increases and the sensible heat flux to decrease. This is consistent with the incorporation of warm, dry air into the boundary layer. The magnitude of changes to both fluxes decreases as the divergence and hence the subsidence increase.

##### **4.2 Kraus and Schaller (1978)**

Kraus and Schaller (1978) use a model similar to that used by Schubert (1976) described above and assume that the entrainment parameter is 0.2. Their work shows that if the MABL can be adequately approximated by a slab model that the steady state surface fluxes are functions of the surface wind speed, the SST, the gradient of SST along the trajectory of the surface wind and the difference between the surface temperature and an extrapolation of the temperature gradient above the inversion to the sea surface ( $T_{SS}-T_{S+}$ ). In this study the tropospheric lapse rate was held constant, leaving ( $T_{SS}-T_{S+}$ ) to be simply dependent on the temperature difference across the inversion and the height of the inversion. Figure 6 shows the flux dependencies found by this study.



## **SECTION III SUMMARY OF PROGRESS TO DATE**

### **1 BULK FORMULAE**

#### **1.1 Errors in VOS data**

The errors present in VOS data were assessed using data from the VSOP-NA project (Kent et al., 1993) where a subset of VOS meteorological reports were compared with the output of an atmospheric numerical model. Although the model output contains errors itself and cannot represent small-scale effects it was assumed that consistent trends in the mean differences between ship and model parameters were meaningful. If it was then possible to relate the trends in the differences to model-independent effects (for example the type of instrumentation used on the ships) then an error in the ship data has been identified. Table 3 gives percentage errors in the sensible and latent heat fluxes resulting from each of the errors identified. The major sources of error are summarised in the remainder of the subsection.

##### a) Effect of solar radiation on VOS measurements of air temperature

The difference between the ship measurement and the model prediction was strongly correlated with incoming solar radiation and also correlated with the relative wind speed over the ship at the time of the observation. This difference could be reduced to a constant offset over the full solar radiation range by applying a formula derived from linear regression of the temperature differences for different wind speed ranges. The method is described in Kent et al. (1994). Figure 7 shows air temperature measurements from the VSOP-NA experiment before and after correction for solar radiation effects. Application of this correction to VSOP-NA data was found to increase the mean annual flux of sensible heat by over 15% (Kent and Taylor, 1994) and to slightly increase the latent heat (~1%) due to the effect on stability.

##### b) Beaufort scale conversion

About 50% of the VOS wind reports are visual estimates (Kent and Taylor, 1991) which have been converted to speeds using a 'Beaufort' wind scale. The data in many flux atlases is based on the WMO1100 scale (WMO, 1970) which is known to give wind speeds too high above force 8 and too low below force 8. The CMM scale (same reference) is thought to give a more accurate representation of the wind speed distribution. Table 3 shows that the use of the CMM scale increases the total flux by 5%.

##### c) Height correction

Height correction is the major factor acting to decrease flux estimates (the other factor being the overestimate by engine intake methods of SST, see below). The bulk formulae

require input data at a specific measurement height (either 10m or 20m) and measured at other heights should be height corrected using, for example, the similarity theory outlined in Appendix A.

d) SST correction

It was found (Kent et al., 1993) that VOS SST observations from engine intake thermometers were consistently 0.35°C higher than those reports using hull sensors or bucket measurements. Removal of this bias from the data reduced the total flux by 4%.

e) Dewpoint correction

Differences were found in dewpoint measurements between screen and psychrometer observations. Consideration of the likely factors indicated that lower measurements of dewpoint (psychrometer) were more likely to be correct (as the errors, eg drying out or contamination of the wick, would tend to increase the wet-bulb measurement towards the dry bulb). The distribution of screen-measured dewpoints was therefore corrected to look like that of the psychrometers. The sensible heat flux is only affected by the effect of water vapour on stability but the error in the total flux was still 8%, Table 3.

f) Effect of fair-weather bias

The effect of fair-weather bias on the wind-speed and flux distributions was assessed in the following way to avoid issues relating to the Beaufort Scale conversion (see Section II, 1.1.4), whilst using all available observations. Two distributions of wind reports were compared. The first distribution was the full set of wind speeds reported by the OWS Cumulus which occupies weather station LIMA (57°N 20°W). The second distribution was the subset of wind speeds reported by the OWS Cumulus corresponding to sample times when there was a VOS wind speed report from the 5° by 5° area around LIMA. If more than one VOS report was received at the same time from this area, the Cumulus report was included in the distribution the appropriate number of times. The two sets of data were compared to determine whether the VOS sampled the wind climate at LIMA in the same way as the OWS Cumulus. Figure 8a shows the distribution of wind speed occurrences. Using a  $\chi^2$ -test the data sets were found to be the same to within 97.5% confidence limits.

The effect of any 'fair-weather bias' which did exist would only be significant for the mean sensible and latent heat fluxes if the total flux carried in the high wind speed part of the flux distribution were appreciable. Figure 8b shows the cumulative distribution of the total proportion of flux occurring below given values of the OWS Cumulus wind speed, calculated using the transfer coefficients of Smith (1988;1989). Comparing Figures 8a and 8b it can be seen that the 10% of winds over 30 knots carried 25% of the latent heat flux and 30% of the sensible heat flux, a significant fraction. However Figure 8b shows that the percentage difference between the total flux from all OWS Cumulus data, and the total flux from OWS

Cumulus data when there were VOS in the region of LIMA, was small. The difference in the mean flux between the full OWS Cumulus data set and the 'VOS subset' was less than 1% for sensible heat and less than 2% for latent heat.

Thus, from this data, there does not appear to be a significant re-routing of ships during periods of high wind speed in the area around LIMA. It therefore does not seem likely that a 'fair-weather bias' affected the mean fluxes significantly, at least in the region of LIMA.

## 1.2 Averaging Methods

The major variations in the transfer coefficients with wind speed and air-sea temperature difference occur at low wind speed (see Figures 2) although some schemes have wind speed dependence at high wind speeds. Figure 9 shows the total heat flux from the VSOP-NA data calculated using the Smith (1988;1989) transfer coefficients. The total heat flux has been plotted separately for sensible and latent heat flux and for stable and unstable conditions. If a negligible proportion of the fluxes occurs in regions where the coefficients vary considerably then terms 3 and 4 on the right-hand side of equations (5) can be neglected. This is obviously scheme dependent; Oberhuber's coefficients have strong wind speed dependence at all wind speeds. Figure 9 shows that about half the flux occurs at wind speeds over 20 knots and about 20% at wind speeds over 30 knots in the region where the coefficients have different wind speed dependencies (compare Figures 2a, e and k). 10% of the flux occurs below 10 knots where the stability effects are most important.

Figure 10 shows the covariances contributing to the mean sampling - classical flux differences with transfer coefficients from Smith (1988;1989). The triple covariance is small (term 5 in equation 5) for both sensible and latent heat. The difference can be seen to mainly result from the correlation between the air-sea temperature or humidity differences and the wind speed. The correlation of transfer coefficient and wind speed has a large effect for latent heat but not for sensible heat.

Figure 11 shows the annual mean error caused by using the classical method in the North Atlantic. Transfer coefficients used are those of Oberhuber (1988), (Figures 2g and h) which have a strong wind speed dependence. Errors can be seen to be large in regions of large flux (eg the Gulf Stream region) but erratic in sign.

## 1.3 Experimental Transfer Coefficients

Figures 2(a-1) shows the transfer coefficients  $C_T$  and  $C_E$  proposed by Bunker (1976), Isemer and Hasse (1987), Large and Pond (1981;1982), Oberhuber (1988), Smith (1988;1989) and Liu et al (1979) described in Section II, 1.1.2 as a function of wind speed and air-sea

temperature difference. The wind speed dependence of these schemes differs greatly in form. Figures 12a and b show the monthly mean transfer coefficients calculated for the VSOP-NA data; the schemes that show an increase in transfer coefficient as the wind speed increases (Bunker, Isemer and Hasse and Oberhuber) have a distinct annual cycle in the monthly mean transfer coefficient which results directly in a greater seasonal variation in the monthly mean fluxes (Figures 12c and d). A long time series of flux measurements would determine the correct wind speed dependence of the transfer coefficients.

The neutral transfer coefficient value largely determines the mean fluxes however fluxes from the atlases incorporate other effects, particularly the use by Esbensen and Kushnir (1981) of bulk SST instead of skin SST and alterations made to the wind speeds. The behaviour of the transfer coefficients with wind speed has been shown to be important in defining the seasonal cycle of fluxes.

## **2 MODELLING**

### **2.1 Koracin and Rogers Model**

#### 2.1.1 Model Characteristics: Koracin and Rogers (1990)

The Koracin and Rogers numerical model (described in Section II, 3.3) was obtained from Dr D. Rogers at Scripps Institute of Oceanography and implemented on the JRC UNIX computer system.

Figure 13 shows the profiles produced by the Koracin and Rogers model (Koracin and Rogers, 1990; Rogers and Koracin, 1992) using the coding obtained from Dr Rogers with idealised input profiles of wind speed, liquid water potential temperature and total water mixing ratio. Defects can be seen in these profiles which are plotted every 12 hours for a two day run. Profiles plotted in this figure and all figures up to and including figure 21 are 'instantaneous' values, that is the output of one, one minute timestep. Table 4 gives the variables for Figure 13 and all similar figures. In this model run the boundary layer grows rapidly (despite the large subsidence rate of about  $1.3 \text{ km day}^{-1}$ ) but does not become mixed. The profile of  $\theta_1$  (Figure 13e) shows the inadequacy of the top boundary condition. Cloud amounts (Figure 13o) are low despite the large liquid water content (Figure 13n) which results from the low kinetic energies (Figure 13i) and the use of the Gaussian cloud profile relationships (Mellor, 1977).

Preliminary model runs revealed that vertical advection of properties other than temperature was not correctly incorporated in the model. Figure 14 shows contours of  $\theta_1$  and

total water for a model run with a large subsidence rate which shows clearly the descent of the temperature inversion under the influence of the subsidence while the humidity profile remains unchanged (after some initial adjustment).

## 2.1.2 Model Development

The following subsections describe the changes made to the model code in order to obtain a more realistic and numerically consistent simulation of the boundary layer.

### 2.1.2.1 Mixing coefficients

The model initially had fixed limits on values for the vertical exchange coefficients  $K_m$  and  $K_h$ . The relatively high minimum value (1.0) used resulted in too vigorous mixing in regions where the K's, and hence the mixing, should have been low which led to rapid growth of the boundary layer. The mixing in regions where the K values was not artificially increased was not however large enough to maintain a well-mixed boundary layer.

The criteria for mixing coefficients which allow the model to remain stable are:

$$K_m, K_h \geq \frac{w\Delta z}{2} \quad (10)$$

where  $\Delta z$  is the vertical grid spacing. When equation 10 was used instead of a fixed minimum value (allowing much smaller mixing coefficients in some regions) the growth of the boundary layer was reduced and a sharp inversion was formed.

The upper limit was also increased from that initially specified as the mixing coefficient values were being limited. The resulting smoother mixing coefficient profiles produced more realistic profiles of other variables, for example removing spikes in the liquid water profile.

### 2.1.2.2 Vertical Advection

Since the model is one-dimensional, horizontal advection terms are assumed zero. However vertical advection terms should be non-zero. Vertical advection terms were found to be missing from the model after comparison with Yamada (1978) and Yamada (1979). Part of the advection term was present in  $\theta_1$ , other variables had no attempt at including advection. The finite difference form of the general equation (11) can be written as (12); note that Yamada used centred differencing whereas the Koracin and Rogers (1990) uses one-sided differencing.

$$\frac{\partial \phi}{\partial t} = \frac{\partial}{\partial z} \left( K \frac{\partial \phi}{\partial z} \right) - w \frac{\partial \phi}{\partial z} - A\phi + F \quad (11)$$

where  $t$  and  $z$  are the time and space co-ordinates respectively,  $\phi$  is the prognostic variable (in this model; liquid water potential temperature, total water, two horizontal components of wind speed and kinetic energy).  $K$  represents the vertical exchange coefficient ( $K_m$  or  $K_h$ ),  $w$  is the vertical velocity,  $A$  represents the dissipation (only present in kinetic energy equation) and  $F$  the forcing terms (eg radiative forcing for the temperature equation).

$$-A_k \phi_{k-1} + B_k \phi_k - C_k \phi_{k+1} = D_k \quad (12)$$

where  $A_k$  etc. are elements of a tri-diagonal matrix as given in equations 13 to 16 (see for example Press et al., 1989, for details of the method of solution):

$$A_k = -\frac{1}{2} \frac{\Delta t}{\left(z_{k-\frac{1}{2}} - z_{k-1\frac{1}{2}}\right)} \left( \frac{K_{k-1}}{\left(z_{k-1} - z_{k-2}\right)} + w_k \right) \quad (13)$$

$$\begin{aligned} B_k &= 1 + A\Delta t - \frac{\Delta t}{2} \left( \frac{K_k + K_{k-1}}{\left(z_k - z_{k-1}\right)\left(z_{k-1} - z_{k-2}\right)} \right) \\ &= 1 + A\Delta t + A_k + B_k \end{aligned} \quad (14)$$

$$C_k = -\frac{1}{2} \frac{\Delta t}{\left(z_{k+\frac{1}{2}} - z_{k-\frac{1}{2}}\right)} \left( \frac{K_k}{\left(z_k - z_{k-1}\right)} - w_k \right) \quad (15)$$

$$D_k = \phi_k + \Delta t \left( \frac{1}{2\left(z_{k-\frac{1}{2}} - z_{k-\frac{1}{2}}\right)} \left( K_k \left( \frac{\phi_{k+1} - \phi_k}{z_k - z_{k-1}} \right) - K_{k-1} \left( \frac{\phi_k - \phi_{k-1}}{z_{k-1} - z_{k-2}} \right) \right) - w_k \left( \frac{\phi_{k+1} - \phi_k}{z_k - z_{k-1}} \right) + F \right) \quad (16)$$

where  $\Delta t$  is the time step,  $k$  is the vertical co-ordinate and  $\phi$  is the solution at the current time-step.

### 2.1.2.3 Gradient boundary condition for $\theta_1$

Once vertical advection has been accounted for in the model the upper boundary conditions become more important, in particular,  $\theta_1$  requires a gradient boundary condition (other prognostic variables can be assumed to be constant across the upper boundary) to allow for the free-atmosphere lapse rate (the value of which has to be assumed in this model). This boundary condition is achieved by putting

$$\theta_{1_{k+1}} = \theta_{1_k} + \gamma \Delta z \quad (17)$$

at the top model level, where  $\gamma$  is the assumed gradient of  $\theta_1$ . The other prognostic variables are not calculated at the top model level. This boundary condition maintains the lapse rate in the free atmosphere as can be seen by comparing Figures 15a and 15b.

#### 2.1.2.4 Vertical motion profile

The vertical motion profile determines the warming rate in the 'free-atmosphere' above the boundary layer. Coarse vertical resolution had initially been used in this region as it was a region of low turbulence. It was found however that changes in the vertical exchange coefficients required to keep the grid Reynolds number within the required limits (see Section III, 2.1.2.1 above) had large and immediate effects throughout the whole model domain and radically changed the surface fluxes.

The vertical resolution was therefore changed in the upper region of the model (to be similar through the whole domain but with increased resolution at the surface). Changes to the profiles obtained with different vertical motion profiles now look to be compatible with the resultant change in heating in the top regions of the model. Figures 16a and b show model profiles of  $\theta_1$  with small changes to the vertical velocity profiles at the top of the model domain, before the change in vertical resolution. Figures 16c and d are comparable plots following the change in resolution. The second pair of plots can be seen to have much more similar boundary layer heights than the first pair. If the surface fluxes are compared ( $H_s$ , the sensible heat flux and  $H_l$ , the latent heat flux; Figures 17a - d) the time series show much greater agreement after the increase in resolution in the upper region of the model (17c and d are more similar than 17a and b).

#### 2.1.2.5 Description of present model status

Figures 18 - 20 show the full output for the model with the changes as described in the subsections above. The variables in Figures 18a-r are as Figure 13. Figures 19a-i show time series of surface values and solar radiation (see Table 5 for details). Figures 20a-r show contour plots of the time evolution of the variables (variables are similar to those in Figure 13, see Table 4, but 20c shows the pressure).

Figures 18 show the boundary layer growing and moistening from its initial state. The boundary layer is fairly well mixed in both temperature and water content (Figures 18e and f). The wind profile quickly become slab-like in the boundary layer with a discontinuity between the smaller wind speeds below the inversion and the larger wind speeds above (Figure 18a). The gradient boundary condition and the high values of vertical velocity in the free atmosphere have caused an unrealistic heating of the air in this region (Figure 18e), although the lapse-rate has been maintained. This heating effect can be removed either by an imposed cooling rate in

this region or by reducing the vertical velocity. Both methods have been used in different studies (see Koracin and Rogers 1992 and Siebesma and Cuijpers 1994). Cloud forms, there is total cloud cover just below the inversion of about 300m thickness at the end of the two day run (Figure 18o) and the boundary layer is energetic (Figure 18i).

Buoyancy flux profiles show consumption of buoyancy in the cloud associated with entrainment and also the production of buoyancy at the surface (Figure 18q). The moisture flux is positive everywhere at the boundary layer is still moistening (Figure 18h). Both the radiative fluxes seem to be in error. Incoming short wave radiation appears to be overestimated; values appear to be a factor of 1.6 too high in January and a factor of 2.4 too high in June (see Figure 19d). The longwave cooling in the absence of cloud seems to be large; values are similar for cloudy and cloud-free situations (Figure 18g).

Figures 19 show the surface parameters for this model and also total water contents, see Table 5 for details. Most of the variables appear to be reaching steady state. The total water content is however increasing due to the large latent heat flux of  $200\text{W/m}^2$  which is approximately constant and the increasing boundary layer depth.

Figures 20 show contour plots (x-axis: time, y-axis: height) of each of the variables. These plots have been constructed from the same output as that shown in Figures 18, that is, one minute values of each variable output once per hour have been contoured. The growth of the boundary layer in height from 800m to 1500m can be seen in each plot. There is variability in the fluxes (20h, the moisture flux; 20q, the buoyancy flux and 20r, the momentum flux).  $\theta_1$  can be seen to be slightly unstable (Figure 20e).

### 2.1.3 Model Resolution

#### 2.1.3.1 Vertical Resolution

As discussed in Section III, 2.1.2.4 the vertical resolution was altered to be approximately equal throughout the model, although increased resolution is used at the surface in the logarithmic layer. The resolution used as standard is 2 mb (about 8m). Model runs using changes in resolution have been compared to RUN 55 (plotted in Figures 18 - 20) which used 2 mb vertical resolution and a 60 second time step. The effects of doubling and halving this resolution with a constant time-step of 60 seconds are discussed here. The output profiles for a 4 mb resolution run (RUN 60) were not significantly different from the standard profiles. But, although the profiles for the prognostic variables were similar the cloud amounts were different. The relationship of the vertical resolution with the Gaussian cloud profile relationship therefore needs to be examined. A general impression is that the profiles with

coarse resolution have smoother variations in the derivative variables but time-averaged profiles may need to be examined before the coarse resolution grid is used in further study.

A 1 mb resolution run was then made (RUN 61). This finer resolution leads to spiky flux profiles and reduced cloud amount. Again the growth of the boundary layer and profiles of the prognostic variables are similar to the 2 mb resolution case.

As the profiles in each case are the output from one, one minute time step every six hours the variability between time steps and time integrated profiles must be examined before differences between the different resolution runs can be regarded as significant.

#### 2.1.3.2 Time Step

The effect of increasing and decreasing the time step with a constant vertical resolution of 2 mb was examined. The standard run has a 1 minute time step. Model runs were made with 30 second (RUN 58) and 2 minute (RUN 59) time steps. As with the changes in vertical resolution the variations in cloud amount seem to be the most significant factor. Again, the significance of variations in the flux profiles cannot be determined from these instantaneous profiles.

#### 2.1.3.3 Effect of Resolution on the Surface Fluxes

Figure 21 a-d show the surface fluxes for the different resolution runs described in the previous two subsections. The differing resolutions can be seen to have little effect on either the sensible or latent heat fluxes.

#### 2.1.4 Mean Profiles and Variability

The model was then altered to output mean profiles and also the standard deviation of the variables to allow the differences between the model runs to be more easily assessed. Figures 22 - 24 show the profiles (an hourly mean plotted every 6 hours), surface values and contour plots respectively. Figures 25 show the standard deviation of the variables plotted in Figures 24.

The profiles of the prognostic variables are little different between the instantaneous profiles (Figures 18) and the hourly average profiles (Figures 22). However the flux profiles, in particular, do show some differences. These fluxes have high variability, particularly in the cloud layer so the flux profiles are generally smoother for the averaged variables although the moisture flux averaged values (Figure 22h) are larger than the instantaneous values (Figure 18h) indicating that the scales of variability in this flux field in particular was poorly sampled by the one minute 'instantaneous' profiles taken once per hour.

Figures 23 show the averaged surface values with error bars of one standard deviation. The variability in these surface parameters can be seen to be small.

Figures 24 are contour plots of the averaged variables. Comparison with Figures 20 shows that fluctuations in the variables are more regular than they appear in the instantaneous output (eg compare the buoyancy flux plots Figures 20h and 24h). This is due to aliasing of the fluctuations. The plots of standard deviation reveal high variability in the cloud layer with mixing events occurring every 2 - 3 hours which extend throughout the boundary layer. Shorter time-period averages may be necessary to fully define the processes.

#### 2.1.5 Numerical Experiments: The Surface Fluxes

The model has been shown to give consistent results for the parameters currently being used. The effect of varying external parameters on the surface fluxes of sensible and latent heat has been studied using the model evolution as in Figures 18 - 20 as a starting point. As a preliminary study the effect on the surface fluxes of the wind speed, the magnitude of the vertical velocity and the effects of an imposed SST gradient have been looked at. Figures 26a-c show the change in the fluxes with each of these parameters. Figure 26a shows the dependence on the fluxes of the horizontal wind speed (that is the geostrophic wind speed at the top of the model domain). Latent heat flux can be seen to increase strongly with wind speed but the sensible heat flux shows little variation with a possible slight reduction at higher wind speeds. Figure 26b shows the effect of the imposed vertical motion on the surface fluxes. The vertical motion was increased from about 0.3 km per day to 1.4 km per day with little effect on the fluxes. Figure 26c shows the effect of an imposed SST gradient on the fluxes. As the model atmosphere is effectively advected over warmer water both the sensible and latent heat fluxes increase. This is in partial agreement with the results of Kraus and Schaller (1978) (Section II, 4.2). They found essentially no dependence of the surface fluxes on the divergence of the horizontal wind (equivalent in this simple model to the large-scale vertical motion). They did find variation with the surface wind speed and the imposed horizontal SST gradient, but the dependence they found on the wind speed was smaller than that on the SST gradient.

There is possible support for the prediction that the surface fluxes do not depend on the vertical motion from the JASIN experiment (Taylor et al 1978). Heat budgets of the lower atmosphere show no link between these two parameters, although there is a large uncertainty in the estimates of vertical motion.

### 2.1.6 Summary

The Koracin and Rogers (1990) numerical model of the marine atmospheric boundary layer has been improved to produce more realistic simulations of the atmosphere (compare Figures 13 and 18). The model now maintains a sharp temperature and humidity discontinuity as is often observed in the real atmosphere and can be run for at least 30 days without becoming unstable. The structure of the boundary layer and the surface fluxes seem to be little affected by changes to the time and space resolution of the model; this is under further study. Use of variables averaged over all time steps between the output time steps should enable the significance of variations between the different model runs to be determined. An extension of this would be to produce daily heat budgets.

A number of features of the model implementation require further investigation and possible modification. The finite difference equations (13 - 16) appear to use down-stream differencing (as the vertical motion applied is always in a downward direction). Also the level thickness used in deriving the derivative terms appears to be appropriate to the level below the property difference being considered. This second point is not now so important as approximately equal layer thicknesses are being used (except in the surface layer) but the effects of both these possible problems with the numerical scheme will need to be addressed. If necessary an up-stream differencing scheme may be applied. As was indicated in Section III, 2.1.2.5 both the short wave and the long wave radiative fluxes do not appear to be correct. This will be investigated and if possible improved.

The effect of varying vertical resolution on cloud amount will be studied. The Gaussian cloud profile relationships relate the cloud amount to not only the saturation of the air but to the kinetic energy and the variance of liquid water amount. The resolution of the model in the cloud region may have an effect on the variance of the liquid water content and the resulting difference in calculated cloud amount may be significant.

## 2.2 Met Office Single Column Model

The Met. Office SCM (described in Section II, 3.4) was obtained from the Hadley Centre and implemented on the JRC UNIX system. As the model was received, the model was forced to an observational data set by adding increments to temperature, humidity and wind speed profiles at each level (Lean, 1922). The increments are selected randomly from populations appropriate to the climatic situation and vertical correlations are taken into account. In this way the effects of the large scale motions which cannot be calculated within the vertical column are simulated. The surface fluxes were also set by observational values.

The observational forcing terms were removed from the program. Contour plots of the time evolution of the prognostic variables as a function of pressure are shown in Figure 27a, the change in scale relative to the Koracin and Rogers model should be noted (3 km height in the Koracin and Rogers is equivalent to ~ 650 mb). These plots show that the processes acting to increase the boundary layer height (entrainment, surface fluxes, see Section II, 2.1) are not being balanced by the subsidence of the overlying air as is often observed. The effects of this subsidence were simulated by adding increments to  $\theta$ , water vapour and the wind speeds calculated from the vertical gradients of these properties combined with a prescribed profile of vertical velocities, equation Y gives the increment for  $\theta$ , ( $\Delta\theta$ ) as a function of  $w$ , the vertical velocity, the vertical gradient of  $\theta$  and the time step ( $\Delta t$ ). Increments to specific humidity and the wind speed components are calculated similarly.

$$\Delta\theta = -w \frac{\partial\theta}{\partial z} \Delta t \quad (18)$$

Figures 27b and c show contour plots from the model with different values of vertical velocity. The effects of subsidence appear to be simulated by this method as the boundary layer height is reduced as the magnitude of the maximum vertical velocity increases.

Work has only recently started with this code but some areas of interest and possible concern have been identified. Initially water vapour is mixed very strongly upwards; the height of mixing then reduces leaving a portion of cloud isolated above the boundary layer. The two cloud layers are intermittently linked by convection which maintains the upper cloud against the effects of the imposed subsidence. The mechanisms driving this initial mixing and its physical plausibility need to be looked at. This mixing is very dependent on the initial value set for the roughness length although this is a parameter subsequently calculated by the model. The vertical motion profile does not have the correct form at present. This is causing warming in the troposphere due to the temperature increments made and results in a tropospheric temperature significantly above that observed. Further validation is required.

## **SECTION IV CONCLUSIONS AND FUTURE WORK**

### **1 SUMMARY**

The VOS data required for validation has been assessed, errors have been identified in the data and methods of correction derived. The form of the transfer coefficients for the bulk formulae has been considered and programs to calculate the coefficients written. The transfer coefficients of Smith (1988) will be used with individual observations as large errors have been shown to be introduced by the use of average parameters. As a result of this work we have a method of calculating fluxes from the ship data which is believed to be unbiased and can therefore be used to validate fluxes calculated using new approaches.

Two computer models of the lower atmosphere have been implemented on the computer system and graphics and display software written. Inconsistencies have been identified in the Koracin and Rogers model and resolved allowing physically reasonable profiles to be obtained. The code of the Met. Office SCM has been altered to remove the external forcing applied and to simulate the effects of subsidence.

Problems that might be expected in the model studies are the possibly inadequate treatment of cloud processes by the models and particularly the entrainment of air into the boundary layer. This will affect the whole energy balance of the boundary layer and therefore the surface fluxes. The surface flux and surface layer parameterisations in the model may not be good enough to study the near surface structure. Horizontal advection is parameterised in these models and the correct prescription of the horizontal forcing will have to be imposed. It may also be difficult to isolate the effects of individual elements of the large-scale forcing in the numerical experimentation.

Some preliminary numerical experiments have been made with the Koracin and Rogers model.

### **2 CONCLUSIONS**

Kraus and Schaller (1978) and Schubert (1976) have demonstrated that the surface fluxes depend on large-scale effects in a simple numerical model. Additionally, the work of Chou and Atlas (1982) demonstrates that the surface fluxes are dependent on processes occurring away from the region of obvious surface influence; although a fairly specific case was studied.

Preliminary numerical experiments have shown that it is possible to demonstrate the effects of external parameters on the surface fluxes of sensible and latent heat using a numerical model. Using the Koracin and Rogers model (after alteration) the surface fluxes have

been shown to depend on the wind speed and the SST gradient in the upwind direction. The model fluxes showed no dependence on the rate of subsidence of the air overlying the boundary layer. The dependence of these results on the model formulation must be assessed.

### 3 FUTURE WORK

The general form of the intended work has been outlined in Section II, 2. Specific details will be covered in this subsection.

The main priority will be to validate both of the models. The problems detailed in earlier sections will be addressed to fully understand the model behaviour. The reason for the rapid mixing observed in the SCM will be determined and the behaviour of the model assessed. The vertical resolution of the SCM must be significantly increased if the boundary layer height is going to be well resolved and the stability of the integration will have to be maintained. The two models must then be made compatible so the output from each can be easily compared. This may be best done by calculating thermodynamic variables such as  $\theta_e$  and  $\theta_v$ . Only the lower portion of the SCM can be compared in this way.

Once a satisfactory model formulation has been achieved, the effects, especially in the surface fluxes, of changes in SST, wind speed, magnitude and profile of vertical velocity, horizontal advection; that is the SST history of the air column, and the tropospheric lapse rate will be assessed along with other parameters as seems appropriate. The changes in the fluxes may be correlated to parameters such as the strength of the temperature and humidity inversions and the boundary layer depth. A parameterisation can then start to be developed.

The Koracin and Rogers model is now giving fairly realistic results; the radiation schemes require examination however. Further work is required on the SCM before model intercomparisons and validation can be started.

5. TABLES

Parameter	Instrument	Satellite	dates	accuracy	resolution	swath*	notes
Wind speed	Scatterometer	ERS-1	7-91 onwards	$\pm 1.2\text{m/s}$ $\pm 15^\circ$	25km	475km	only operates when SAR isn't
		SeaSat	6-78 to 10-78	$\pm 2\text{m/s}$ $\pm 15^\circ$	50km	1400km	400km gap below satellite
	Altimeter	ERS-1	7-91 onwards	greatest of 10% or 2m/s	7-12km	7-12km	no wind direction
		Topex-Poseidon	8-92 onwards	greatest of 10% or 2m/s	~10km	~10km	no wind direction
	SSM/I	DMSP	ongoing program		~50km	1499km	Special Sensor Microwave/Imager
SST	AVHRR	NOAA series	1978 onwards	0.3-0.5K	1km	512km	Calibrated 8km resolution historical data available as 'Pathfinder'
	ATSR	ERS-1	7-91 onwards	0.5-0.7K	1km	512km	
	SMMR	SeaSat	6-78 to 10-78	$\pm 2\text{K}$	50km	600km	Scanning Multichannel Microwave Radiometer
	SSM/T	DMSP	ongoing program		~50km		Special Sensor Microwave/ Temperature
Total water vapour and liquid water	SSM/I	DMSP	ongoing program	$\pm 2\text{kg/m}^2$	50km	1400km	accuracy comparable to radiosondes
	Sounder	ERS-1	7-91 onwards	$\pm 3\text{kg/m}^2$	~20km	~20km	for correction to altimeter
		Topex-Poseidon	8-92 onwards	$\pm 2\text{kg/m}^2$	~20km	~20km	
	SMMR	SeaSat	6-78 to 10-78	$\pm 2\text{kg/m}^2$	50 km	600km	
		Nimbus 7	10-78 to 7-88	$\pm 2\text{kg/m}^2$	150km	600km	

Table 1 - Summary of satellite data available for use in study.

Information in this table is from the ERS user handbook (published by ESA), the Matra Marconi Space Earth Observation Directory 1993/1994 and from discussions with David Cotton, Tom Forrester and Trevor Guymer at the James Rennell Centre for Ocean Circulation.

Note on data coverage for satellite sensors.

The satellite swath can be related to coverage using the diagram below which shows data coverage for one day from the wind-scatterometer on ERS-1 in a 35-day repeat orbit. The swath width is approximately 500km for this sensor. All orbits for this wide swath give quasi-global coverage every 3 days. Coverage and resolution depend also on latitude. The orientation of the satellite orbit determines the range of latitudes sampled ( $\pm 80^\circ$  for ERS-1). The repeat cycle becomes more critical for data coverage for the nadir sensors.

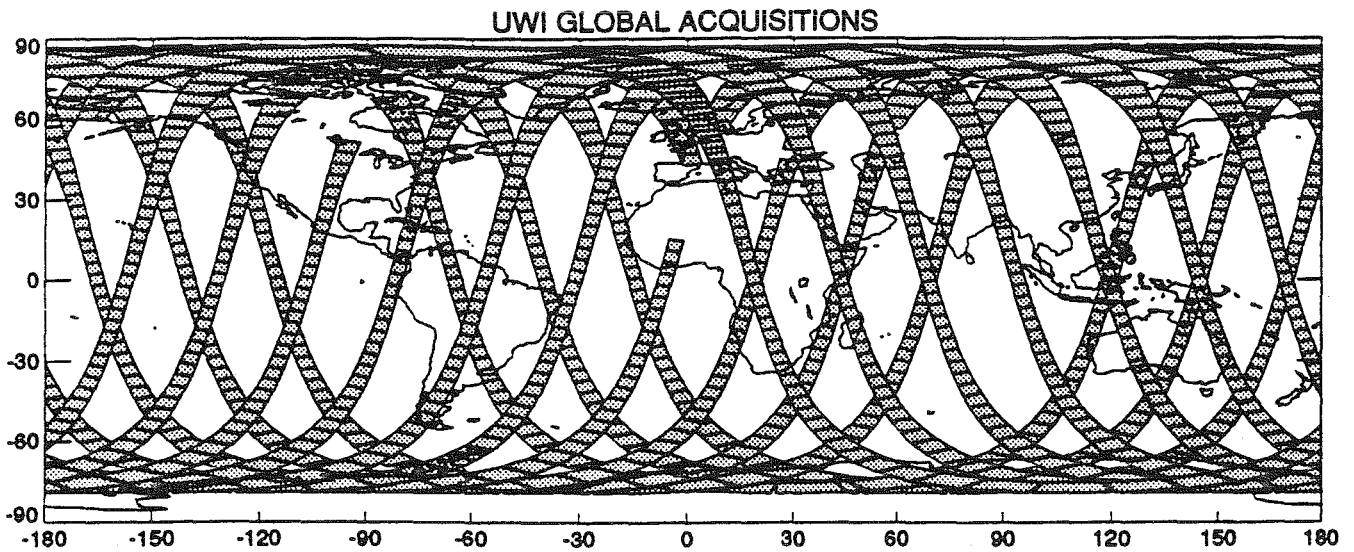


Table 2 - Summary of heat budget studies calculating the surface turbulent fluxes

Study	Region	Grid Scale	Time	Data	Solar Radiation	Albedo	Net Longwave	Sensible Heat Flux	Latent Heat Flux	Cloud	Wind Scale Conversion	Climatologies Compared	
Esbensen and Kushnir (1981)	Global	4° x 5°	monthly and annual	TDF 11° climatologies classical	Berliand (1960) Budyko (1974)	Payne (1972)	Berliand and Berliand (1952)	Liu et al. (1979)  (used bulk sst instead of skin sst)	Liu et al. (1979)  (used bulk sst instead of skin sst)	Berliand and Strokina (1980)	WMO 1100	Schutz and Gates (1971) Schutz and Gates (1972) Schutz and Gates (1973) Schutz and Gates (1974) Hasenrath and Lamb (1977) Bunker and Goldsmith (1979)	
Bunker (1976)	North Atlantic	1° x 1° (coast) to 2° x 5° (open ocean)	monthly	TDF 11 1941 - 72 sampling	Budyko (1963)	Payne (1972)	Budyko (1963)	Bunker (1976)	Bunker (1976)	TDF 11	WMO 1100	OWS E Budyko (1963)	
Isemer and Hasse (1987)	North Atlantic	as Bunker (1976)	monthly and annual	TDF 11 1941 - 72 sampling	Reed (1977) Transmission factor = 0.7, cloud cover coeff = 0.62	Payne (1972)	Budyko (1974) cloud cover exponent = 1	(Bunker, 1976) *0.83	(Bunker, 1976) *0.87	TDF 11	Kaufeld (1985)	Bunker (1976)	
Isemer and Hasse (1987)	Revised following inverse calculation	as Bunker (1976)	monthly and annual	TDF 11 1941 - 72 sampling (Tdp-sst-0.07)	Reed (1977) Transmission factor = 0.69, cloud cover coeff = 0.637	Payne (1972)	Budyko (1974) cloud cover exponent = 1.1	(Bunker, 1976) *0.87	(Bunker, 1976) *0.92	TDF 11	Kaufeld (1985)	Bunker (1976)	
Oberhuber (1988)	Global	2° x 2°	monthly and annual	COADS Wright (1988) classical	Zillmann (1972) cloudiness factor from Reed (1977)		Berliand and Berliand (1952)	Large and Pond (1982) Large and Pond (1981)	Large and Pond (1982) Large and Pond (1981)	COADS	WMO 1100		
Bunker et al. 1982	Mediterranean and Red Seas	as Bunker (1976)	annual	TDF 11 1941 - 72 sampling	Budyko (1963)	Payne (1972)	Budyko (1963)	Bunker (1976)	Bunker (1976)	TDF 11	WMO 1100	Compared with oceanic transport measurements through Straits of Gibraltar and Bab-el-Mandeb	
Isemer et al. (1989)	North Atlantic	as Bunker (1976)	annual	TDF 11 1941 - 72 sampling (Tdp-sst-0.07 & Ta-sst-0.07)	Reed (1977) Transmission factor = 0.69, cloud cover coeff = 0.636	Payne (1972)	Budyko (1974) cloud cover exponent = 1.1	(Bunker, 1976) *0.87	(Bunker, 1976) *0.92	TDF 11	Kaufeld (1985)	Rago and Rossby (1987) Hall and Bryden (1982)  Compared with oceanic meridional transport measurements.	
Smith and Dobson (1984)	OWS B	-	-	OWS B	Lumb (1964)	Payne (1972)	Budyko (1974)	10 <sup>-3</sup> no wind speed dependence Stability from Dyer (1974)	1.2°C H	Observation	-		
Hsiung (1986)	Global	5° x 5°	monthly and annual	TDF 11 1949 - 1979 classical	Similar to Reed (1977)	Payne (1972)	Budyko (1963)	=C <sub>E</sub>	Bunker (1976)	TDF 11	WMO 1100	Hasenrath and Lamb (1977) Bunker (1976) Clark (1967) Weare et al. (1980) Esbensen and Kushnir (1981)	
Bunker and Worthington (1976)	North Atlantic	10° x 10°	monthly and annual	NCC	Budyko (1963)	Payne (1972)	Budyko (1963)	Bunker (1976)	=C <sub>H</sub>	TDF 11	WMO 1100	(Budyko, 1963)	
Hsiung (1985)	Global	5° x 5°	annual	TDF 11	Similar to Reed (1977)	Payne (1972)	Budyko 1974	Bunker and Worthington (1976)	=C <sub>H</sub>		WMO 1100	Meridional transport calculation	
Budyko (1963)	Global		annual bi-monthly										
Hasenrath and Lamb (1977)	Tropical Atlantic and Eastern Pacific	1° x 1°	monthly										
Talley (1984)	Pacific			Used data of Clark (1967), Weare et al. (1980) and Esbensen and Kushnir (1981) to estimate meridional heat transport.									

Correction	Sensible Heat Flux Change (%)	Latent Heat Flux Change (%)	Sensible + Latent Heat Flux Change (%)
Dewpoint	0	+10	+8
SST	-8	-4	-4
CMM	+2	+6	+5
Height	-5	-8	-7
Solar Radiation	+19	+1	+4
Full	+9	+4	+5

**Table 3 - The effect of errors in VOS data on the surface fluxes of sensible and latent heat. Transfer coefficient scheme used is Smith (1988;1989) with the VSOP-NA data set.**

Figure letter	Variable	Symbol	Units
a	u-component wind speed	u	ms <sup>-1</sup>
b	v-component wind speed	v	ms <sup>-1</sup>
c	w-component wind speed	w	ms <sup>-1</sup>
d	mixing parameter	q2l	m <sup>3</sup> s <sup>-2</sup>
e	liquid water potential temperature: $\theta_l$	thet l	°C
f	total water mixing ratio	qtot	gkg <sup>-1</sup>
g	radiative cooling rate	radcl	Kday <sup>-1</sup>
h	vertical moisture flux	wqw	gkg <sup>-1</sup> ms <sup>-1</sup>
i	kinetic energy	qsq	m <sup>2</sup> s <sup>-2</sup>
j	vertical exchange coefficient for momentum: $K_m$	eddy	m <sup>2</sup> s <sup>-1</sup>
k	vertical exchange coefficient for heat: $K_h$	edkh	m <sup>2</sup> s <sup>-1</sup>
l	mixing length	black	m
m	solar heating rate	solht	Ks <sup>-1</sup>
n	liquid water mixing ratio	qliq	gkg <sup>-1</sup>
o	cloud fraction	ratio	
p	parameter in Gaussian cloud relations	qlsq	?
q	buoyancy flux	wtv	Kms <sup>-1</sup>
r	momentum flux	tow	m <sup>2</sup> s <sup>-2</sup>

**Table 4 - Summary of variables in Koracin and Rogers (1990) marine atmospheric boundary layer model.**

Figure letter	Variables	Symbol	Units
a	mixing length for momentum	z0	m
	mixing length for temperature	z0t	m
b	friction velocity	u*	ms <sup>-1</sup>
	temperature scale	t*	°C
	humidity scale	q*	gkg <sup>-1</sup>
c	sensible heat flux	Hs	Wm <sup>-2</sup>
	latent heat flux	Hl	Wm <sup>-2</sup>
d	incoming solar radiation	solar	Wm <sup>-2</sup>
	solar radiation at top of cloud	soltop	Wm <sup>-2</sup>
	solar radiation at base of cloud	solbas	Wm <sup>-2</sup>
e	water vapour flux	wqw	gkg <sup>-1</sup> ms <sup>-1</sup>
	bouyancy flux	wtv	Kms <sup>-1</sup>
	stress	tau	m <sup>2</sup> s <sup>-2</sup>
f	liquid water potential temperature at surface	thet l	°C
	liquid water potential temperature at level 2	thet(2)	°C
g	total water at surface	qtot	gkg <sup>-1</sup>
	total water at level 2	qtot(2)	gkg <sup>-1</sup>
h	u-component of wind speed at level 2	u(2)	ms <sup>-1</sup>
	v-component of wind speed at level 2	v(2)	ms <sup>-1</sup>
i	measure of total water vapour	twvap	arbitrary
	measure of total liquid water	tqliq	arbitrary

**Table 5 - Summary of surface variables in Koracin and Rogers (1990) marine atmospheric boundary layer model.**

## APPENDIX A - MONIN-OBUKHOV SIMILARITY THEORY AND TRANSFER COEFFICIENTS

This Appendix details the description of atmospheric stability in terms of Monin-Obukhov similarity theory and follows, for example, Businger (1973). It is included here for completeness.

The Monin-Obukhov length ( $L_{MO}$ ) is the height in the non-neutral surface layer where buoyancy effects equal the shear production of energy. The  $L_{MO}$  is given by equation A1.

$$L_{MO} = -\frac{(u_*^3/\kappa)}{g\beta(w'\theta'_v)_0} \quad (A1)$$

where  $\kappa$  is the von Karman constant (0.4),  $\beta$  is the thermal expansion coefficient,  $\theta_v$  is the virtual temperature,  $g$  is the acceleration due to gravity,  $w$  is the vertical velocity and  $u_*$  is the friction velocity and is related to the wind stress  $\tau$  and air density  $\rho$  by:

$$u_* = \sqrt{\frac{|\tau|}{\rho}} \quad (A2)$$

Thus when the turbulent motion is highly suppressed by stratification  $L_{MO}$  tends to  $+\infty$  and when free convection occurs  $L_{MO}$  tends to  $-\infty$ . The dimensionless length scale used is  $z/L_{MO}$  and the form of dimensionless gradients of temperature ( $\phi_t$ ), humidity ( $\phi_q$ ) and momentum ( $\phi_m$ ) are found empirically see for example Businger (1973), equations A3.

$$\left. \begin{aligned} \frac{\partial U}{\partial z} &= \left(\frac{u_*}{\kappa z}\right) \phi_m\left(\frac{z}{L_{MO}}\right) \\ \frac{\partial \theta_t}{\partial z} &= \left(\frac{\theta_*}{\kappa z}\right) \phi_h\left(\frac{z}{L_{MO}}\right) \\ \frac{\partial q_t}{\partial z} &= \left(\frac{q_*}{\kappa z}\right) \phi_q\left(\frac{z}{L_{MO}}\right) \end{aligned} \right\} \quad (A3)$$

$\theta_*$ ,  $q_*$  and  $u_*$  (introduced above) are temperature, water vapour and velocity scales given by equations A4:

$$\left. \begin{aligned} u_* &= \sqrt{w'v'} \\ \theta_* &= -\frac{w'\theta'}{u_*} \\ q_* &= -\frac{w'q'}{u_*} \end{aligned} \right\} \quad (A4)$$

These gradient relations are then integrated to give temperature ( $\Psi_t$ ), humidity ( $\Psi_q$ ) and wind profiles ( $\Psi_m$ ) of the form given by equations (A5), see for example Large and Pond (1982).

$$\left. \begin{aligned} \Psi_{m,t,q}(Z/L_{MO} > 0) &= -7Z/L_{MO} \\ \Psi_{t,q}(Z/L_{MO} < 0) &= 2 \ln\left(\frac{1}{2}(1+X^2)\right) \\ \Psi_m(Z/L_{MO}) &= 2 \ln\left(\frac{1}{2}(1+X)\right) + 2 \ln\left(\frac{1}{2}(1+X^2)\right) - 2 \tan^{-1}(X) + \pi/2 \\ \text{where } X &= \phi_m(z/L_{MO}) \end{aligned} \right\} \quad (A5)$$

where a typical empirical functional form for X is given by A6:

$$X = \left(1 - 16Z/L_{MO}\right)^{-0.25} \quad (A6)$$

The neutral values of  $C_D$ ,  $C_E$  and  $C_T$  are then given by

$$\left. \begin{aligned} C_{DN} &= \frac{\kappa^2}{\left[\ln(10/z_0)\right]^2} \\ C_{EN} &= \frac{\kappa^2}{\left[\ln(10/z_0) \ln(10/z_q)\right]} \\ C_{TN} &= \frac{\kappa^2}{\left[\ln(10/z_0) \ln(10/z_t)\right]} \end{aligned} \right\} \quad (A7)$$

The roughness lengths  $z_0$ ,  $z_q$  and  $z_t$  are determined experimentally. The non-neutral values of  $C_E$  and  $C_T$  are then found from equations A8:

$$\left. \begin{aligned} C_E &= \frac{C_{EN} \sqrt{\left(\frac{C_D}{C_{DN}}\right)}}{1 + \frac{C_{EN}}{\kappa \sqrt{C_{DN}}} \left[ \ln\left(\frac{Z}{10}\right) - \Psi_q\left(\frac{Z}{L_{MO}}\right) \right]} \\ C_T &= \frac{C_{TN} \sqrt{\left(\frac{C_D}{C_{DN}}\right)}}{1 + \frac{C_{TN}}{\kappa \sqrt{C_{DN}}} \left[ \ln\left(\frac{Z}{10}\right) - \Psi_t\left(\frac{Z}{L_{MO}}\right) \right]} \end{aligned} \right\} \quad (A8)$$

where

$$\sqrt{\frac{C_D}{C_{DN}}} = \frac{1}{1 + \frac{\sqrt{C_{DN}}}{\kappa} \left[ \ln\left(\frac{Z}{10}\right) - \Psi_m\left(\frac{Z}{L_{MO}}\right) \right]} \quad (A9)$$

The Charnock relation (Charnock, 1955) can be derived from dimensional analysis (A9)

$$z_0 = \frac{au^{2*}}{g} \quad (A10)$$

## APPENDIX B - TRANSFER AND VERTICAL MIXING COEFFICIENTS IN THE SCM

Transfer coefficients in the SCM are calculated based on a Richardson number using the following formulation:

$$\zeta_1 \equiv \frac{z}{L_{MO}} \equiv \frac{\kappa C_H}{C_D^{3/2}} Ri_B \quad (B1)$$

where the bulk Richardson number  $Ri_B$  is related to the height above the surface of the first layer interface ( $z_1$ ), the current speed ( $v_0$ ), the wind speed at  $z_1$ , ( $v_1$ ) and the buoyancy difference across the layer  $\Delta B$  by equation B2

$$Ri_B = \frac{(z_1 + z_{0m})\Delta B}{|v_1 - v_0|^2} \quad (B2)$$

After consideration of the neutral values and asymptotic limits of  $C_D(Ri)$  and  $C_H(Ri)$  the following relationships are formed:

$$\left. \begin{aligned} C_D &= C_{DN} f_m \\ C_H &= C_{DN} f_h \end{aligned} \right\} \quad (B3)$$

where  $C_{DN}$  and  $C_{TN}$  come from equations A6. The stability factors  $f_m$  and  $f_h$  are given by equations B4.

$$\left. \begin{aligned} f_m &= \frac{1}{1+A_m Ri_B} \\ f_h &= \frac{1}{1+A_h Ri_B} \end{aligned} \right\} \text{for } Ri_B \geq 0$$

$$\left. \begin{aligned} f_m &= 1 - \frac{A_m Ri_B}{1+B_m (-Ri_B)^{1/2}} \\ f_h &= 1 - \frac{A_h Ri_B}{1+B_h (-Ri_B)^{1/2}} \end{aligned} \right\} \text{for } Ri_B < 0 \quad (B4)$$

and

$$B_m = \frac{D_m A_m C_{DN}}{f(z_1, z_{0m}, z_h)}$$

$$B_h = \frac{A_h C_{HN}}{f(z_1, z_{0m}, z_h)} \quad (B5)$$

where  $A_m$  and  $A_h$  are constants (both set to 10),  $D_m$  is set to 2, and

$$f(z_1, z_{0m}, z_h) \approx (3h)^{-3/2} \left( \frac{z_h}{z_1 + z_{0m}} \right)^{1/2} \quad (B6)$$

with  $(3h)^{3/2}$  as 4.

The vertical mixing coefficients  $K_m$  and  $K_h$  are given by equations B7

$$\left. \begin{aligned} K_m &= l_m^2 f_m(Ri) \left| \frac{\partial v}{\partial z} \right| \\ K_h &= l_m l_h f_h(Ri) \left| \frac{\partial v}{\partial z} \right| \end{aligned} \right\} \quad (B7)$$

where the stability functions  $f_m$  and  $f_h$  are given by equations B8.

$$\left. \begin{aligned} f_h = f_m &= \frac{1}{1 + G_0 Ri} & Ri \geq 0 \\ f_h &= 1 - \frac{G_0 Ri}{1 + \left(\frac{G_0}{E_H}\right) \left(\frac{l_m}{l_h}\right) (-Ri)^{-1/2}} \\ f_m &= 1 - \frac{G_0 Ri}{1 + \left(\frac{G_0}{E_M}\right) \left(\frac{l_m}{l_h}\right) (-Ri)^{-1/2}} \end{aligned} \right\} \quad Ri < 0 \quad (B8)$$

where  $G_0$ ,  $E_H$  and  $E_M$  are adjustable parameters set to 10, 25 and 4 respectively.

The mixing coefficients never reduce to zero and cut off all the mixing. In the unstable limit the mixing is independent of the wind shear.

## REFERENCES

- Ball, F. K., 1960: Control of inversion height by surface heating. *Q. J. Roy. Met. Soc.*, 86(370), 483-494.
- Berliand, M. E. and T. G. Berliand, 1952: *Determining the net long-wave radiation of the Earth with consideration of the effect of cloudiness*. 1, *Isv. Akad. Nauk. SSSR Ser. Geofiz.*
- Berliand, T. G., 1960: Methods of climatological computation of total incoming solar radiation. *Meteorol. Gidrol*, 6, 9-12.
- Berliand, T. G. and L. A. Strokina, 1980: *Global distribution of the total amount of cloudiness*. Hydrometeorology Publishing House, 71 pp.
- Blackadar, A. K., 1962: The vertical distribution of wind and turbulent exchange in a neutral atmosphere. *J. Geophys. Res.*, 67(8), 3095-3102.
- Blanc, T. V., 1985: Variation of bulk-derived surface flux, stability and roughness results due to the use of different transfer coefficient schemes. *J. Phys. Oceanogr.*, 15(6), 650-669.
- Blanc, T. V., 1986: The effect of inaccuracies in weather-ship data on bulk derived estimates of flux, stability and sea-surface roughness. *J. Atmos. & Oceanic Tech.*, 3(1), 12-26.
- Bryden, H. L. and M. M. Hall, 1980: Heat transport by currents across 25°N in the Atlantic Ocean. *Science*, 207, 884-886.
- Budyko, M. I., 1963: *Atlas of heat balance of the world*. Glabnaia Geofiz. Observ.
- Budyko, M. I., 1974: *Climate and Life*, Academic Press.
- Bunker, A. F., 1976: Computations of surface energy flux and annual air-sea interaction cycles of the North Atlantic Ocean. *Monthly Weather Review*, 104, 1122-1140.
- Bunker, A. F., H. Charnock and R. A. Goldsmith, 1982: A note on the heat balance of the Mediterranean and Red Seas. *J. Mar. Res.*, 40 Supplement, 73-84.
- Businger, J. A., 1973: Turbulent transfer in the atmospheric surface layer. *Workshop on Micrometeorology*, D. A. Haugen, Ed., American Meteorological Society, 67-100.
- Carissimo, B. C., A. H. Oort and T. H. V. Haar, 1985: Estimating the meridional energy transports in the atmosphere and ocean. *J. Phys. Oceanogr.*, 15, 82-91.
- Charnock, H., 1955: Wind stress on a water surface. *Q. J. Roy. Met. Soc.*, 81(639-640).

- Chou, S. H. and D. Atlas, 1982: Satellite estimates of ocean-air heat fluxes during cold air outbreaks. *Mon. Wea Rev.*, 110, 1434-1450.
- Clark, N. E., 1967: *Large-scale heat transfer processes and fluctuations of sea surface temperature in the North Pacific Ocean*. MIT.
- Driedonks, A. G. M. and P. G. Duynkerke, 1989: Current problems in the stratocumulus-topped atmospheric boundary layer. *Boundary-Layer Meteorol.*, 46(3), 275-303.
- Esbensen, S. K. and Y. Kushnir, 1981: *The heat budget of the global ocean: An atlas based on estimates from surface marine observations*. Climatic Research Institute Report No 29, Oregon State University.
- Esbensen, S. K. and R. W. Reynolds, 1981: Estimating monthly averaged air-sea transfers of heat and momentum using the bulk aerodynamic method. *J. Phys. Oceanogr.*, 11, 457-465.
- Fissel, D. B., S. Pond and M. Miyake, 1977: Computation of surface fluxes from climatological and synoptic data. *Mon. Wea Rev.*, 105, 26-26.
- Friehe, C. A. and K. F. Schmitt, 1976: Parameterisation of air-sea interface fluxes of sensible heat and moisture by the bulk aerodynamic formulas. *J. Phys. Oceanogr.*, 6, 801-809.
- Garrett, C., R. Outerbridge and K. Thompson, 1993: Interannual variability in Mediterranean heat and buoyancy fluxes. *Journal of Climate*, 6, 900-910.
- Gaspar, P. H., J. C. Andre and J. M. Lefreuve, 1990: The determination of the latent and sensible heat fluxes at the sea surface viewed as an inverse problem. *J. Geophys. Res.*, 95(C9), 16169-16178.
- Hall, M. M. and H. L. Bryden, 1982: Direct estimates and mechanisms of ocean heat transport. *Deep Sea Research*, 29, 339-359.
- Hasenrath, S. and P. J. Lamb, 1977: *Climatic atlas of the Tropical Atlantic and Eastern Pacific Oceans.*, University of Wisconsin Press, 105 pp.
- Hasse, L., 1970: The sea surface temperature deviation and the heat flow at the sea-air interface. *Boundary-Layer Meteorol.*, 1, 368-379.
- Holland, J. Z., 1972: Comparative evaluation of some BOMEX measurements of sea surface evaporation, energy flux and stress. *J. Phys. Oceanogr.*, 2, 476-486.
- Hsiung, J., 1985: Estimates of global meridional heat transport. *J. Phys. Oceanogr.*, 15, 1405-1413.

- Hsiung, J., 1986: Mean surface energy fluxes over the global ocean. *J. Geophys. Res.*, 91(C9), 10585-10606.
- Isemer, H.-J. and L. Hasse, 1987: *The Bunker climate atlas of the North Atlantic Ocean. Vol. 2: Air-sea interactions.*, Springer-Verlag, 252 pp.
- Isemer, H.-J., J. Willebrand and L. Hasse, 1989: Fine adjustment of large scale air-sea energy flux parameterizations by direct estimates of ocean heat transport. *Journal of Climate*, 2(10), 1173-1184.
- Kaufeld, L., 1985: The development of a new Beaufort equivalent scale. *Meteorol. Rundsch.*, 34, 17-23.
- Kent, E. C. and R. W. Pascal, 1992: *Project SOFIA: IOS Cruise Report.* James Rennell Centre for Ocean Circulation.
- Kent, E. C. and P. K. Taylor, 1991: *Ships observing marine climate: a catalogue of the voluntary observing ships participating in the VSOP-NA.* Marine Meteorology and Related Oceanographic Activities 25, World Meteorological Organisation.
- Kent, E. C. and P. K. Taylor, 1994: A comparison of sensible and latent heat flux estimates for the North Atlantic Ocean. *submitted.*
- Kent, E. C., P. K. Taylor, B. S. Truscott and J. S. Hopkins, 1993: The accuracy of voluntary observing ship's meteorological observations. *J. Atmos. & Oceanic Tech.*, 10(4), 591-608.
- Kent, E. C., R. J. Tiddy and P. K. Taylor, 1994: Correction of marine daytime air temperature observations for radiation effects. *J. Atmos. & Oceanic Tech.*, 10(6), 900-906.
- Keuttner, J. P. and D. E. Parker, 1976: GATE: Report on the field phase. *Bull. Am. Meteor. Soc.* 63, 370-382.
- Koracin, D. and D. P. Rogers, 1990: Numerical simulations of the response of the marine atmosphere to ocean forcing. *Journal of the Atmospheric Sciences*, 47(5), 592-611.
- Kraus, H. and E. Schaller, 1978: Steady-state characteristics of inversions capping a well-mixed planetary boundary layer. *Boundary-Layer Meteorol.*, 14, 83-104.
- Large, W. G. and S. Pond, 1981: Open ocean momentum flux measurements in moderate to strong winds. *J. Phys. Oceanogr.*, 11, 324-336.
- Large, W. G. and S. Pond, 1982: Sensible and latent heat flux over the sea. *J. Phys. Oceanogr.*, 12, 464-482.

- Lean, J., 1992: A guide to the UK Meteorological Office Single Column Model. *Hadley Centre Internal Report, April 1992*. 43pp.
- Lilly, D. K., 1968: Models of cloud-topped mixed layers under a strong inversion. *Q. J. Roy. Met. Soc.*, 94, 292-309.
- Liu, W. T., 1984: Estimation of latent heat flux with SeaSat-SMMR, a case study in N. Atlantic. *Large-scale oceanographic experiments and satellites*, C. Gautier and M. Fieux, Ed., D Reidel Publishing Company, 205-222.
- Liu, W. T., 1987: Comment on "The effect of inaccuracies in weather-ship data on bulk-derived estimates of flux, stability and sea-surface roughness". *J. Atmos. & Oceanic Tech.*, 4(3), 527-529.
- Liu, W. T., 1990: Remote sensing of surface turbulent heat flux. *Surface waves and fluxes Volume 2 - Remote sensing*, G. L. Geernaert and W. J. Plant, Ed., Kluwer Academic Publishers, 293-309.
- Liu, W. T., K. B. Katsaros and J. A. Businger, 1979: Bulk parameterization of air-sea exchanges of heat and water vapour including the molecular constraints at the interface. *Journal of the Atmospheric Sciences*, 36, 1722-1735.
- Liu, W. T. and P. P. Niiler, 1984: Determination of monthly mean humidity in the atmospheric surface layer over oceans from satellite data. *J. Phys. Oceanogr.*, 14, 1451-1457.
- Lumb, F. E., 1964: The influence of cloud on hourly amounts of total solar radiation at the sea surface. *Quarterly Journal of the Royal Meteorological Society.*, 90, 43-56.
- Mellor, G. L., 1977: The Gaussian cloud model relations. *J. Atmos. Sci.*, 34, 356-358.
- Miller, J. R., 1981: Variations in upper ocean heat storage determined from satellite data. *Remote Sensing Environment*, 11, 473-482.
- Nicholls, S., 1983: An observational study of the mid-latitude, marine, atmospheric boundary layer. PhD dissertation, University of Southampton.
- Nicholls, S., 1984: The dynamics of stratocumulus: Aircraft observations and comparisons with a mixed-layer model. *Q. J. Roy. Met. Soc.*, 110, 783-820.
- Oberhuber, J. M., 1988: *An atlas based on the COADS data set: The budgets of heat, buoyancy and turbulent kinetic energy at the surface of the global ocean*. Report No. 15, Max-Planck-Institut für Meteorologie.

- Payne, R. E., 1972: Albedo of the sea surface. *Journal of the Atmospheric Sciences*, 29, 959-970.
- Pollard, R. T., T. H. Guymer and P. K. Taylor, 1983: Summary of the JASIN 1978 field experiment. *Phil. Trans. Roy. Soc. London*, 308(A), 221-230.
- Press, W. H., B. P. Flannery, S. A. Teukolsky and W. T. Vetterling, 1989: *Numerical Recipes*, Cambridge University Press, 702 pp.
- Quayle, R. G., 1980: Climatic Comparisons of Estimated and Measured Winds from Ships. *J. Appl. Meteorol.*, 19, 142-156.
- Rago, T. A. and H. T. Rossby, 1987: Heat transport into the North Atlantic Ocean north of 32°N latitude. *J. Phys. Oceanogr.*, 17(854-871).
- Robinson, I. S., N. C. Wells and H. Charnock, 1984: The sea surface thermal boundary layer and its relevance to the measurements of sea surface temperature by airborne and spaceborne radiometers. *International Journal of Remote Sensing*, 5, 19-45.
- Rogers, D. P., 1983: A numerical model of the cloudy marine boundary layer. PhD dissertation, University of Southampton.
- Rogers, D. P. and K. Koracin, 1992: Radiative transfer and turbulence in the cloud-topped marine atmospheric boundary layer. *Journal of the Atmospheric Sciences*, 49(16), 1473-1486.
- Roll, H. U., 1965: *Physics of the marine atmosphere.*, Academic Press.
- Schubert, W. H., 1976: Experiments with Lilly's cloud-topped mixed layer model. *Journal of the Atmospheric Sciences*, 33, 436-446.
- Schulz, J., P. Schlüssel and H. Grassl, 1993: Water vapour in the atmospheric boundary layer over oceans from SSM/I measurements. *International Journal of Remote Sensing*, 14(15), 2773-2789.
- Schutz, C. and W. L. Gates, 1971: *Global climatic data for surface, 800mb, 400mb: January*. R-915-ARPA, The Rand Corporation, Santa Monica.
- Schutz, C. and W. L. Gates, 1972: *Global climatic data for surface, 800mb, 400mb: July*. R-1029-ARPA, The Rand Corporation, Santa Monica.
- Schutz, C. and W. L. Gates, 1974: *Global climatic data for surface, 800mb, 400mb: October*. R-1425-ARPA, The Rand Corporation, Santa Monica.
- Siebesma, A. P. and J. W. M. Cuijpers, 1994: Evaluation of parametric assumptions for shallow cumulus convection. Unpublished report, KNMI.

- Simmonds, I. and M. Dix, 1989: The use of mean atmospheric parameters in the calculation of modelled mean surface heat fluxes over the world's oceans. *J. Phys. Oceanogr.*, 19, 205-215.
- Smith, S. D., 1988: Coefficients for sea surface wind stress, heat flux and wind profiles as a function of wind speed and temperature. *J. Geophys. Res.*, 93, 15467-15474.
- Smith, S. D., 1989: Water Vapour Flux at the Sea Surface. *Boundary-Layer Meteorol.*, 47, 277-293.
- Smith, S. D. and F. W. Dobson, 1984: The heat budget at Ocean Weather Station Bravo. *Atmosphere-Ocean*, 22(1), 1-22.
- Stage, S. A. and J. A. Businger, 1981a: A model for entrainment into a cloud-topped marine boundary layer. Part I: Model description and application to a cold-air outbreak episode. *J. Atmos. Sci.*, 38, 2213-2229.
- Stage, S. A. and J. A. Businger, 1981b: A model for entrainment into a cloud-topped marine boundary layer. Part II: Discussion of model behaviour and comparison with other models. *J. Atmos. Sci.*, 38, 2230-2242.
- Stull, R. B., 1988: *An introduction to boundary layer meteorology.*, Kluwer Academic Publishers.
- Talley, L. D., 1984: Meridional heat transport in the Pacific Ocean. *J. Phys. Oceanogr.*, 14, 231-241.
- Taylor, P. K., 1982: Remote sensing of atmospheric water content and sea surface latent heat flux. *Remote sensing and the atmosphere*, University of Liverpool, 265-272.
- Taylor, P. K., 1984a: The determination of surface fluxes of heat and water by satellite microwave radiometry and in situ measurements. *Large-scale oceanographic experiments and satellites.*, C. Gautier and M. Fieux, Ed., D Reidel Publishing Company, 223-246.
- Taylor, P. K., 1984b: *The measurement of the ocean surface fluxes of sensible heat, latent heat and water for WOCE.* Annex III in WCP-69, World Climate Research Programme.
- Taylor, P. K., A. L. M. Grant, H. Gunther and G. Olbruck, 1983: Mass, momentum, sensible heat and latent heat budgets for the lower atmosphere. *Phil. Trans. Roy. Soc. London*, 308(A), 275-290.
- Tennekes, H., 1973: Similarity laws and scale relations in planetary boundary layers. *Workshop on Micrometeorology*, D. A. Haugen, Ed., American Meteorological Society, 177-216.

- Wagner, D., E. Ruprecht and C. Simmer, 1990: A combination of microwave observations from satellites and an EOF analysis to retrieve vertical humidity profiles over the ocean. *J. Appl. Meteorol.*, 29(11), 1142-1157.
- Weare, B. C., 1989: Uncertainties in estimates of surface heat fluxes derived from marine reports over the tropical and subtropical oceans. *Tellus*, 41A, 357-370.
- Weare, B. C. and P. T. Strub, 1981: The significance of sampling biases on calculated monthly mean oceanic surface heat fluxes. *Tellus*, 33, 211-224.
- Weare, B. C., P. T. Strub and M. D. Samuel, 1980: *Marine atlas of the Tropical Pacific Ocean*. University of California.
- White, A. A. and R. A. Bromley, 1988: *A new set of dynamical equations for use in numerical weather prediction and global climate models*. Meteorological Office 13 Branch Memo.
- WMO, 1970: *The Beaufort scale of wind force*. Commission for Marine Meteorology.
- Wright, P. B., 1988: *An atlas based on the COADS data set: Fields of mean wind, cloudiness and humidity at the surface of the global ocean*. Report No. 14, Max-Planck-Institut für Meteorologie.
- Yamada, T., 1978: *A three-dimensional, second-order closure numerical model of mesoscale circulations in the lower atmosphere: description of the basic model and an application to the simulation of the environmental effects of a large cooling pond*. ANL-RER-78-1, Argonne National Laboratory.
- Yamada, T., 1979: An application of a three-dimensional, simplified second-moment closure numerical model to study atmospheric effects of a large cooling pond. *Atmospheric Environment*, 13, 693-704.
- Zillmann, J. W., 1972: *A study of some aspects of the radiation and the heat budgets of the southern hemisphere oceans*. 26, Bureau of Meteorology, Department of the Interior, Canberra, Australia.



6. FIGURES

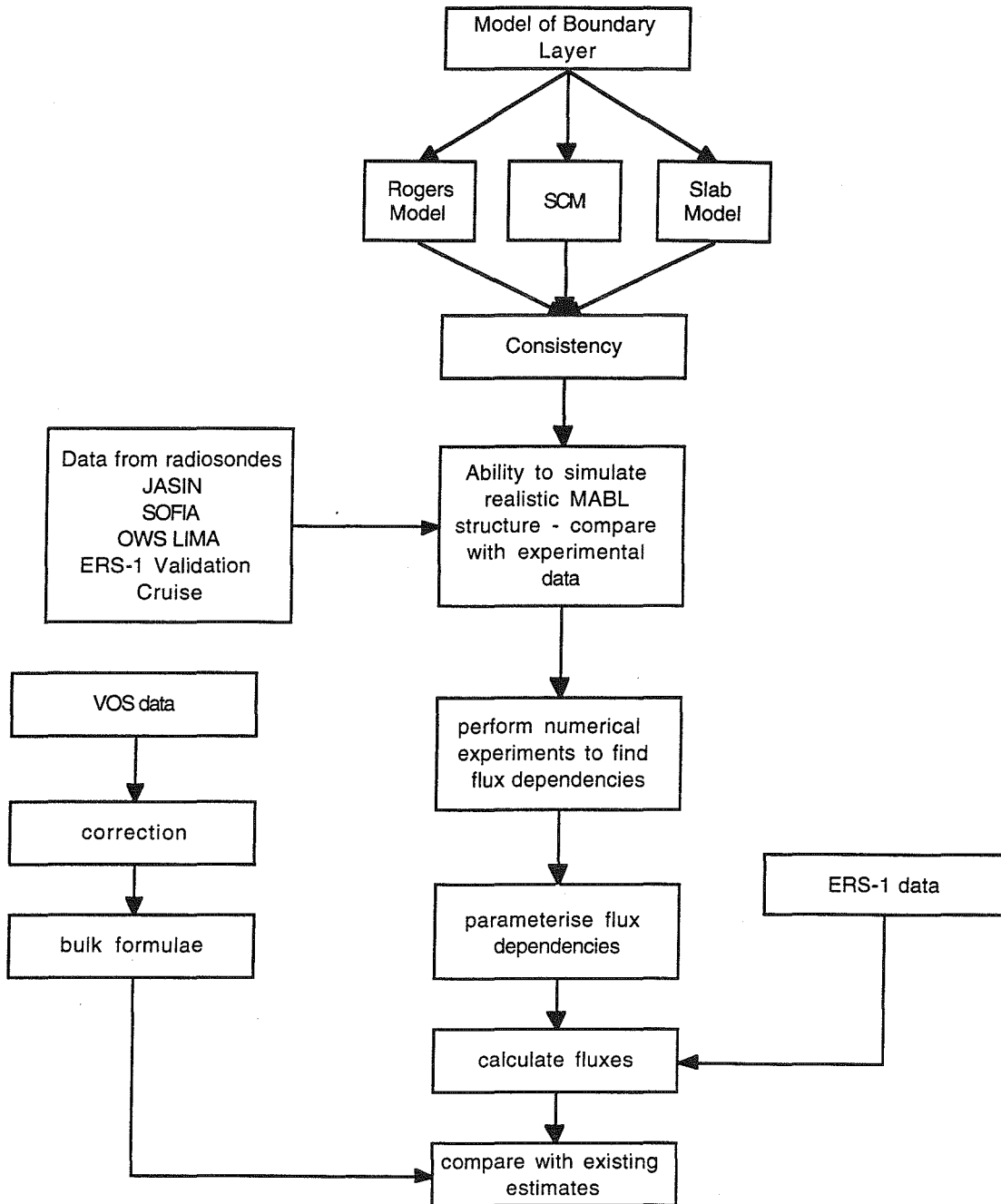


Figure 1 - Flow chart showing steps required in study

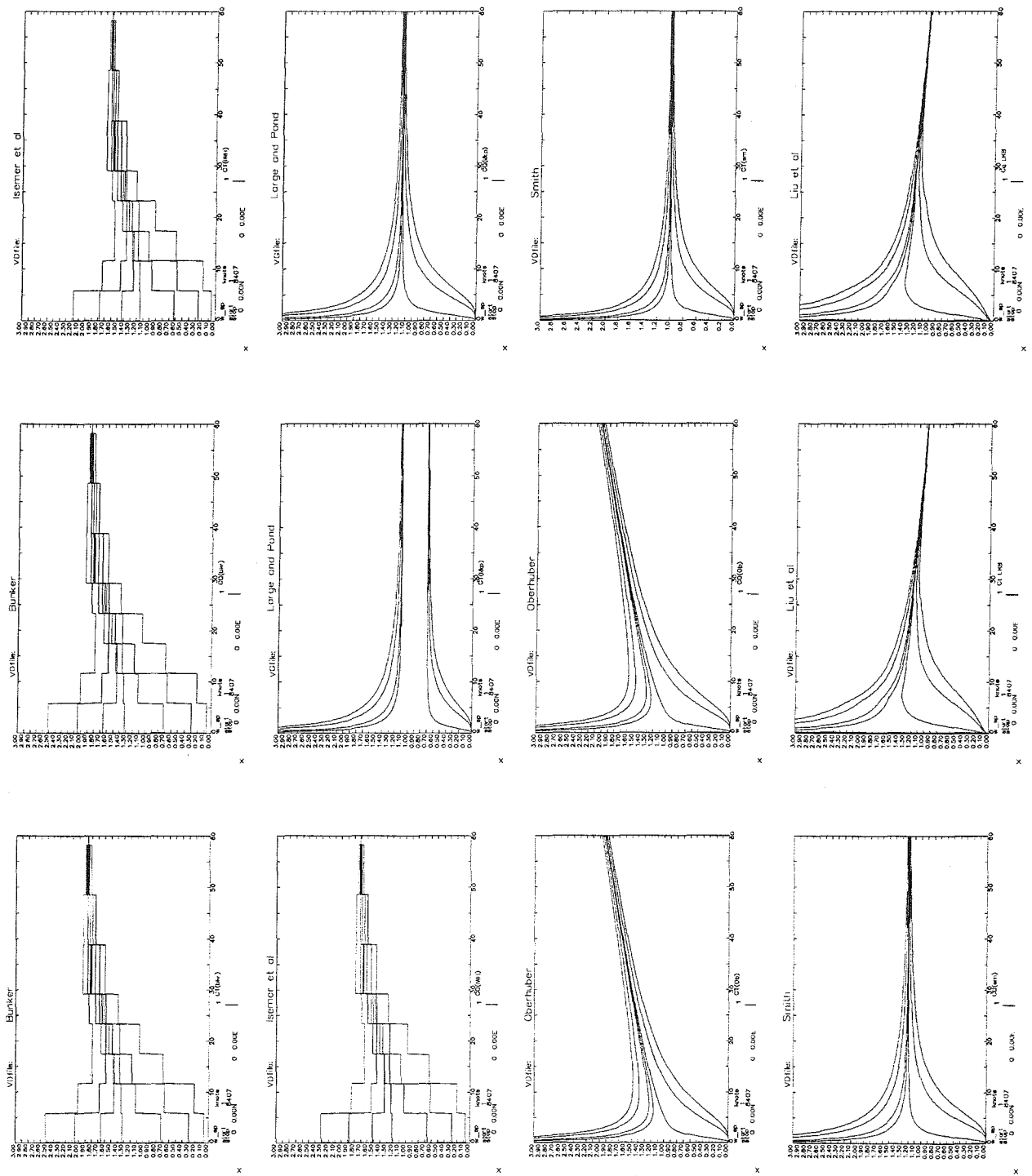


Figure 2 - Transfer coefficients for sensible and latent heat respectively as a function of wind speed (knots) and air-sea temperature difference. Air-sea temperature differences are (bottom to top)  $>5^{\circ}\text{C}$ ,  $4.9$  to  $1.0^{\circ}\text{C}$ ,  $0.9$  to  $0.2^{\circ}\text{C}$ ,  $0.1$  to  $-0.2^{\circ}\text{C}$ ,  $-0.3$  to  $-1.0^{\circ}\text{C}$ ,  $-1.1$  to  $4.9^{\circ}\text{C}$  and  $<-5^{\circ}\text{C}$ . Schemes are (a,b) Bunker (1976), (c,d) Isemer and Hasse (1987), (e,f) Large and Pond (1981;1982), (g,h) Oberhuber (1988), (i,j) Smith 1988;1989 and (k,l) Liu et al (1979).

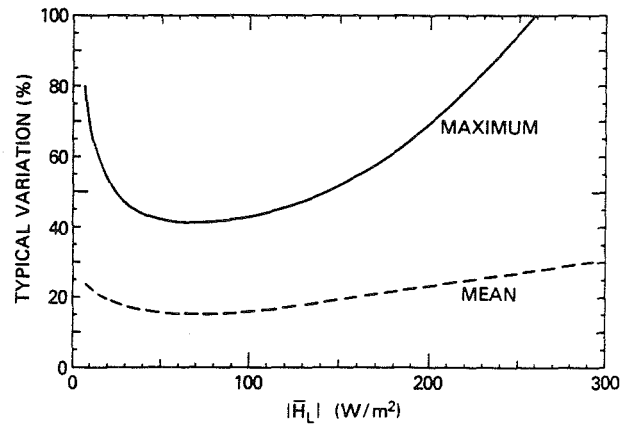
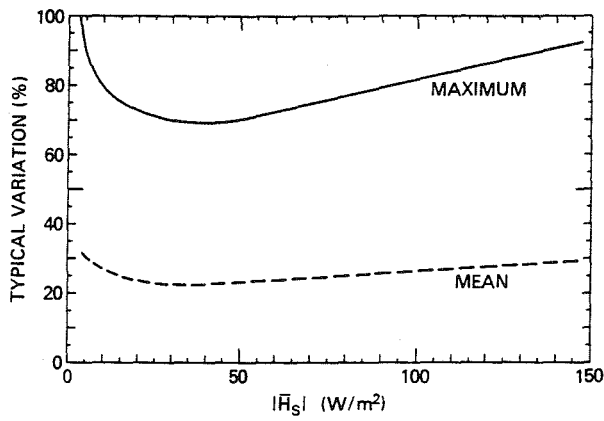
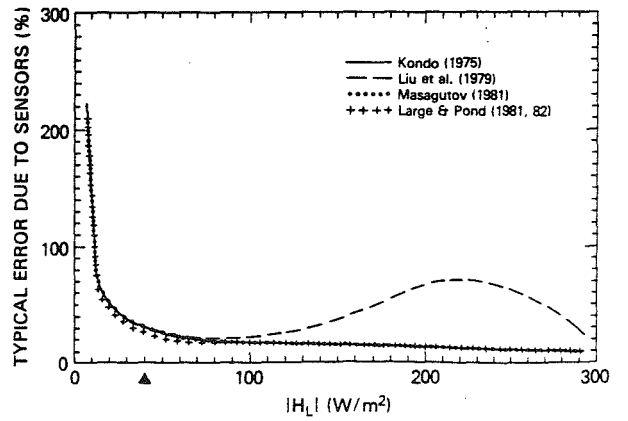
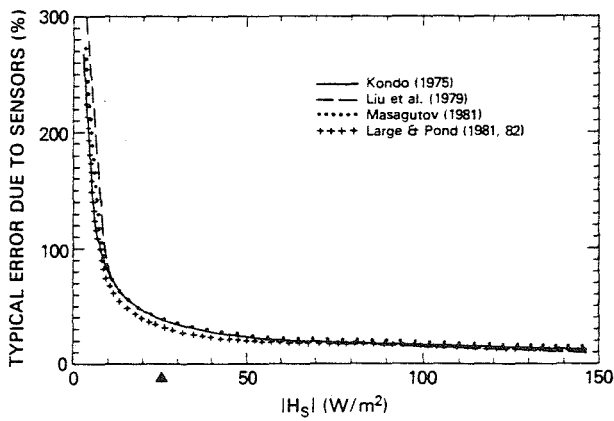


Figure 3 - Typical mean and maximum heat flux variation (%) between 10 transfer coefficient schemes as a function of the consensus heat flux (from Blanc 1985)

a) Sensible Heat

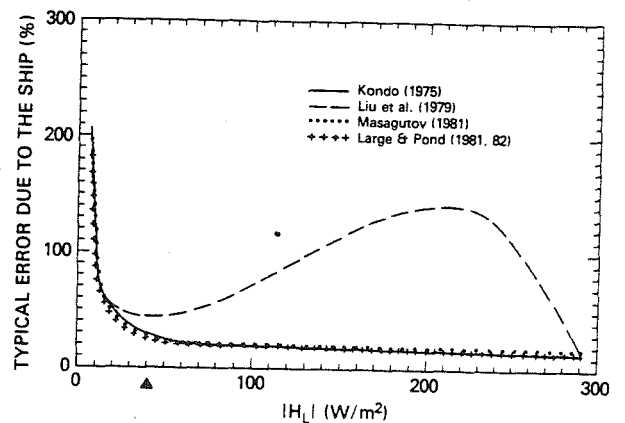
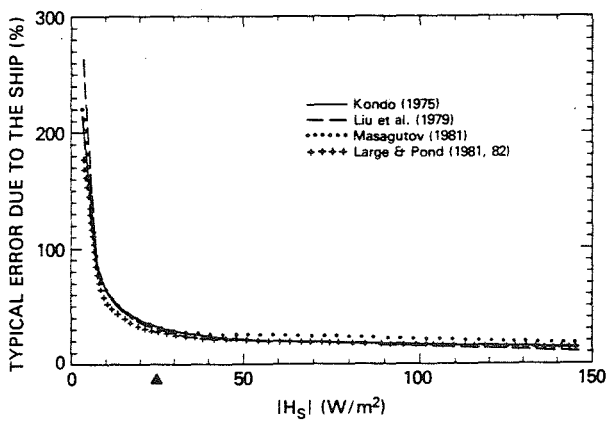
b) Latent Heat



Typical mean and maximum heat flux variation (%) due to sensor error as a function of the consensus heat flux (from Blanc 1986)

c) Sensible Heat

d) Latent Heat



Typical mean and maximum heat flux variation (%) due to ship-induced distortion as a function of the consensus heat flux (from Blanc 1986)

e) Sensible Heat

f) Latent Heat

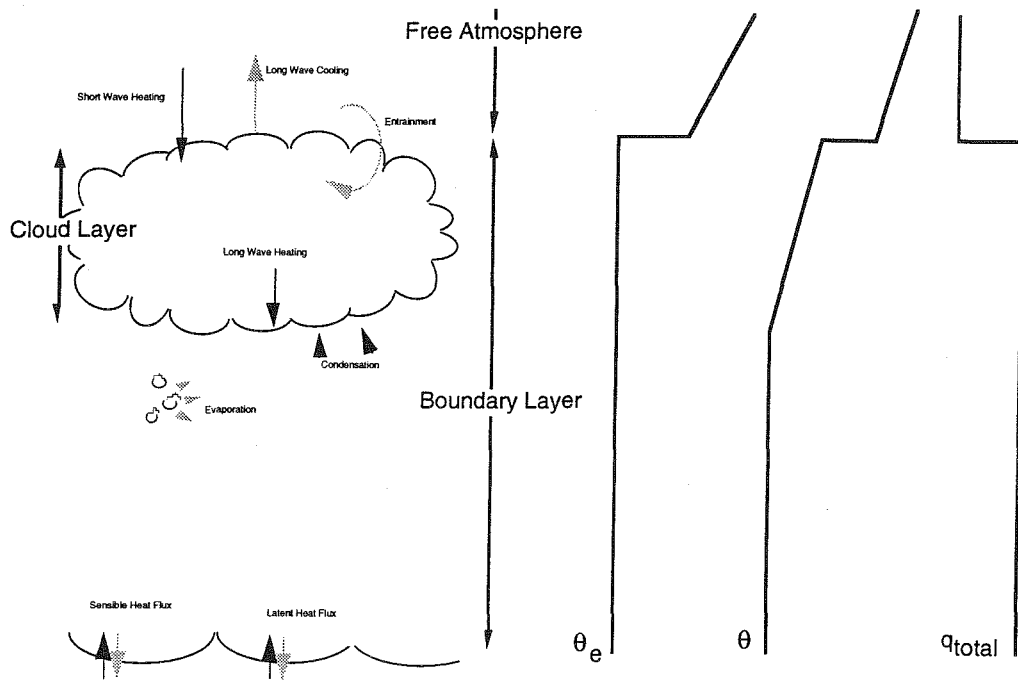


Figure 4 - Schematic diagram of boundary layer processes. Black arrows indicate heat input to the atmosphere and grey arrows heat sinks. Also shown are idealised profiles of equivalent potential temperature, potential temperature and total water mixing ratio.

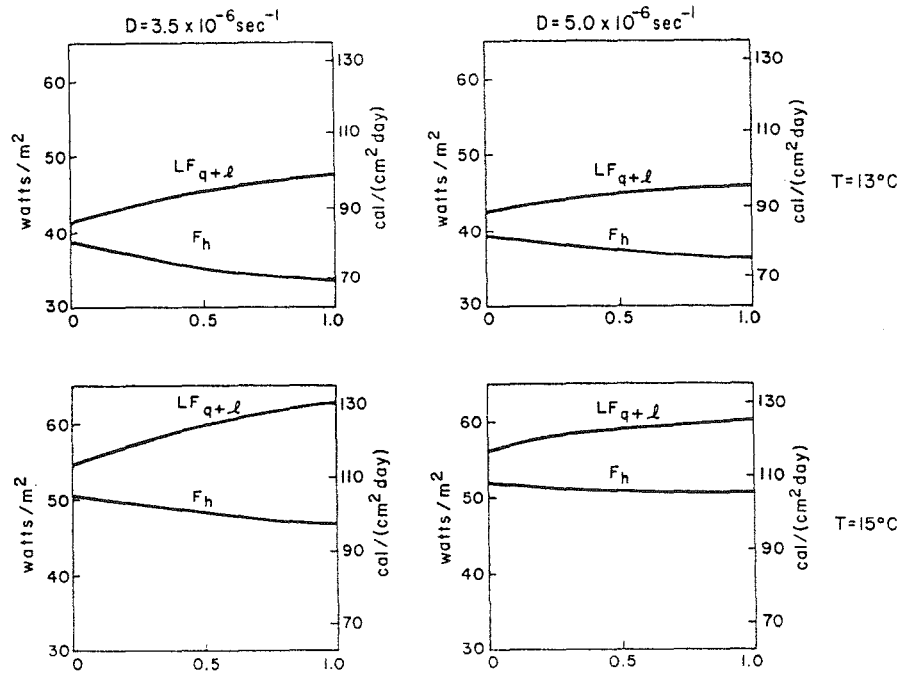


Figure 5 - Dependence of the fluxes of moist static energy ( $F_h$ ), and total water ( $F_{q+l}$ ) on the entrainment parameter  $k$ , ( $x$ -axis), the large scale divergence ( $D$ ) and the SST ( $T$ ).  $k=1$  corresponds to the maximum entrainment condition. From Schubert (1976).

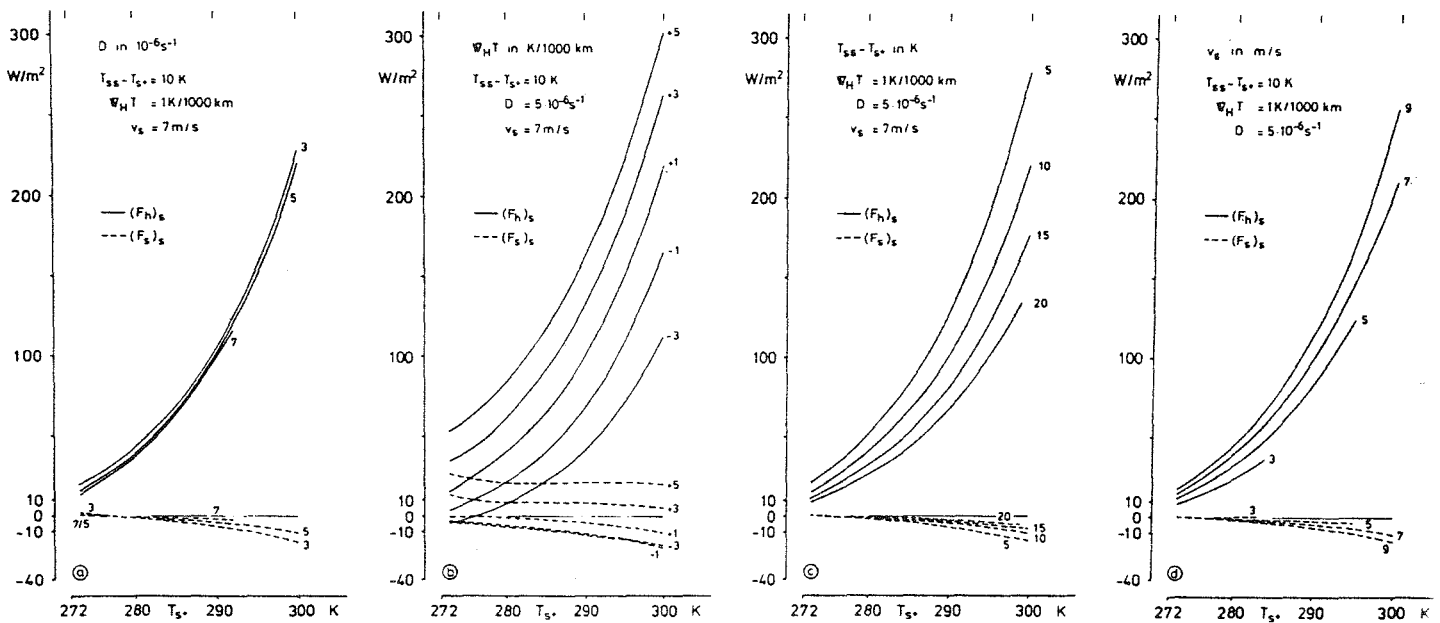


Figure 6 - Dependence of the fluxes of dry static energy ( $F_s$ ) and moist static energy ( $F_h$ ) on SST ( $x$ -axis), the large scale divergence ( $D$ ), the horizontal gradient of SST in the upwind direction ( $\nabla_H T$ ), the difference between the SST and the extrapolation of the lapse rate above the inversion to the sea surface ( $T_{ss} - T_{s+}$ ) and  $v_s$  the 10m wind speed. From Kraus and Schaller (1978).

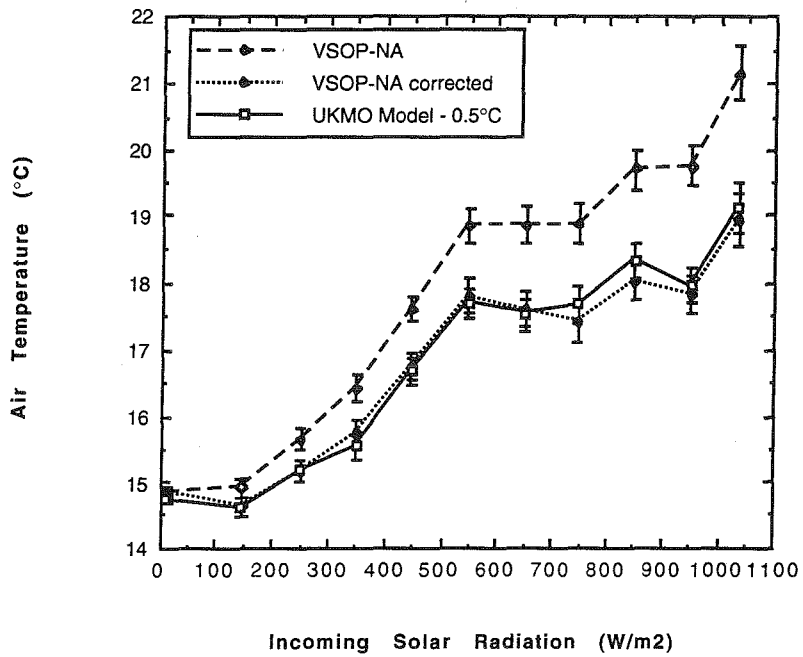


Figure 7 - Air temperature (°C) from UKMO model, and from the VSOP-NA both before and after correction for solar radiation effects plotted as a function of incoming solar radiation (W/m<sup>2</sup>). The model data had an approximately constant bias of 0.5°C from the corrected data and this bias has been subtracted from the model data.

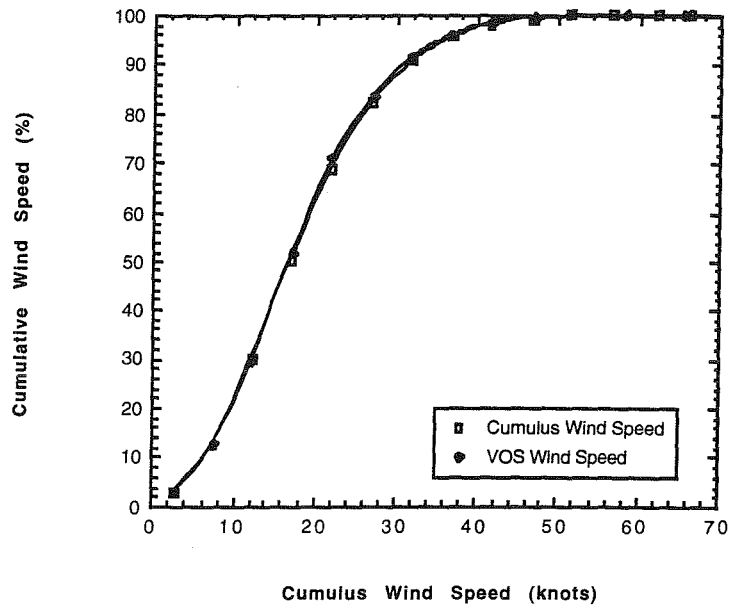


Figure 8a - Cumulative percentage distribution of OWS Cumulus wind data and VOS wind data as a function of OWS Cumulus wind speed at the time of the VOS observation.

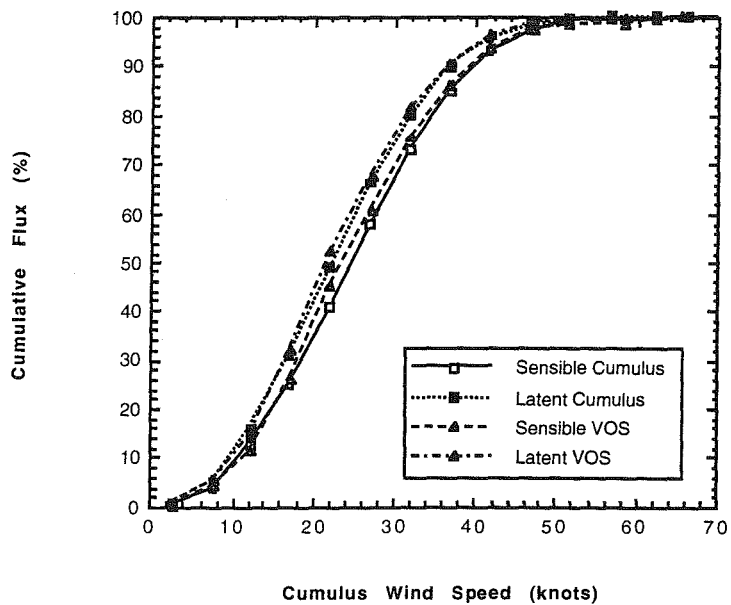


Figure 8b - The cumulative distribution of the total percentage of sensible and latent heat fluxes plotted as a function of OWS Cumulus wind speed.

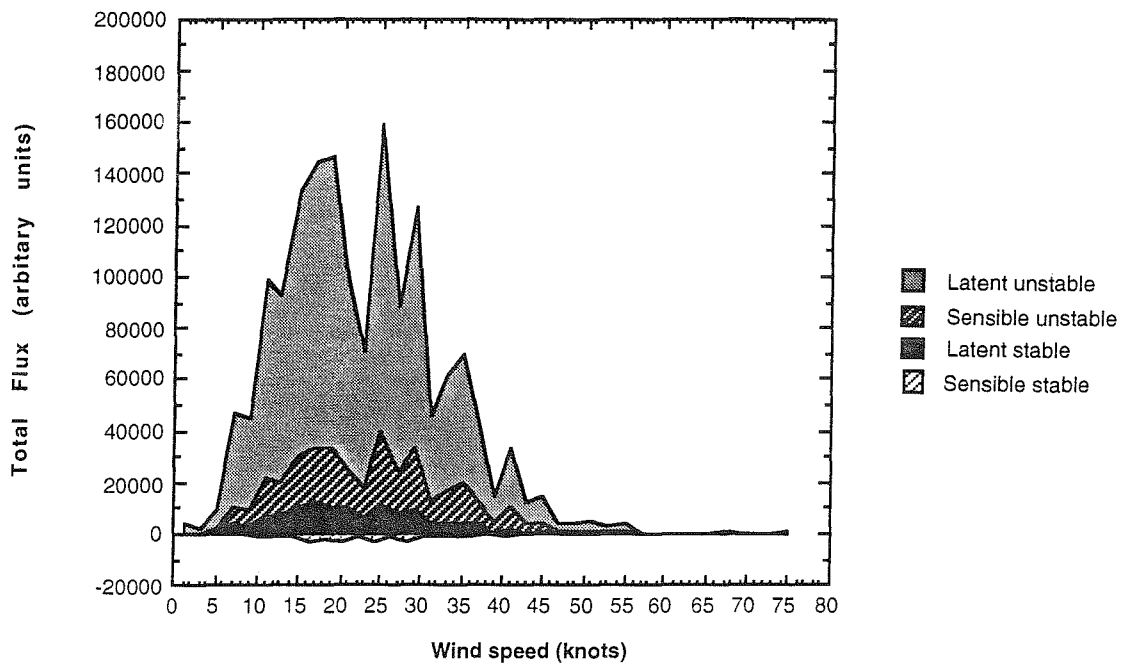


Figure 9 - The total heat flux in 2 knot divisions separately for stable and unstable conditions and for sensible and latent heat flux. The effect of the visual wind reports being biased towards the Beaufort Scale mid-points can clearly be seen as spikes in the data.

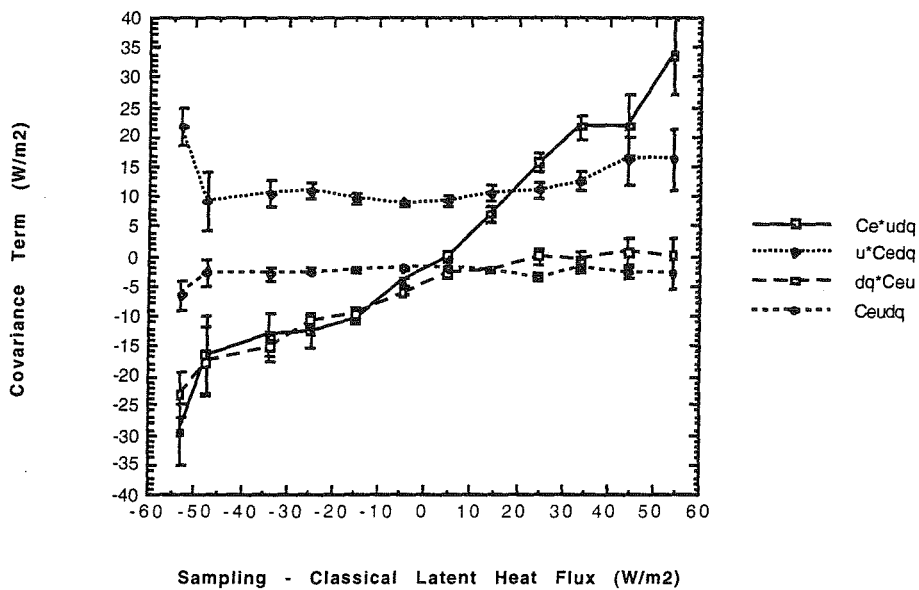
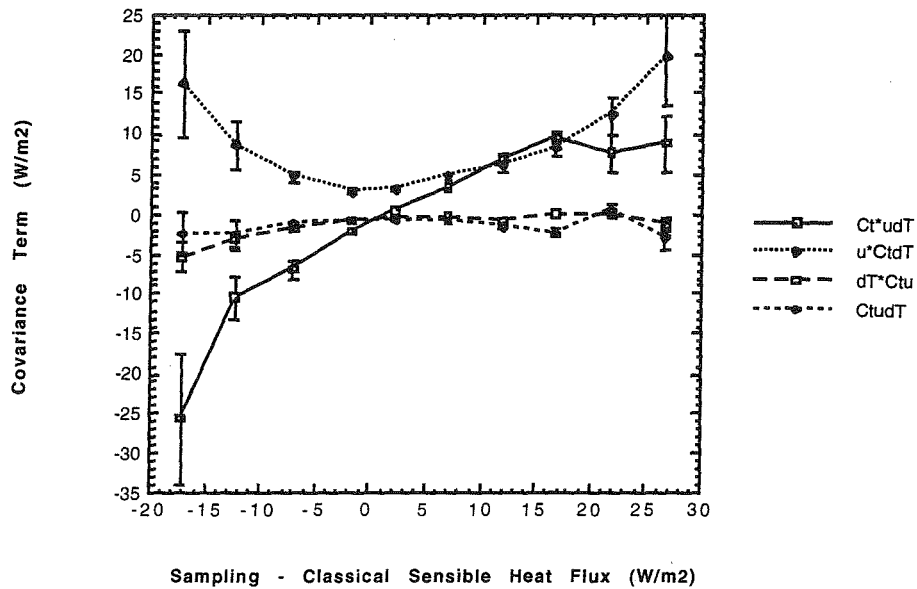


Figure 10 - Covariances contributing to the difference between sampling and classical methods of flux calculation.

$C_T * u * dT = C_T * (\text{covariance between wind speed (u) and air-sea temperature difference (dT)})$

$u * C_T * dT = u * (\text{covariance between } C_T \text{ and } dT)$

$dT * C_T * u = dT * (\text{covariance between } C_T \text{ and } u)$

$C_T * u * dT = \text{triple covariance between } C_T, u \text{ and } dT$

$C_E * u * dq = C_E * (\text{covariance between } u \text{ and air-sea humidity difference (dq)})$

$u * C_E * dq = u * (\text{covariance between } C_E \text{ and } dq)$

$dq * C_E * u = dq * (\text{covariance between } C_E \text{ and } u)$

$C_E * u * dq = \text{triple covariance between } C_E, u \text{ and } dq$

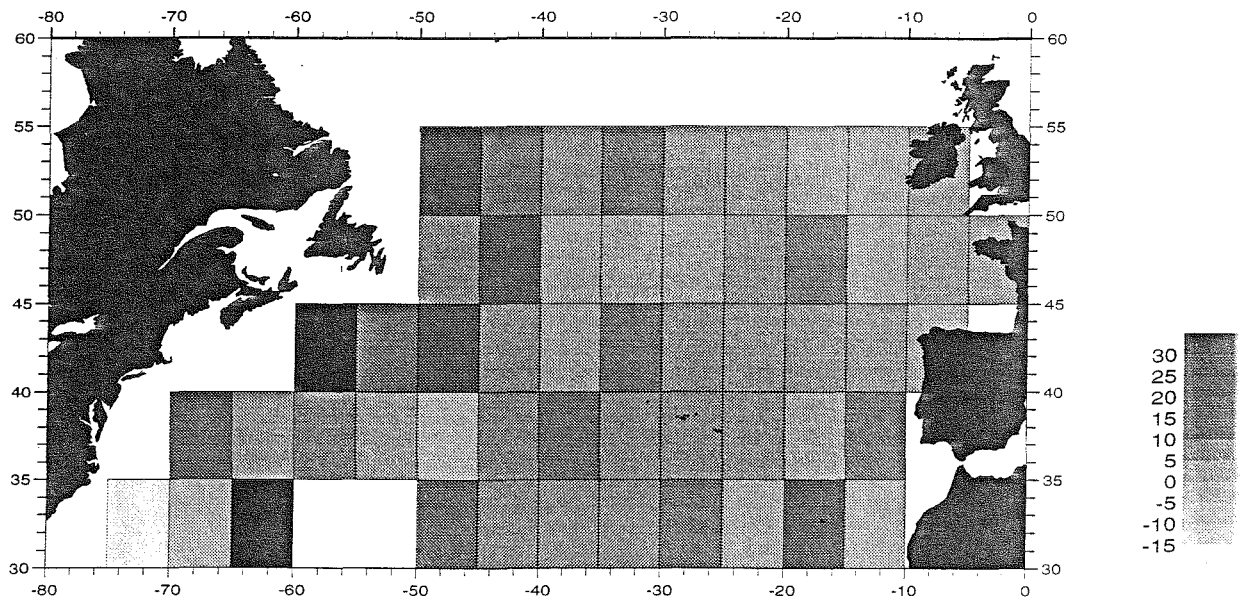
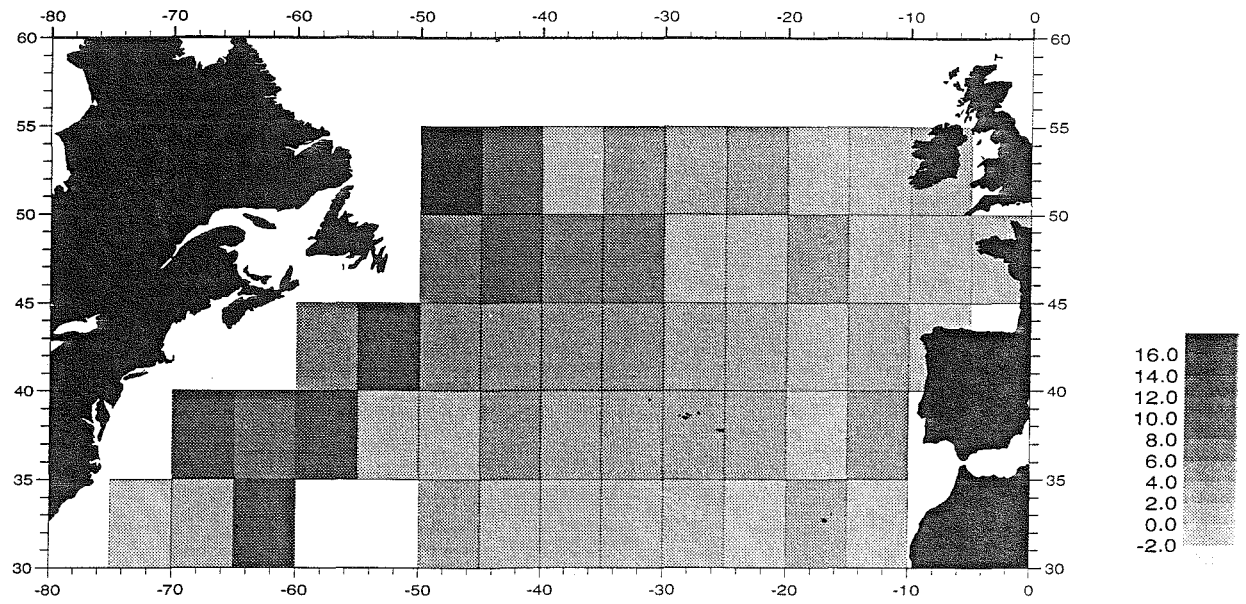


Figure 11 - Difference between sampling and classical heat fluxes in  $W/m^2$  calculated using the transfer coefficient scheme of Oberhuber (1988). Top plot (sampling - classical) sensible heat flux. Bottom plot (sampling - classical) latent heat flux.

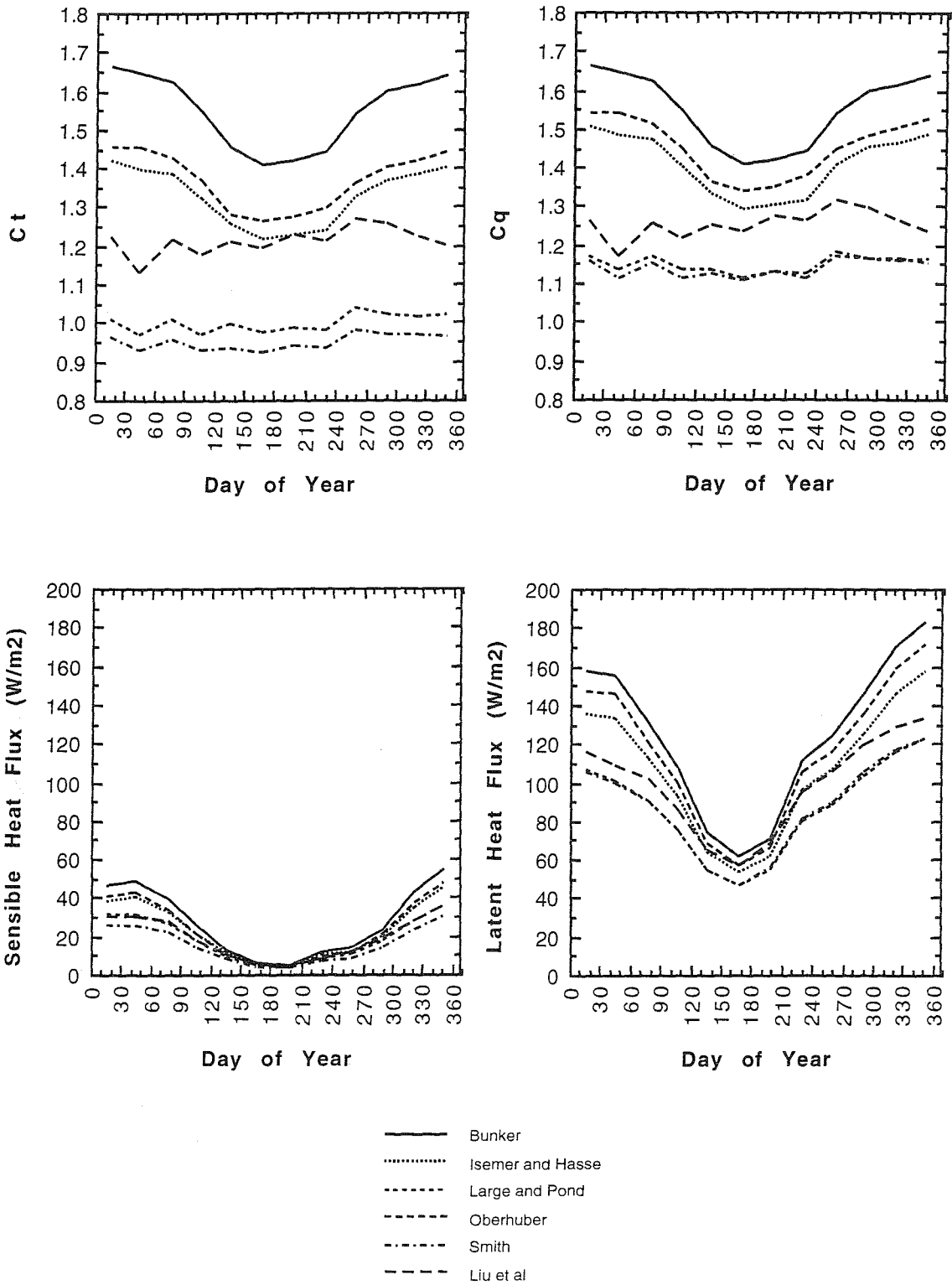


Figure 12 - Monthly mean transfer coefficients and fluxes calculated using six transfer coefficient schemes (see eg section 2.1.1.2).

- a) Transfer Coefficient for Sensible Heat      b) Transfer Coefficient for Latent Heat  
c) Sensible Heat Flux                              d) Latent Heat Flux

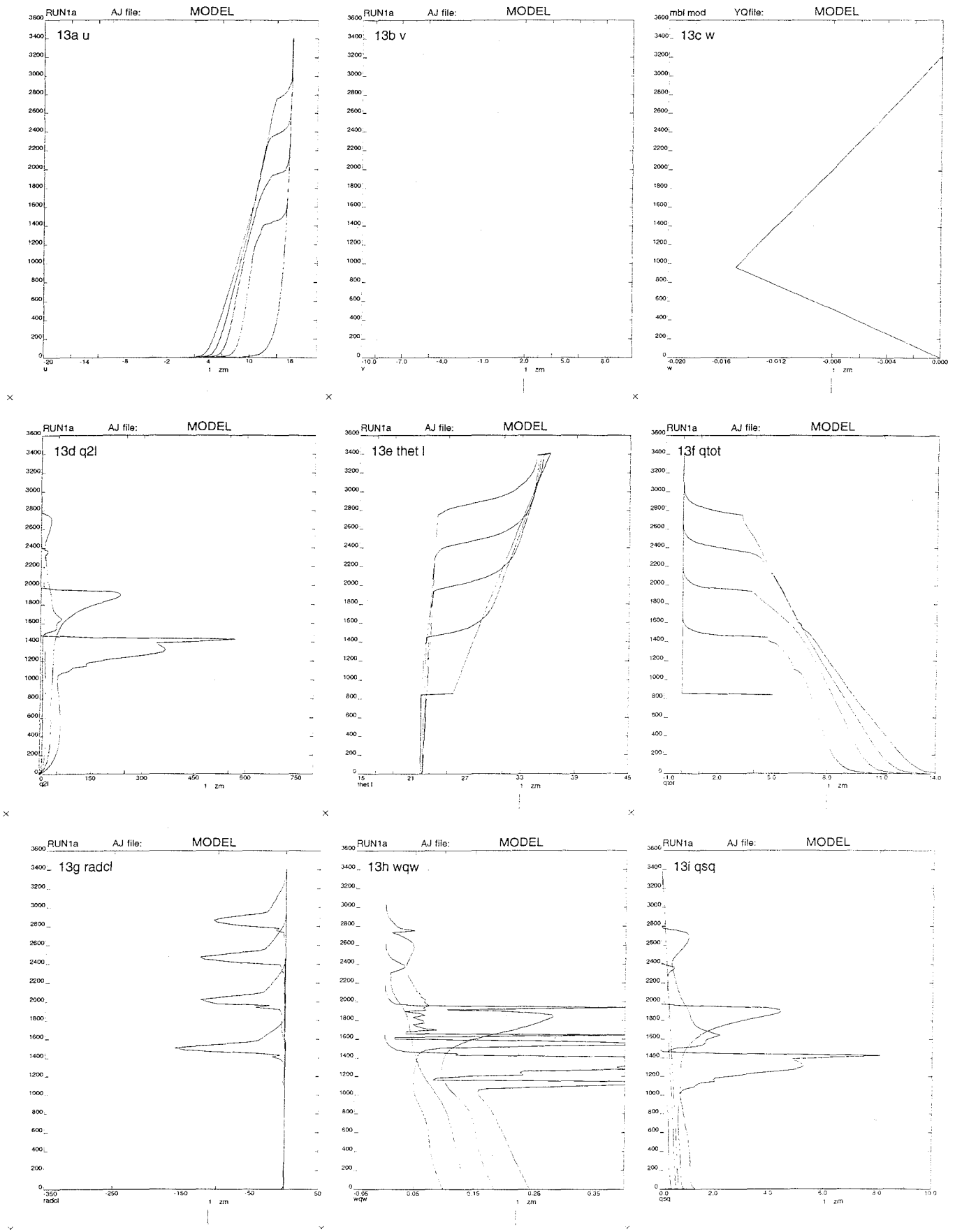


Figure 13 - One minute mean profiles of variables plotted every 12 hours for a 48 hour run as produced by original version of model (Koracin and Rogers 1990). Variables are as given in Table 4.

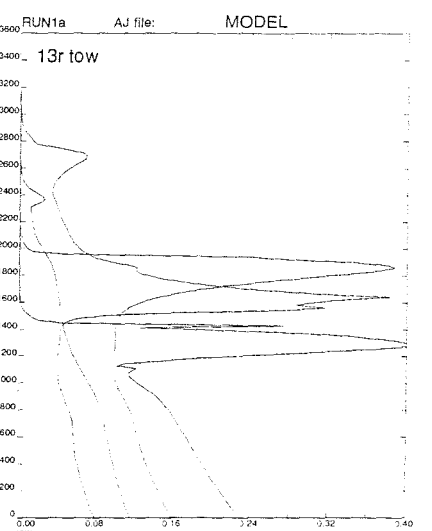
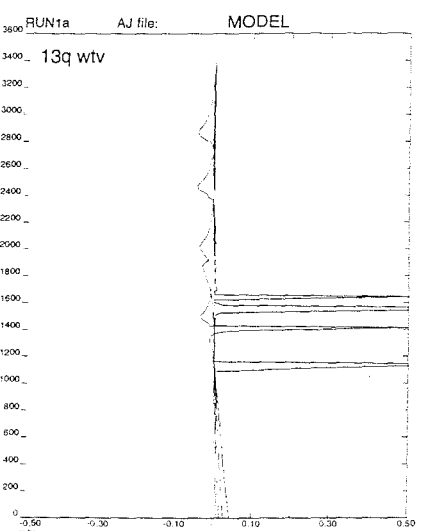
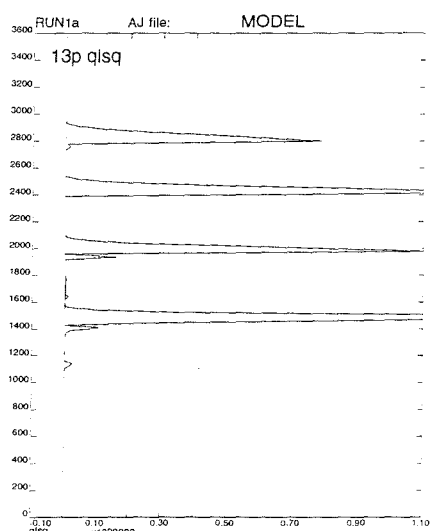
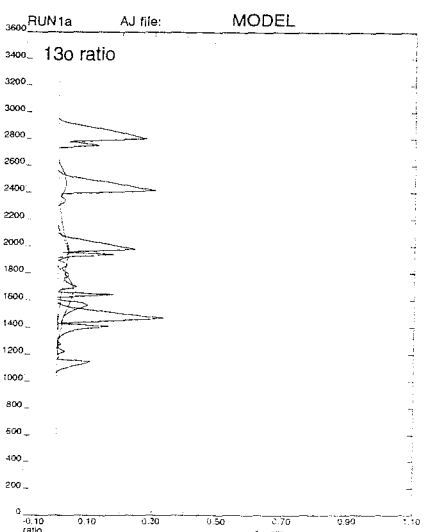
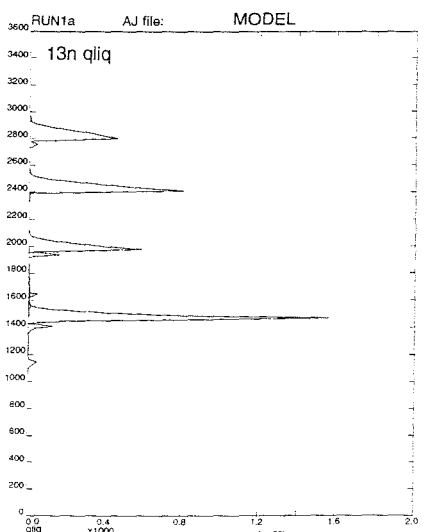
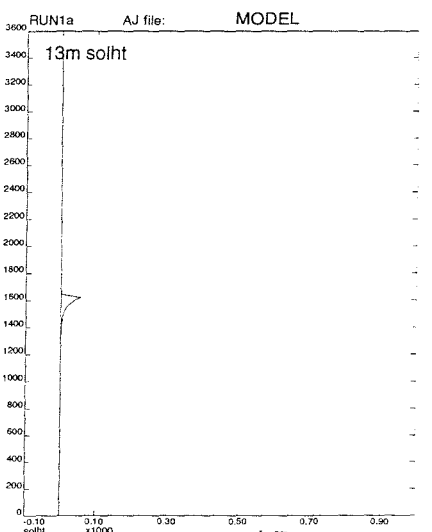
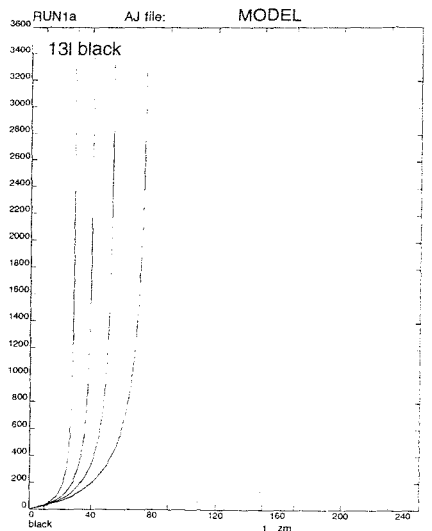
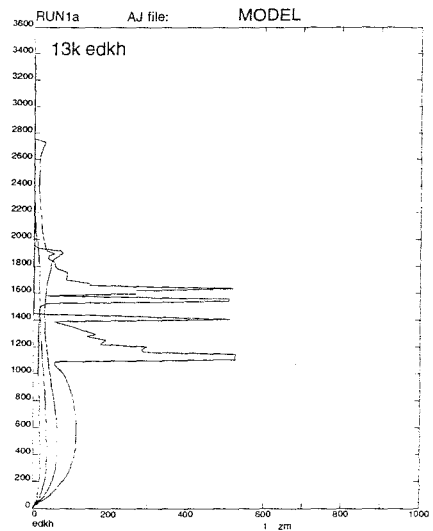
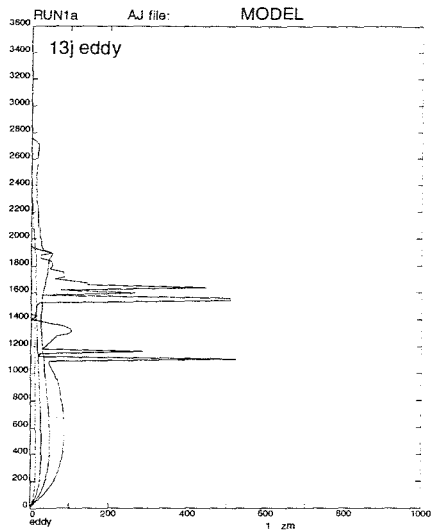


Figure 13 - continued

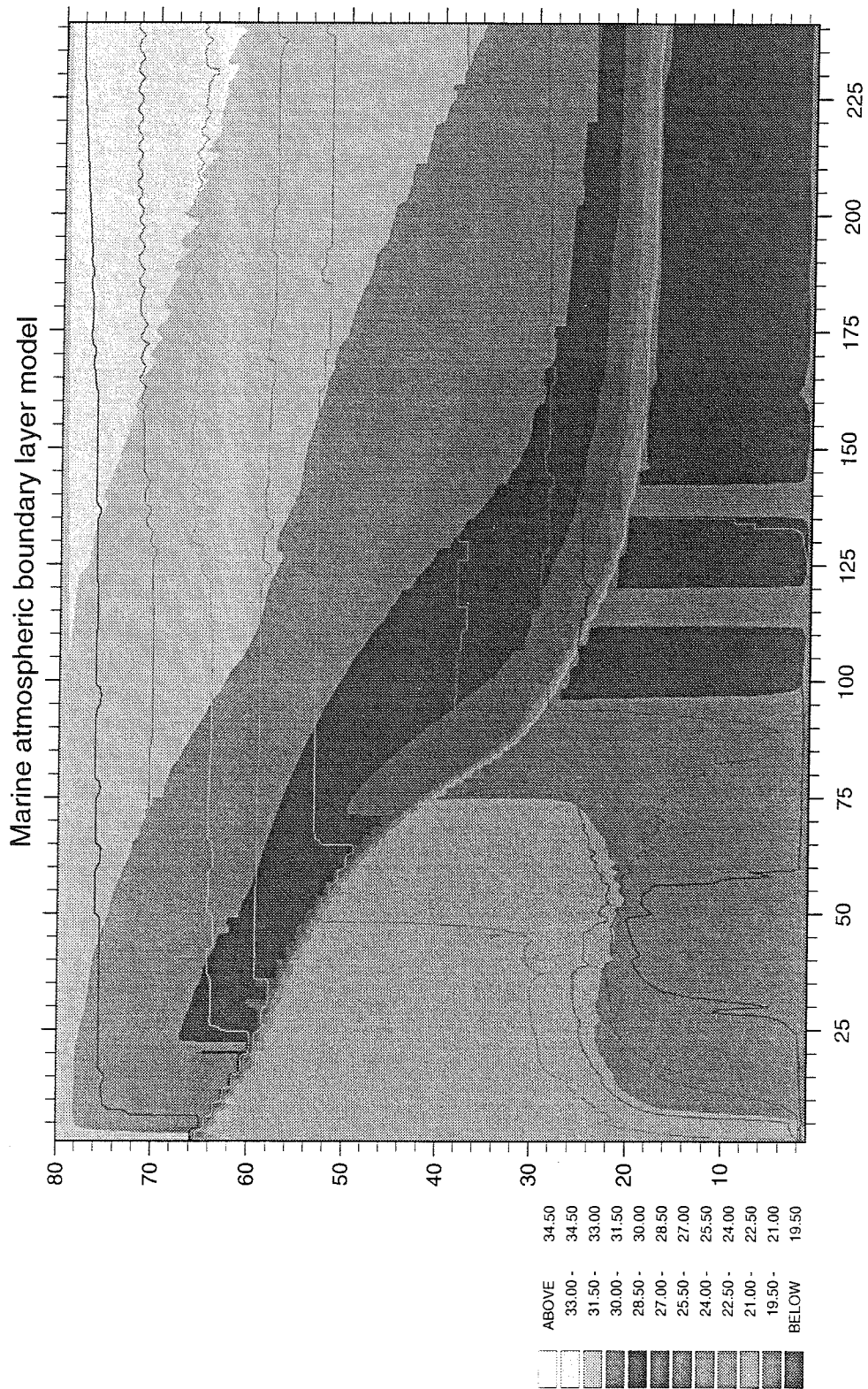


Figure 14 - Contour plot of time evolution of  $\theta$  and water vapour content over 10 days (x-axis in hours ) as a function of model layer (layer 80 is at 2km height) for the original version of the Rogers model. The shaded contours of  $\theta$  can be seen to descend under the influence of the imposed vertical motion whilst the water vapour contours (lines) remain unaffected.

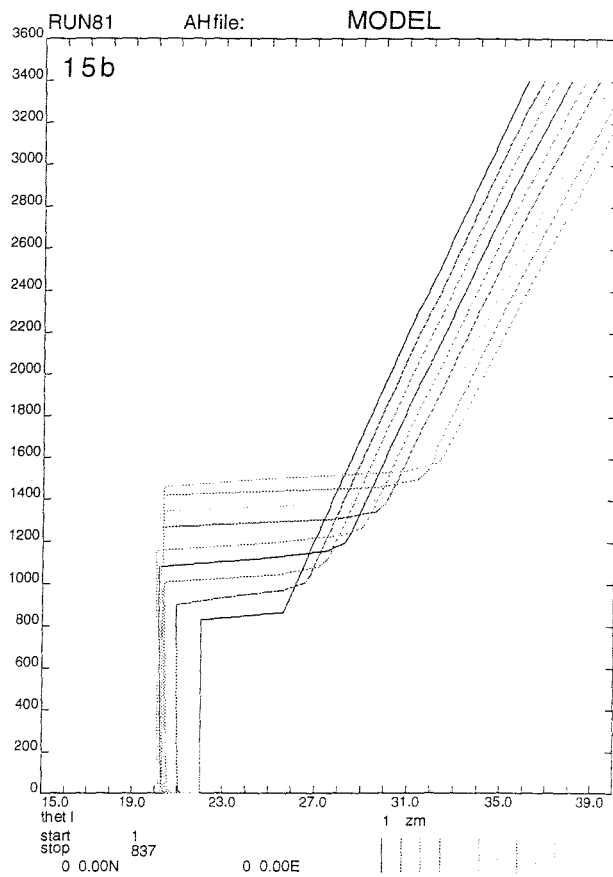
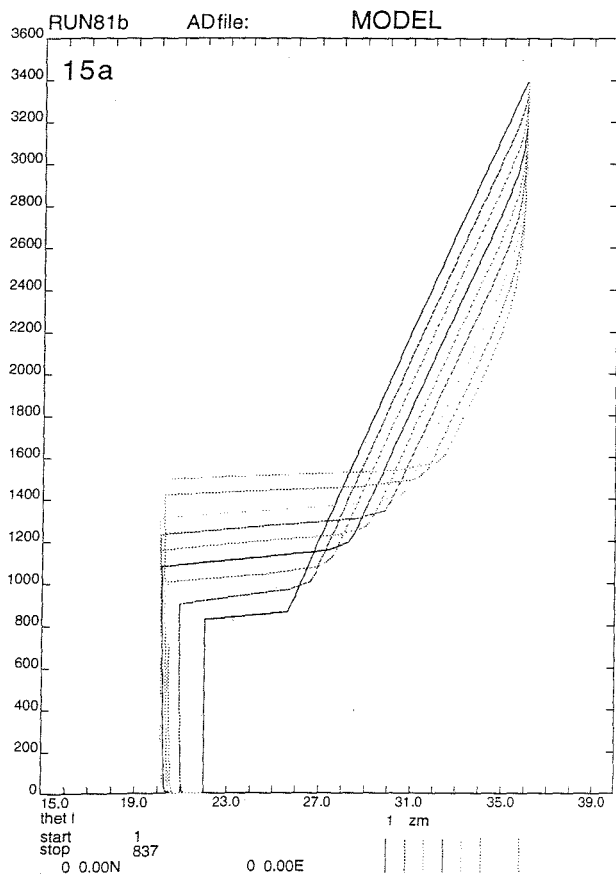


Figure 15 - (a) One minute mean profiles of  $\theta_1$  plotted every 12 hours for a 48 hour run with original boundary condition ( $\theta_1 = \text{const.}$ , see text for details).  
 (b) as (a) but with gradient boundary condition ( $d\theta_1/dz = \text{const.}$ , see text for details).

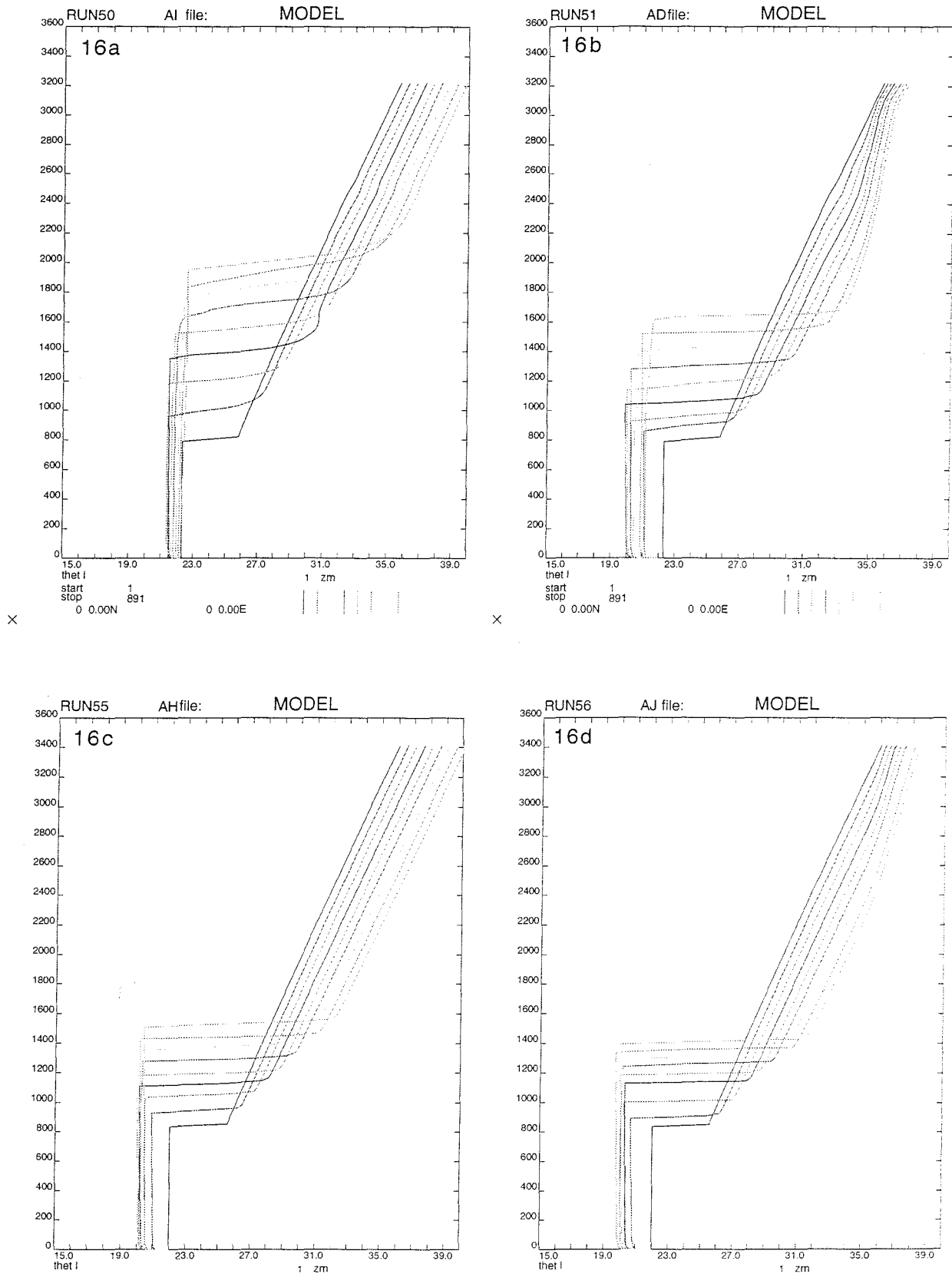


Figure 16 - One minute mean profiles of  $\theta_1$  plotted every 6 hours for a 48 hour run for different profiles of imposed vertical motion,  $w$ .

(a)  $w$  rises linearly from surface to inversion level and then constant to top level minus 1 then,  $w$  is zero at top level. Model grid has coarse resolution near top of model domain.

(b) as (a) but with a more gradual decrease of  $w$  over 3 grid levels at top of model domain.

(c) as (a) but with fine resolution grid throughout model domain.

(d)  $w$  profile as (b), grid resolution as (c).

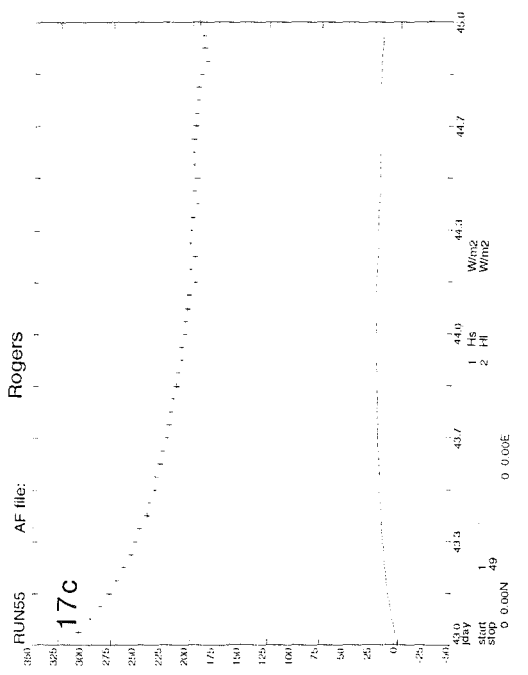
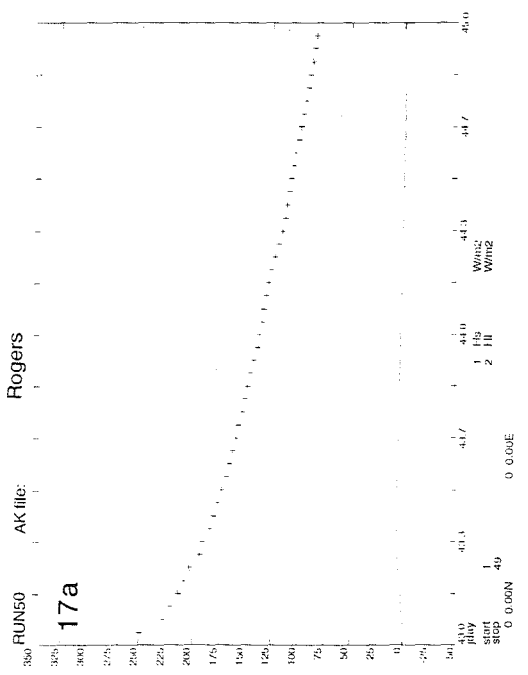
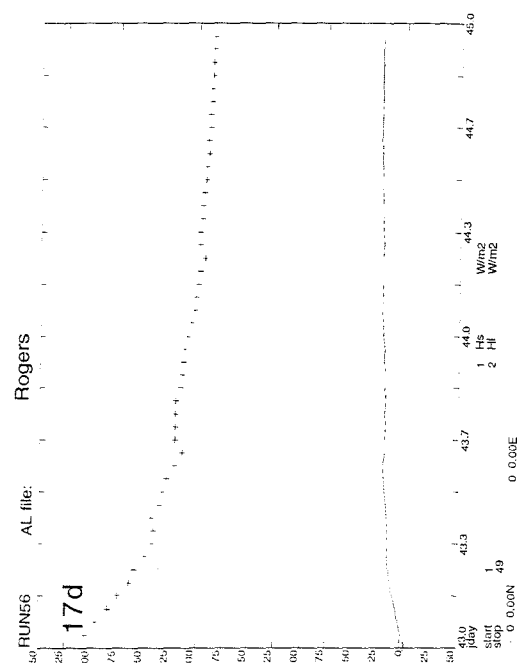
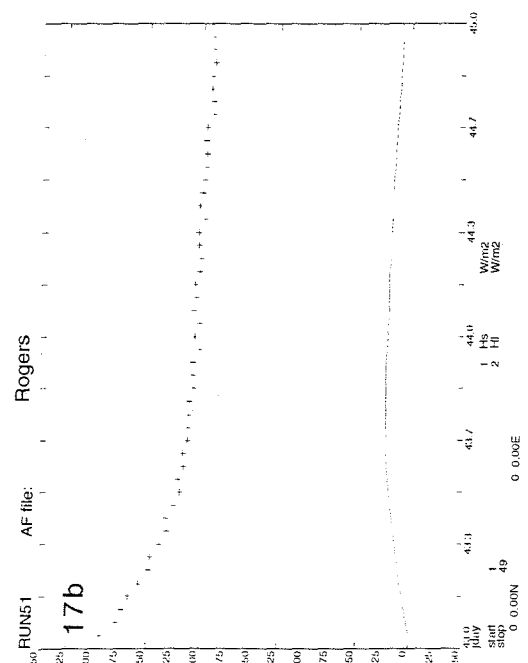


Figure 17 - Time series of surface fluxes of sensible heat (solid line) and latent heat (crosses) for each case as in Figures 16a-d.

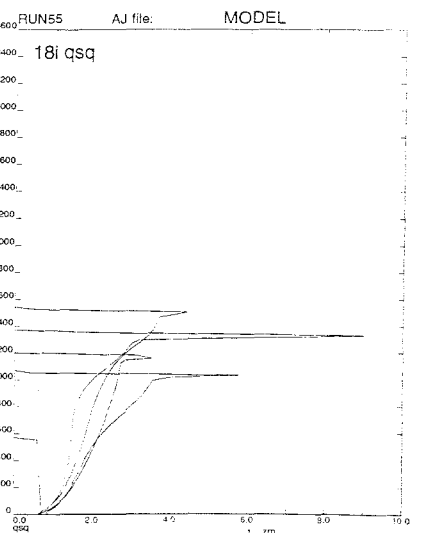
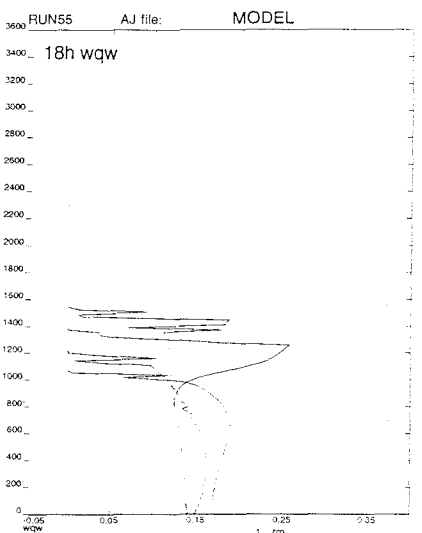
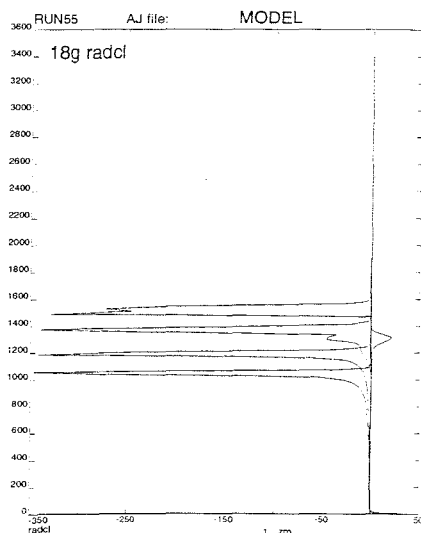
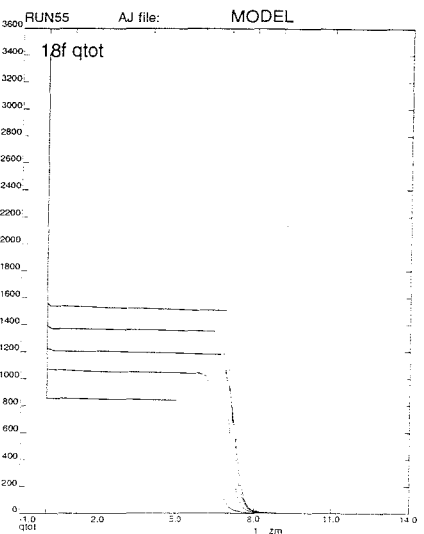
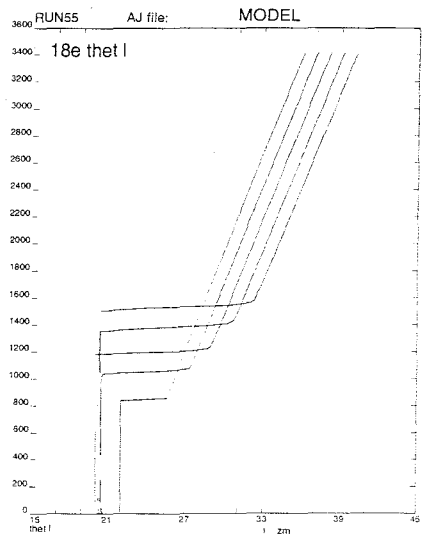
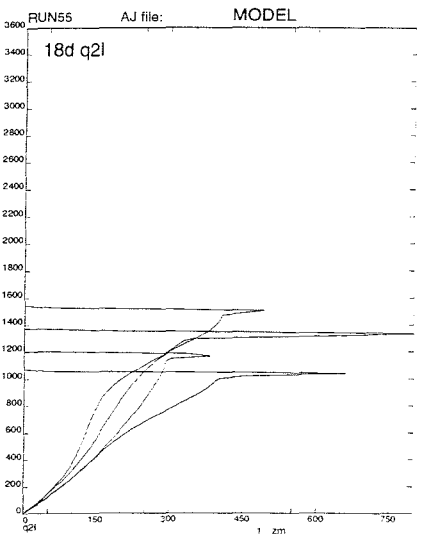
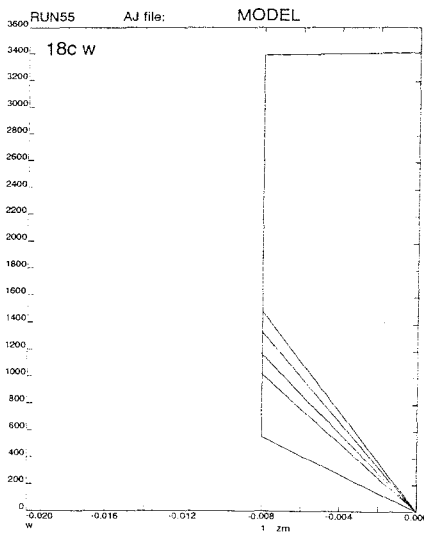
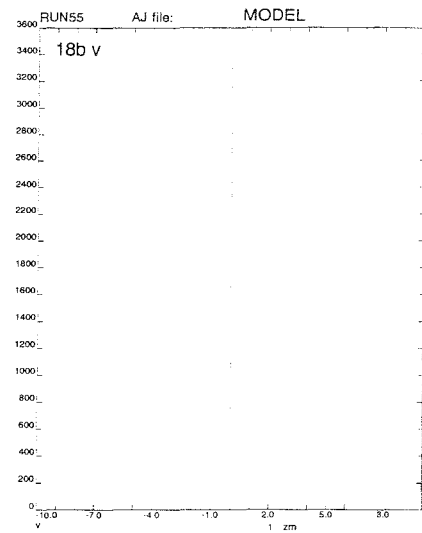
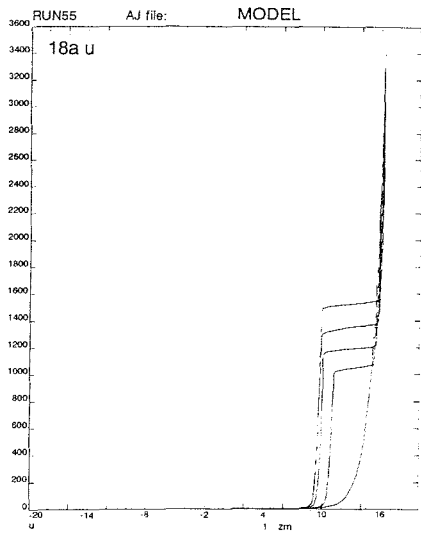


Figure 18 - Model profiles as Figure 13 (see Table 4) for optimum model set up achieved to date.

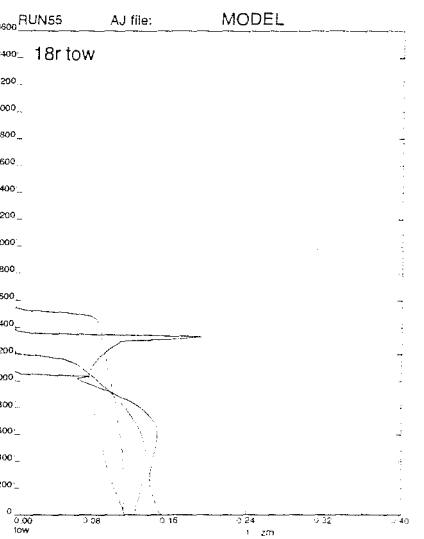
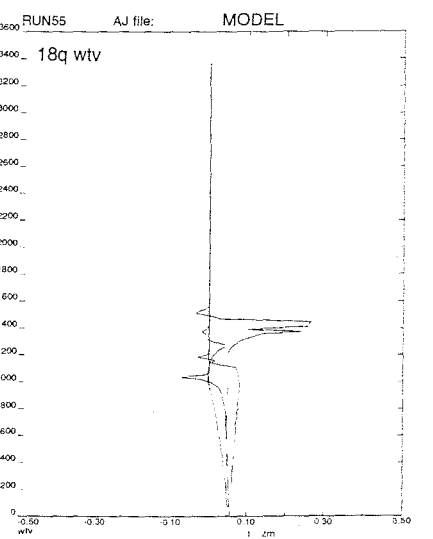
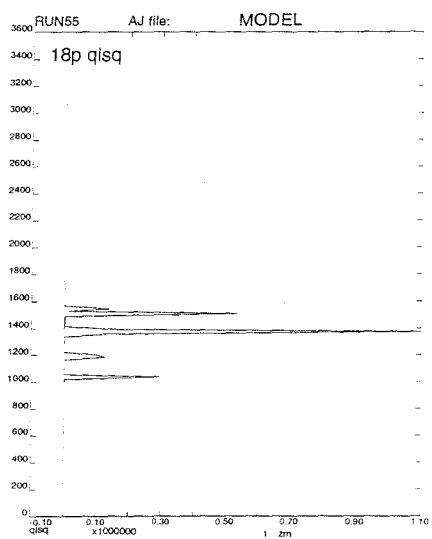
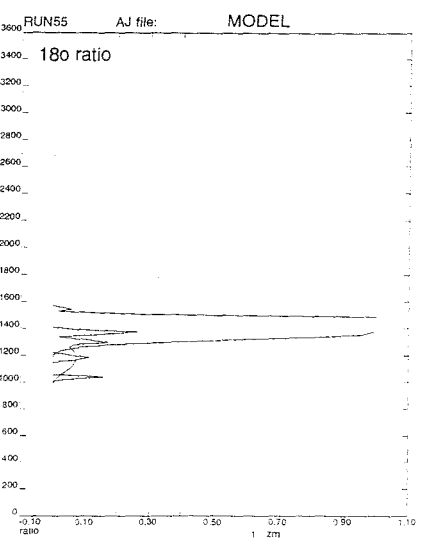
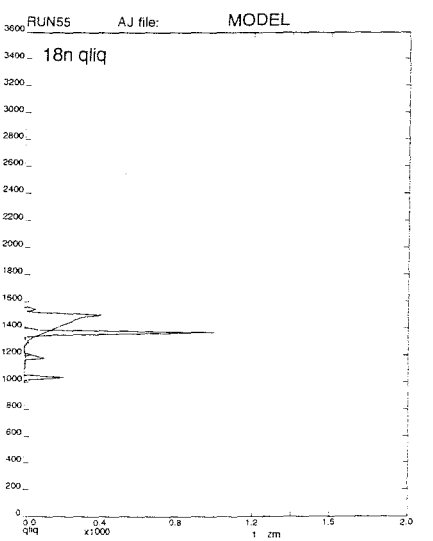
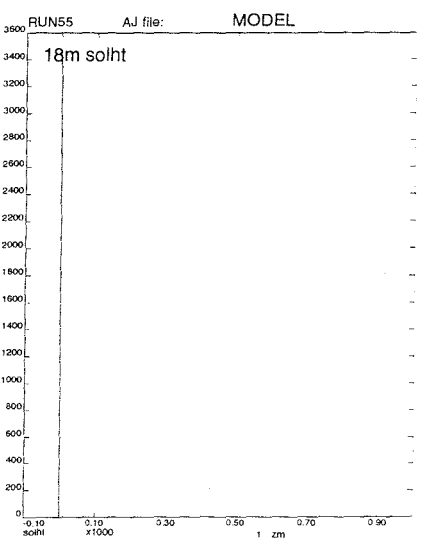
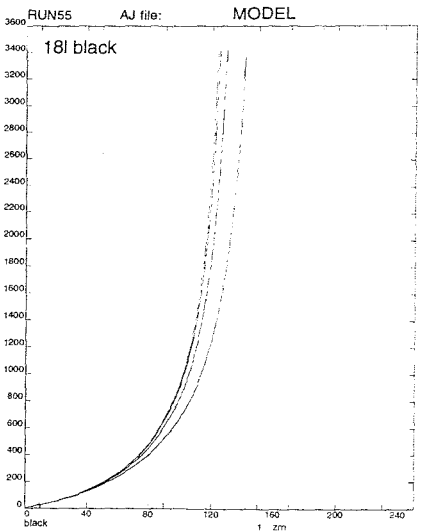
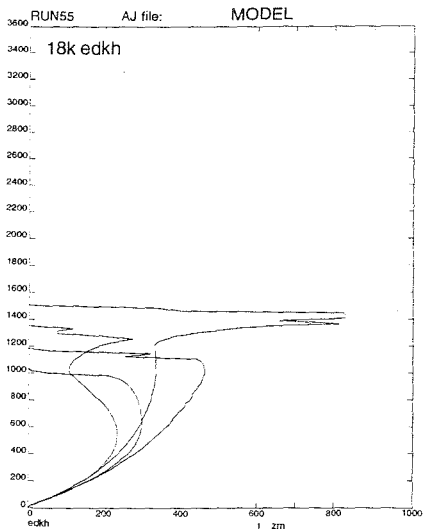
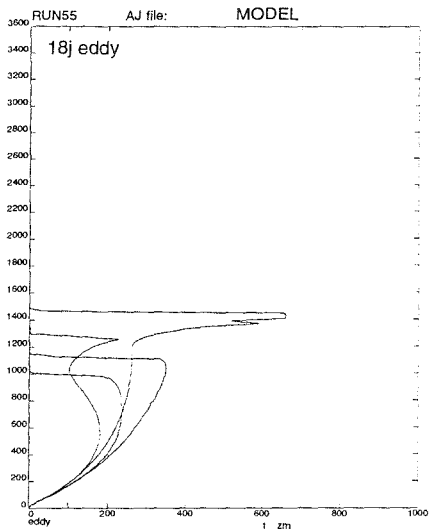
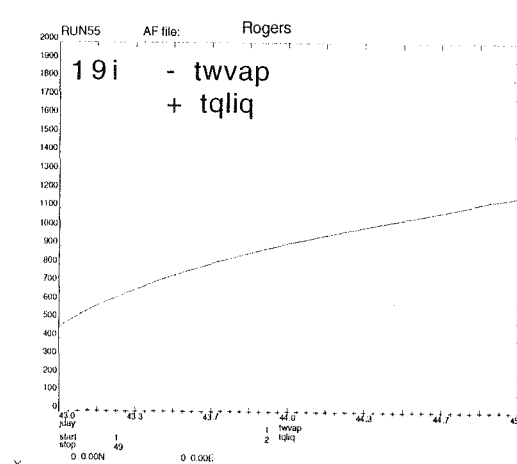
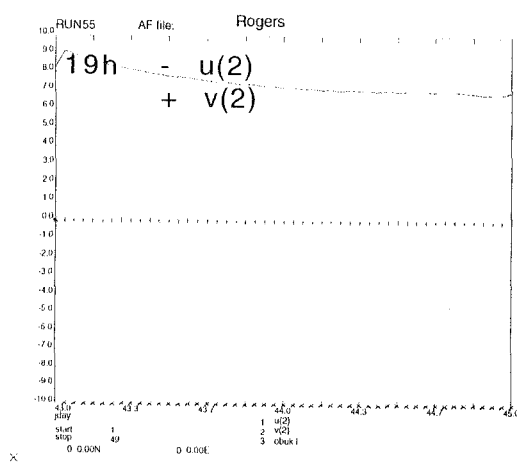
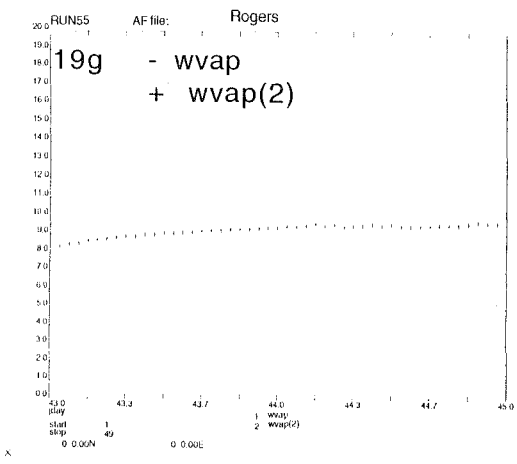
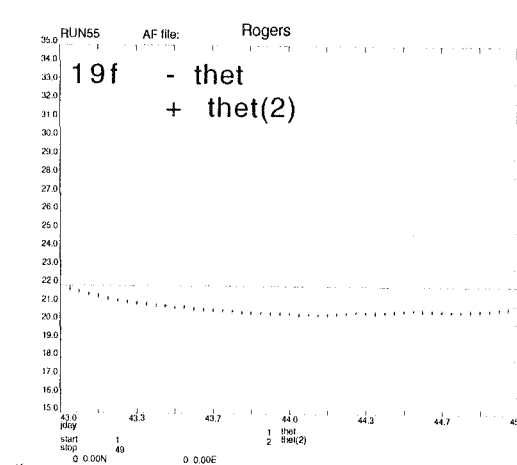
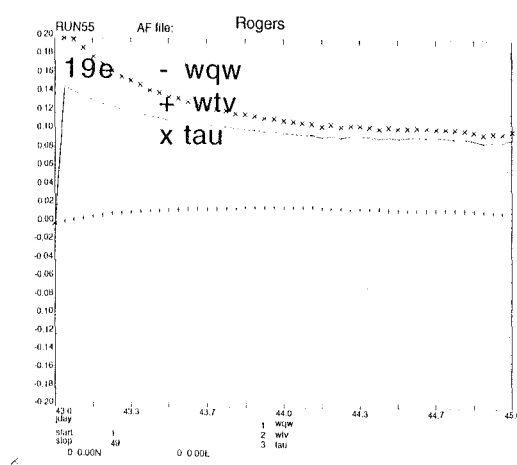
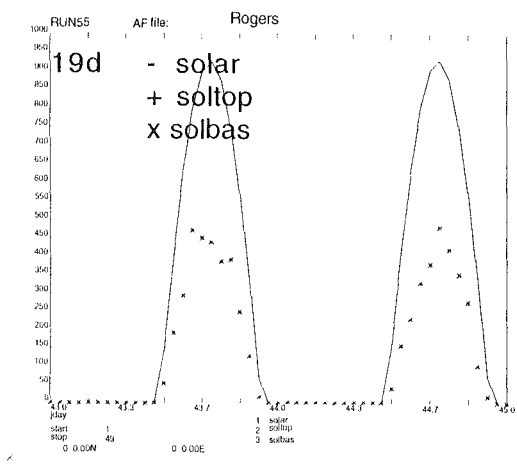
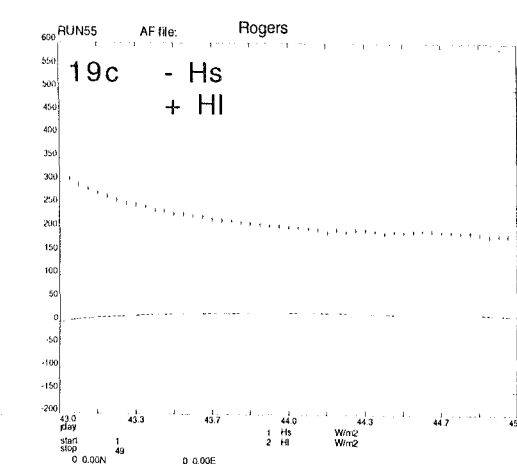
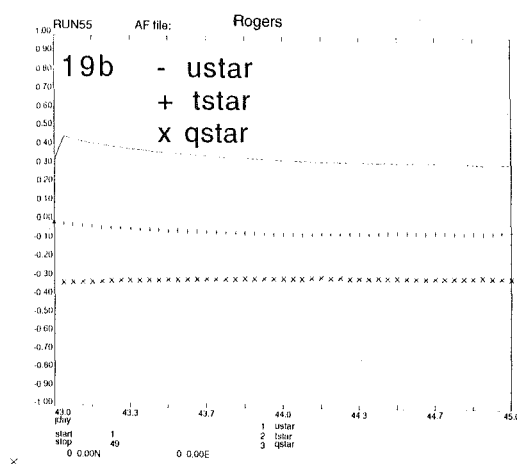
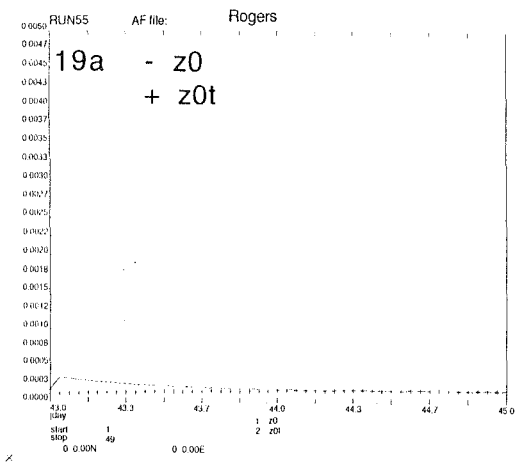
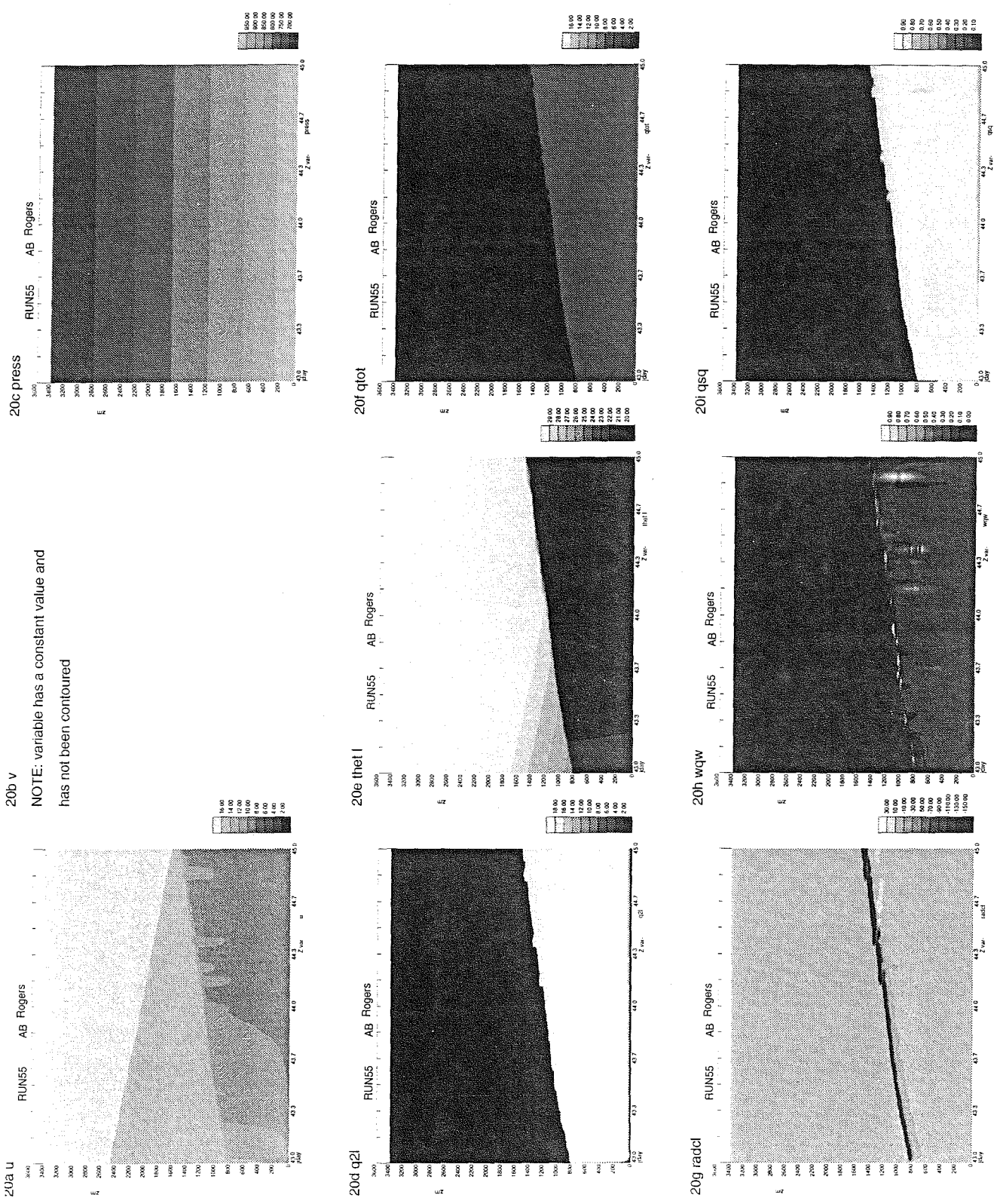


Figure 18- continued

Figure 19 - Time series of surface values for model run as in Figures 18. Table 5 gives details of the variable plotted.





NOTE: variable has a constant value and has not been contoured

Figure 20 - Contour plots of the time evolution of model parameters for run as in Figure 18. Variables plotted are similar to those in Figures 13 and 18, see text for details.

Figure 20 - continued

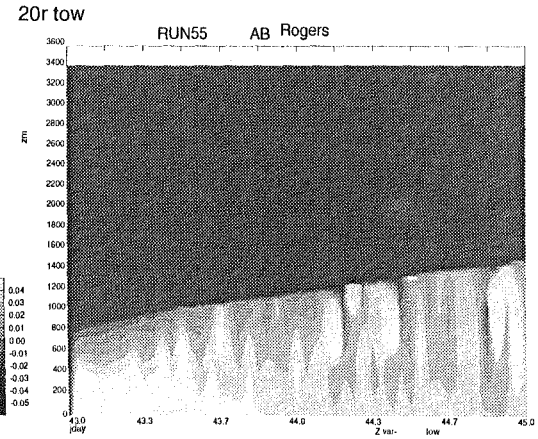
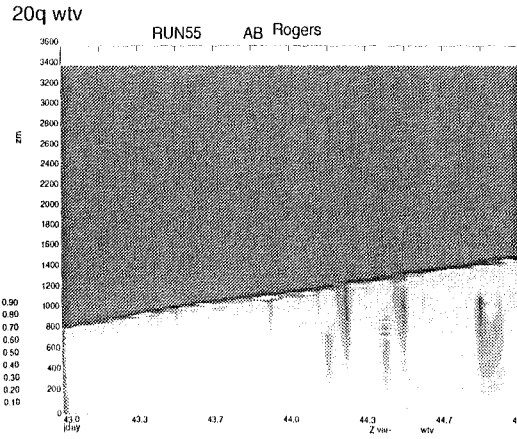
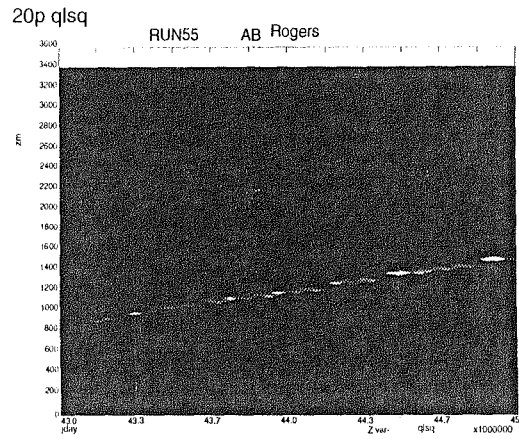
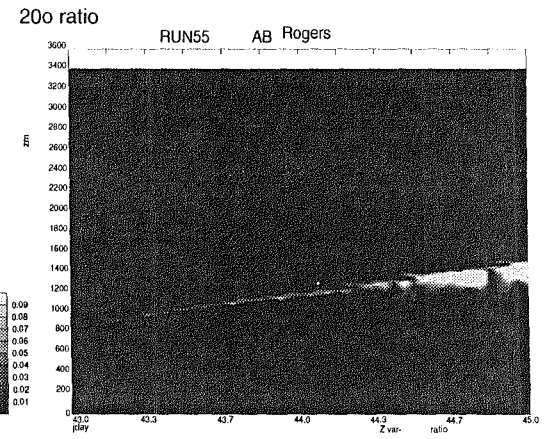
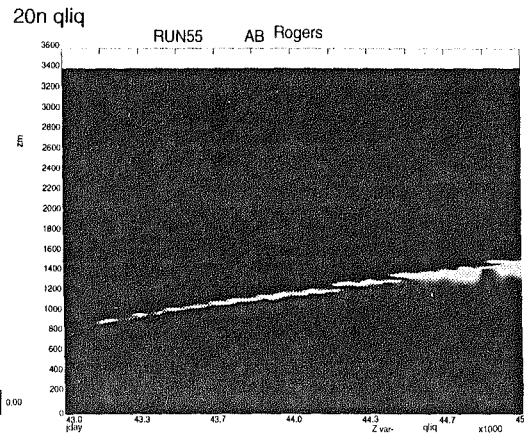
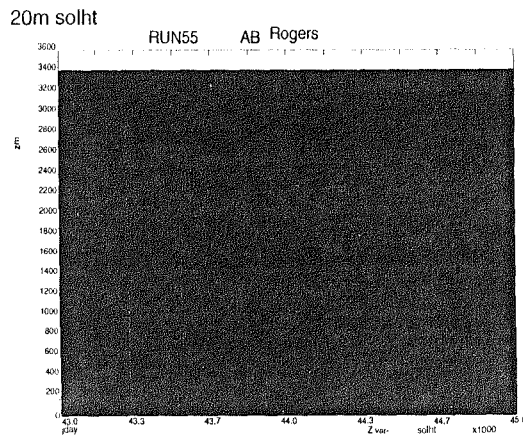
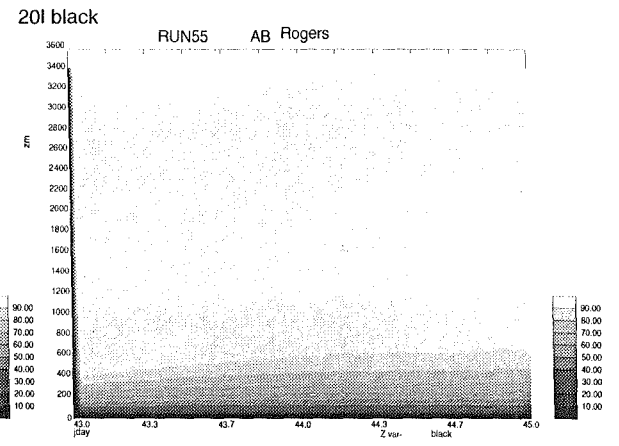
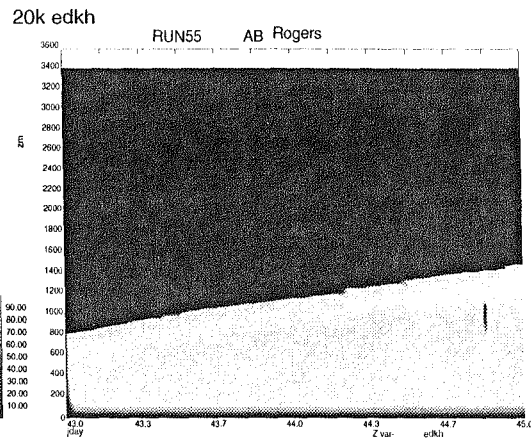
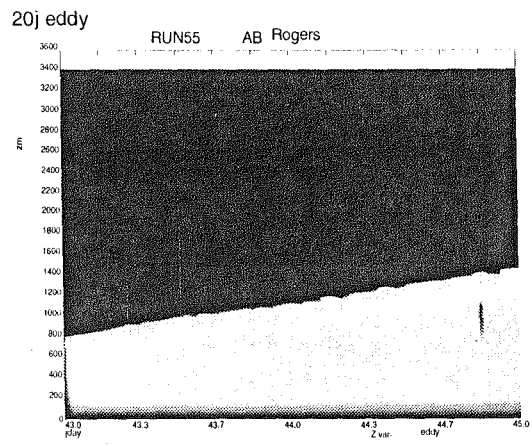
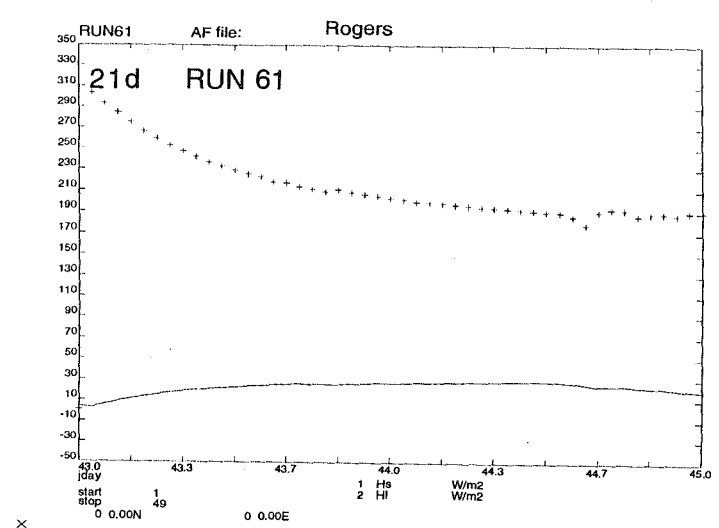
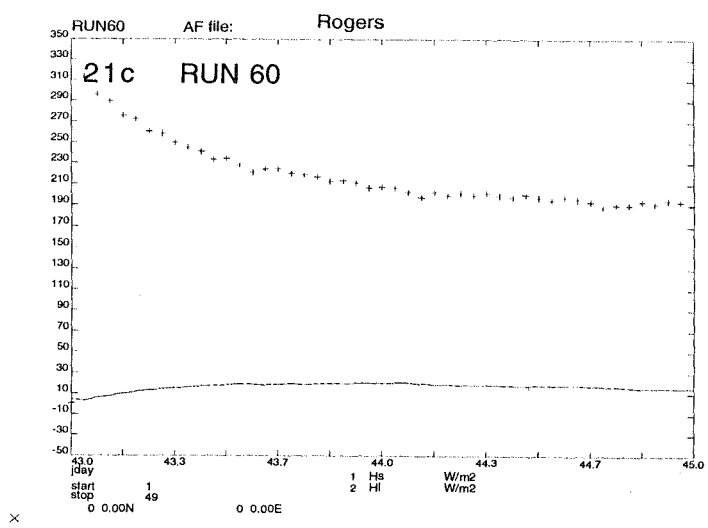
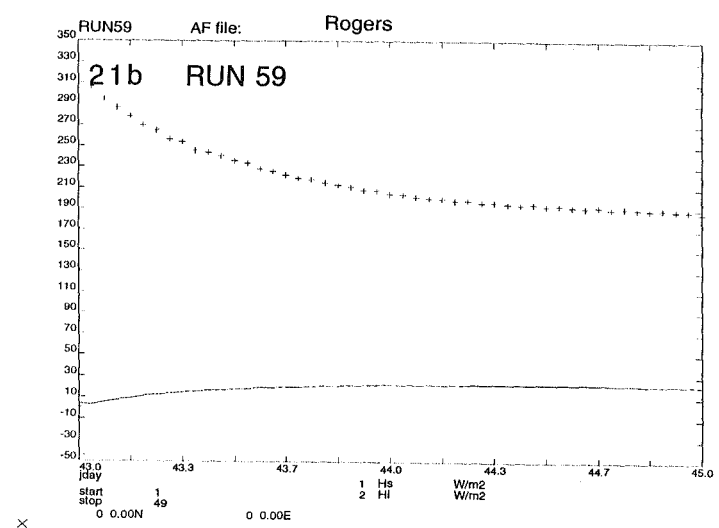
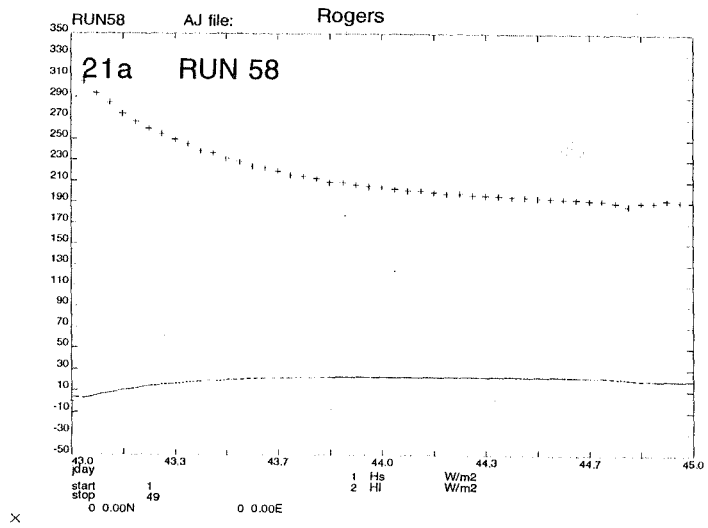


Figure 21 - Time series of surface fluxes of sensible (solid line) and latent (crosses) heat in  $W/m^2$ . (a) RUN 58 (b) RUN 59 (c) RUN 60 and (d) RUN 61.



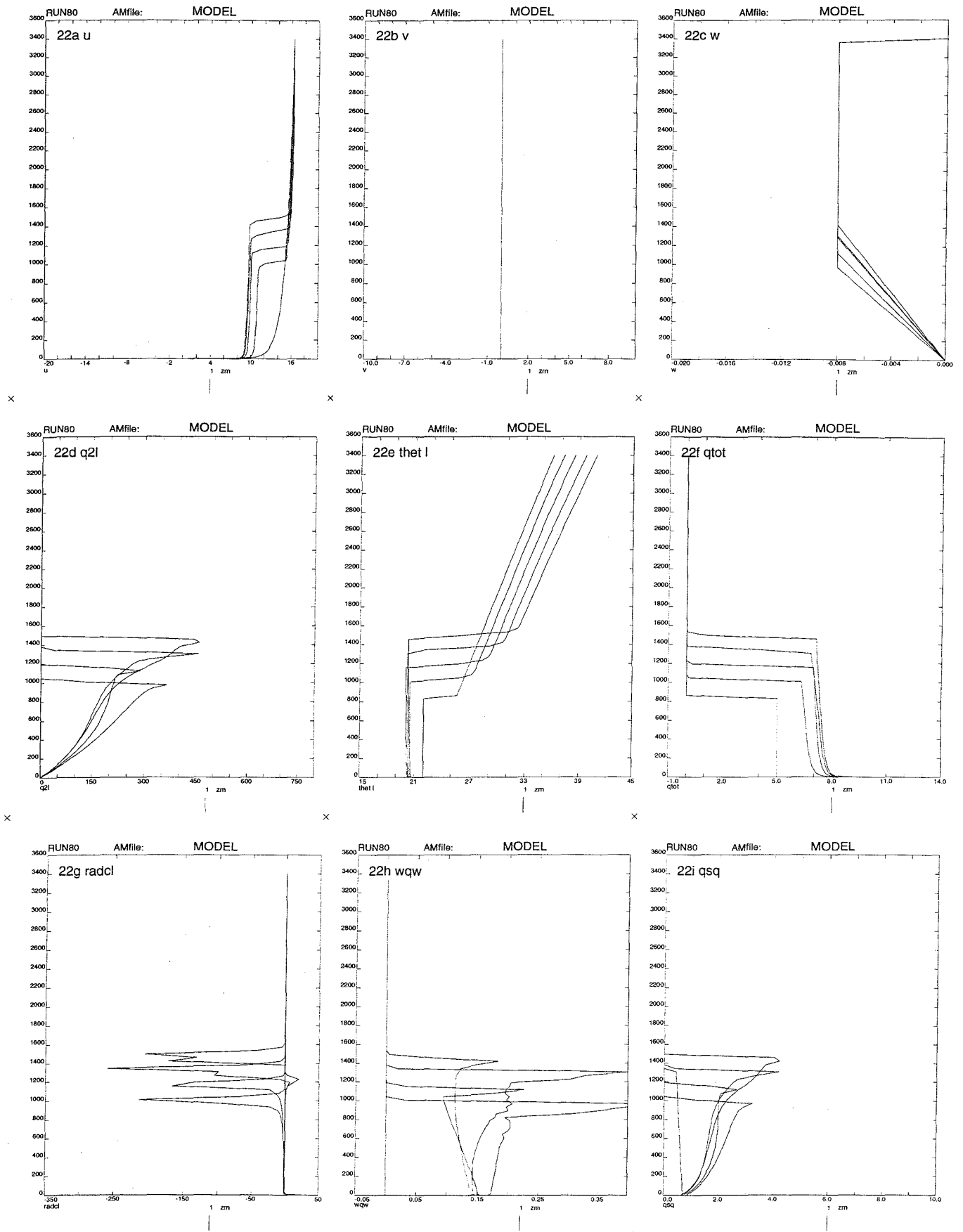


Figure 22 - Model profiles as Figure 18 but for averaged output, see text for details.

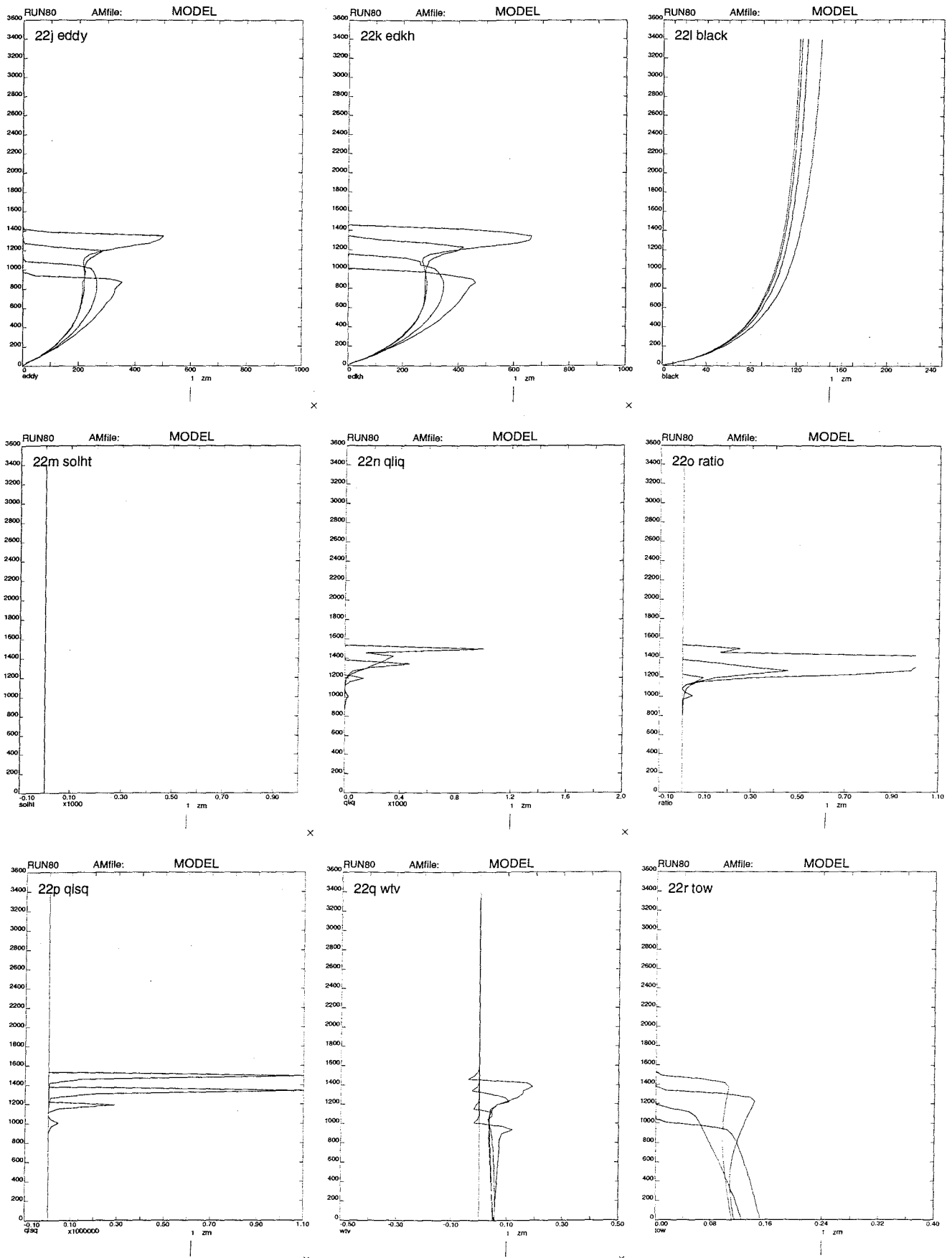


Figure 22 - continued

Figure 23 Time series of surface variables as Figure 19 but for averaged output. Error bars represent the standard error of the mean.

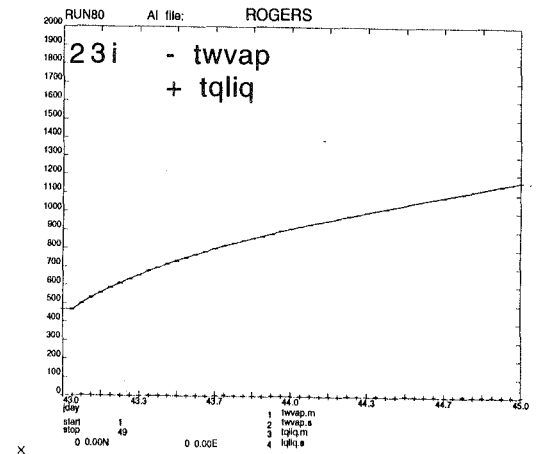
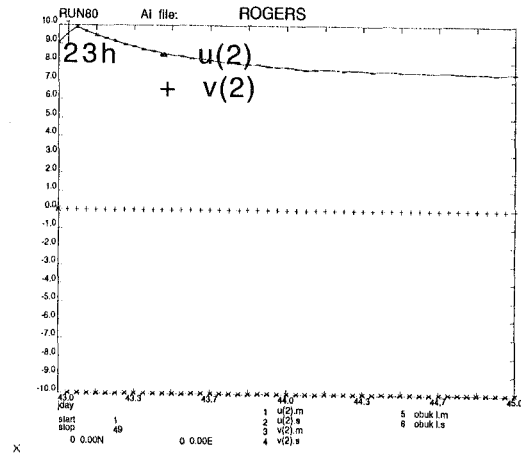
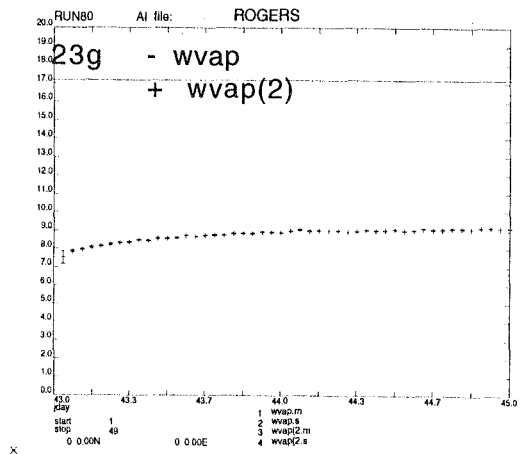
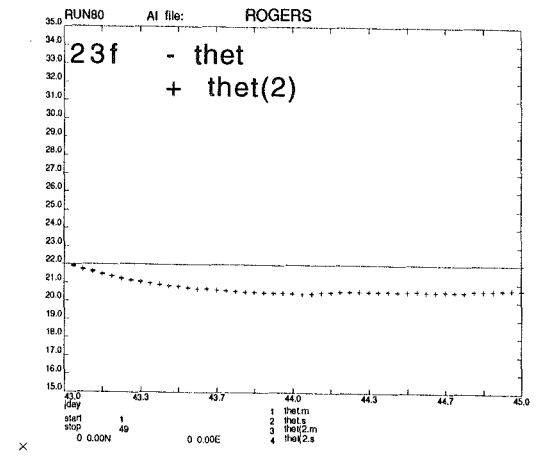
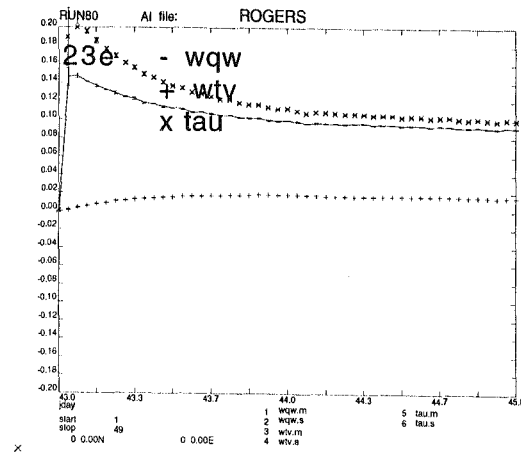
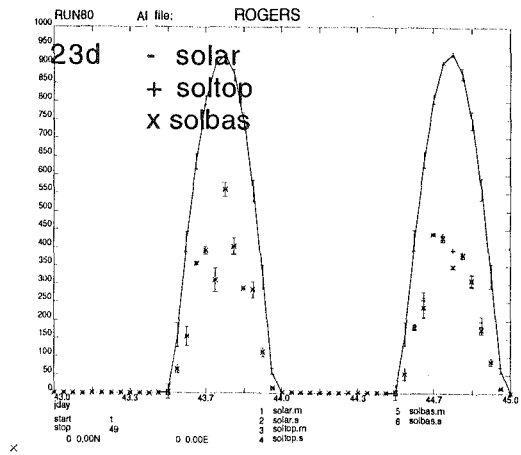
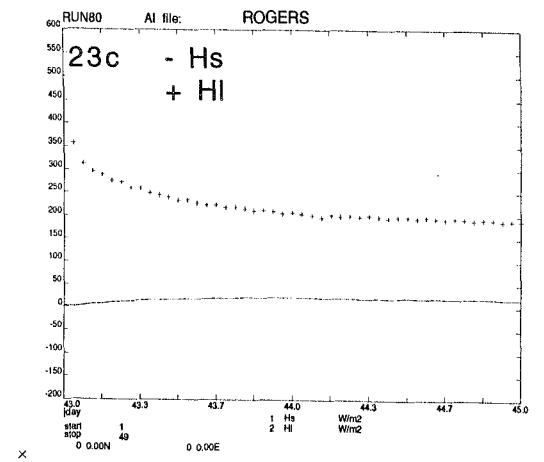
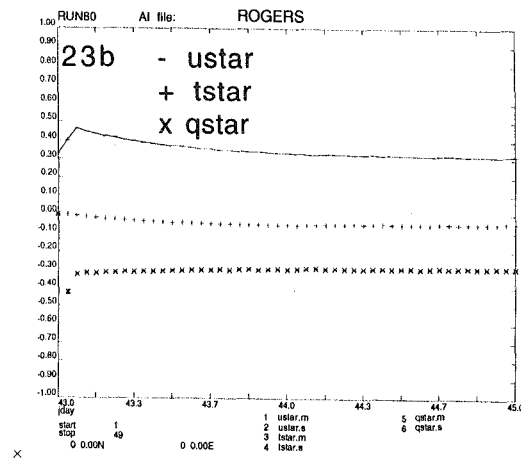
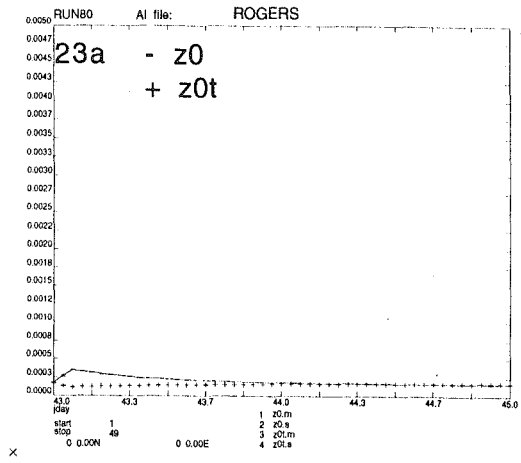
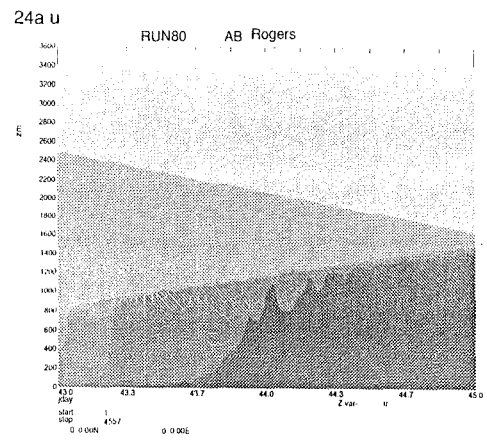


Figure 24 - As Figure 20 but for averaged output.



24b v

NOTE: variable has a constant value and has not been contoured

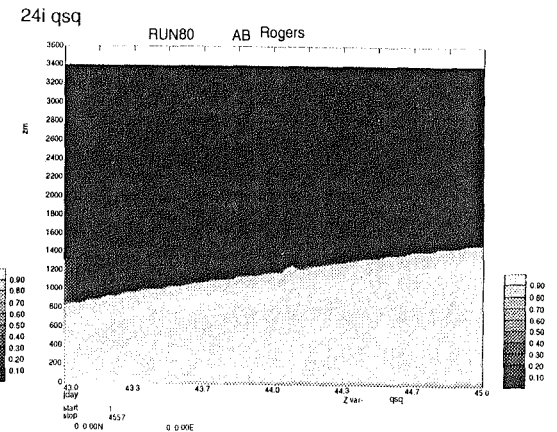
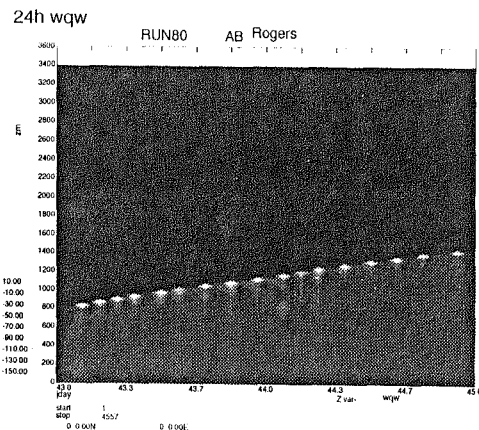
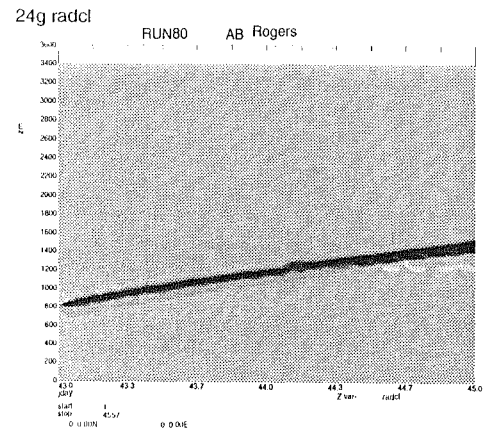
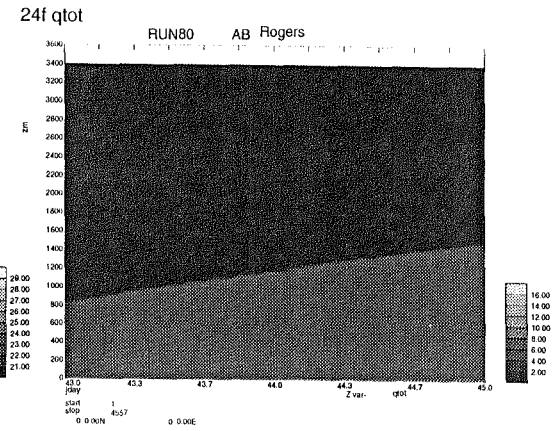
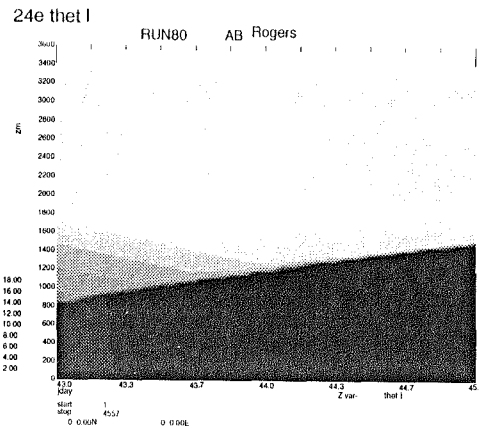
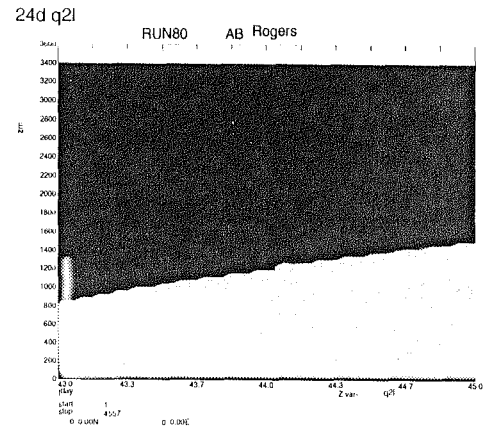
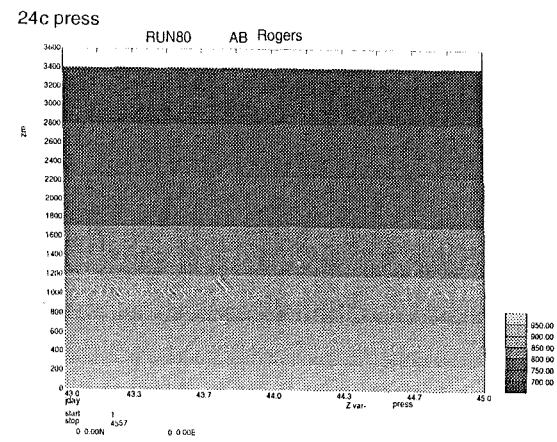


Figure 24 - continued

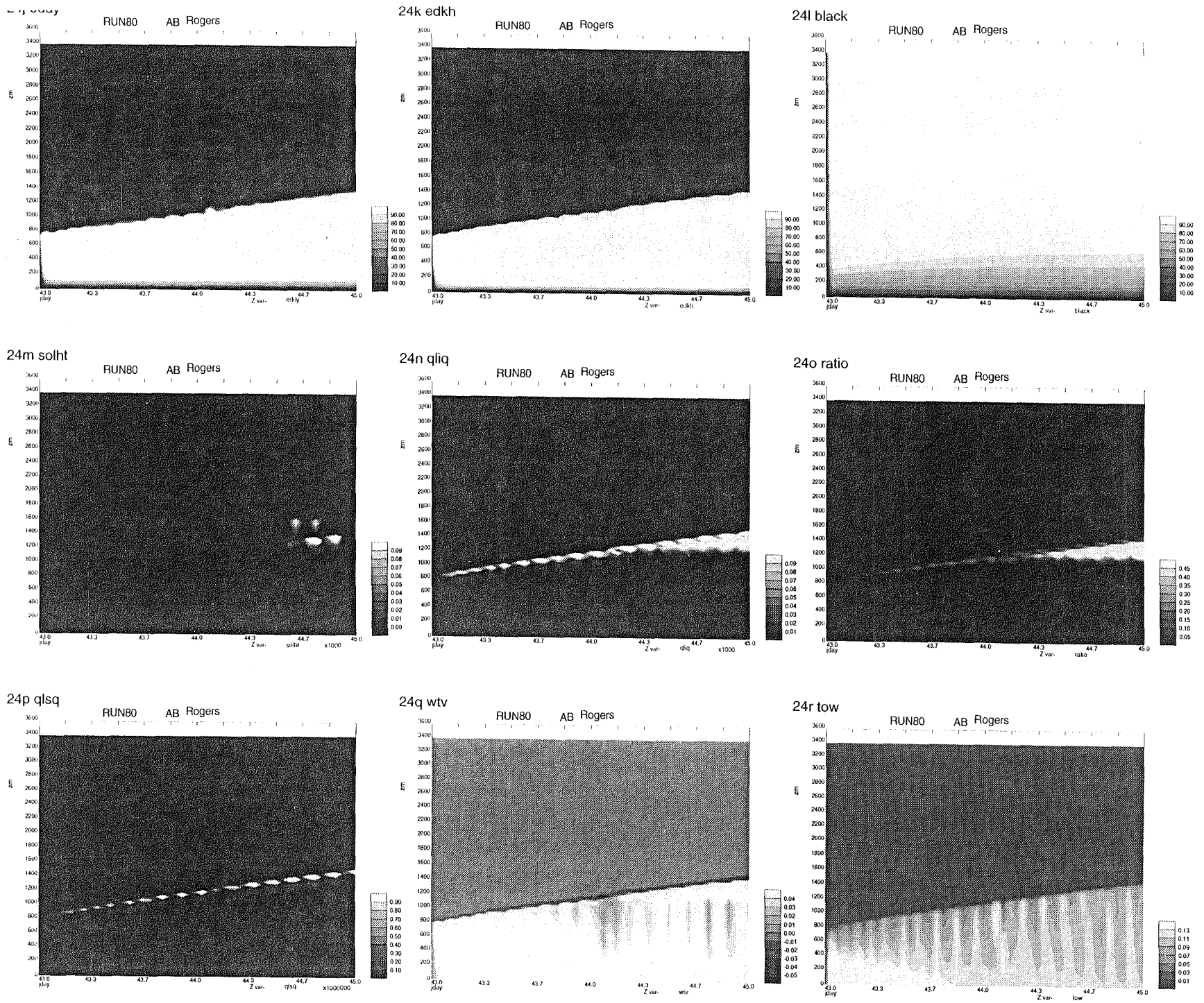
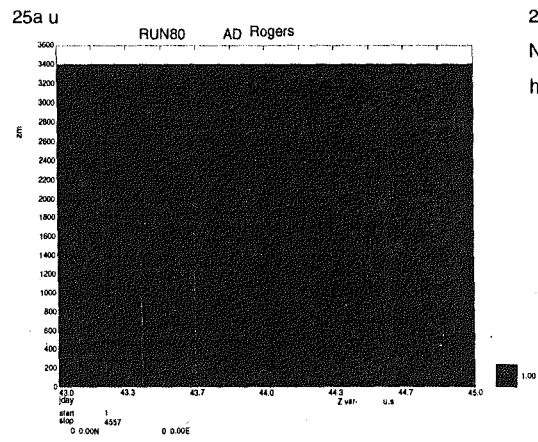


Figure 25 - Standard deviation of variables as in Figure 24.



25b v

NOTE: variable has a constant value and has not been contoured

25c press

NOTE: variable has a constant value and has not been contoured

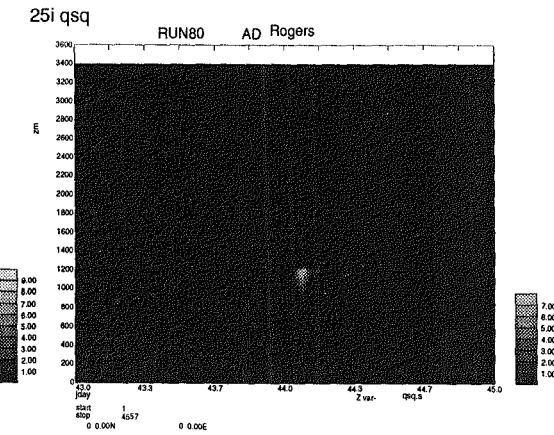
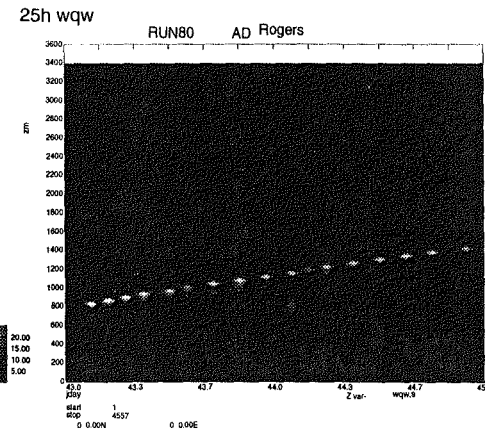
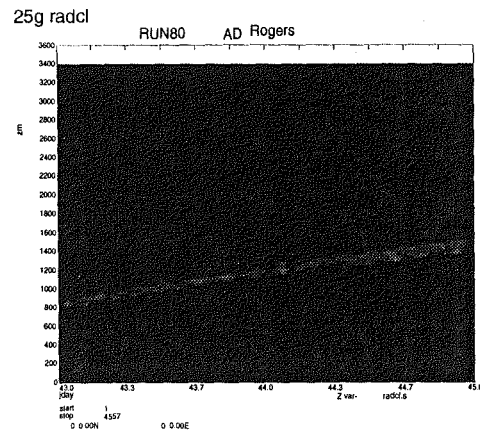
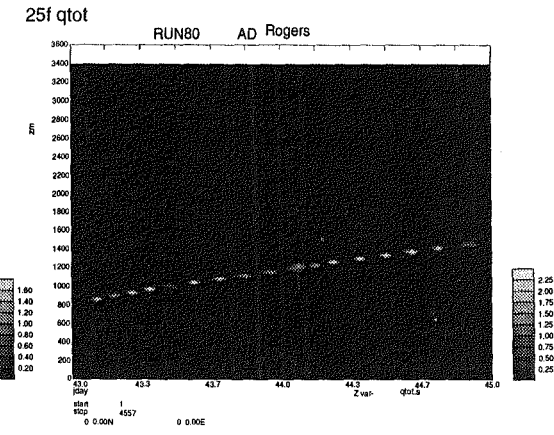
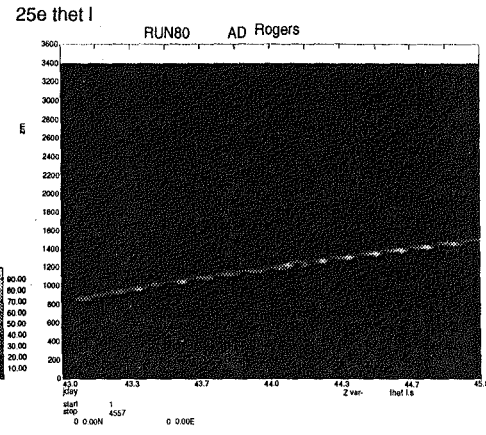
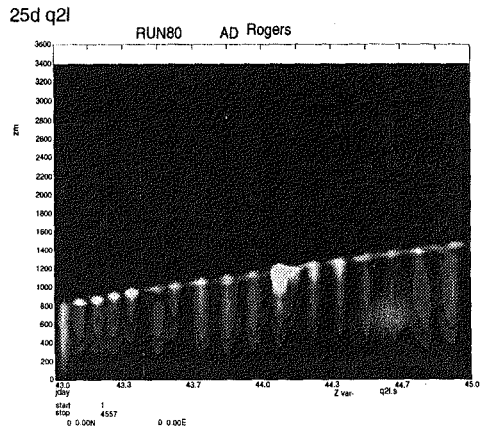
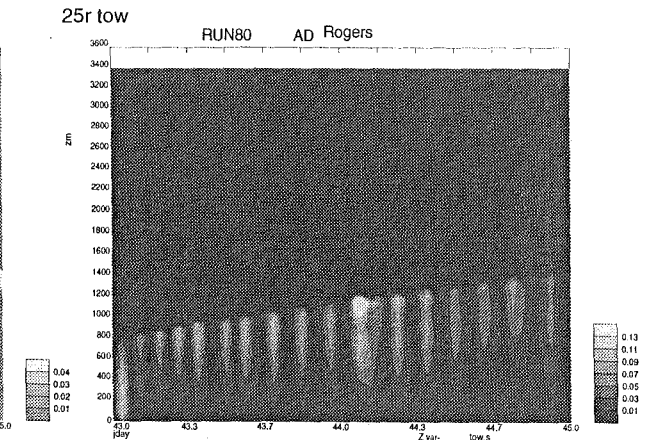
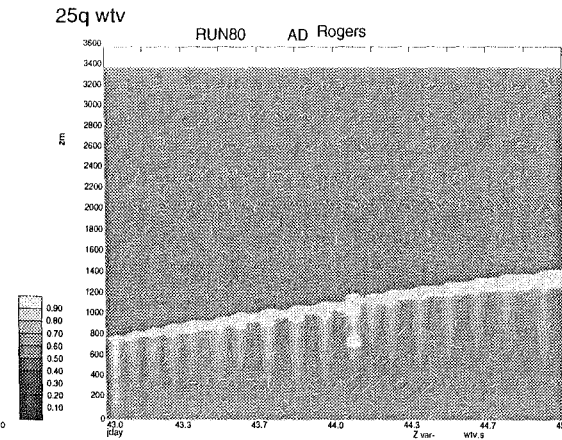
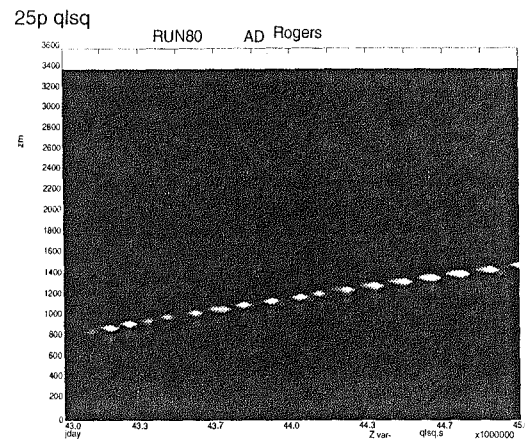
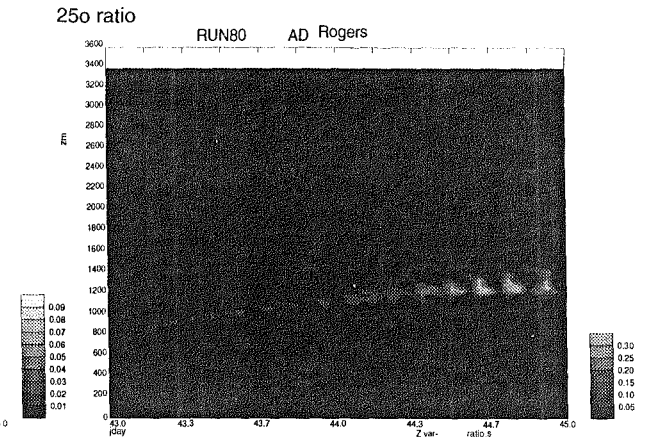
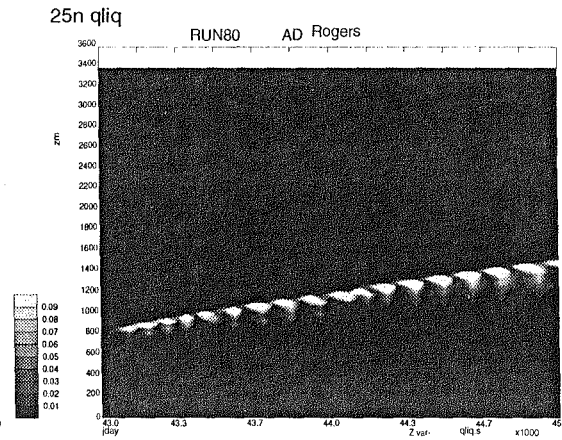
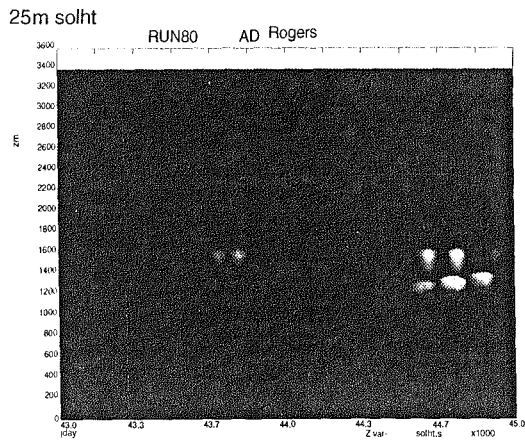
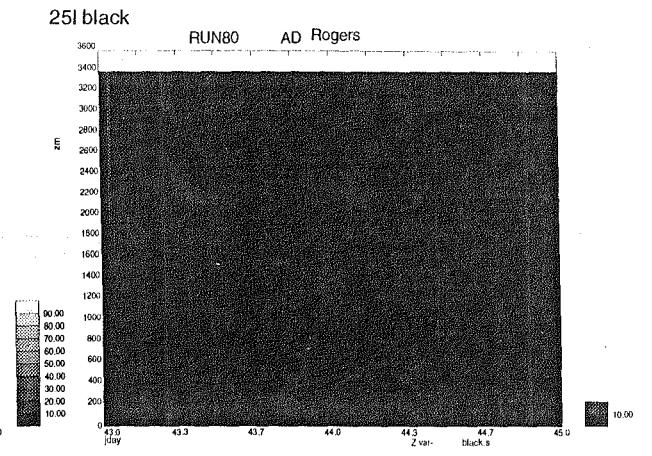
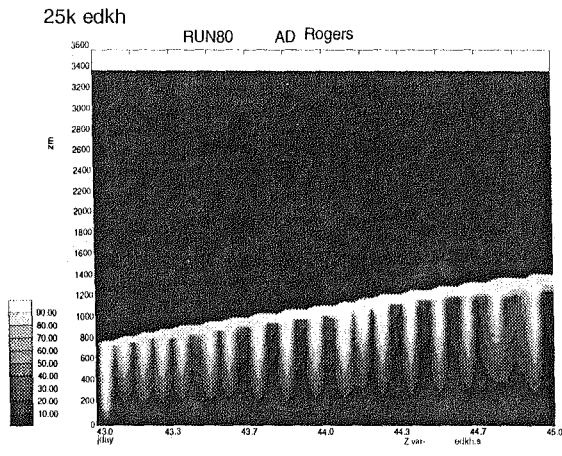
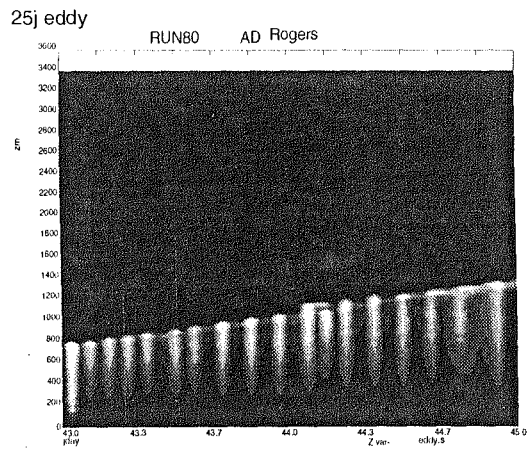


Figure 25 - continued



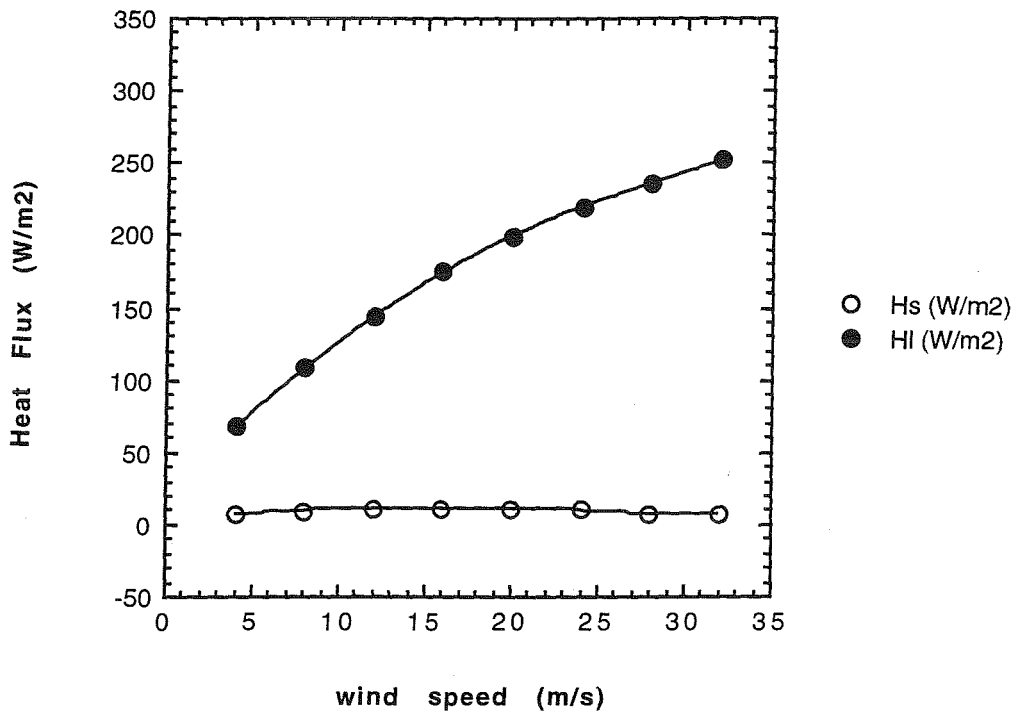


Figure 26a Variation of sensible heat flux (open circles) and latent heat flux (dark circles) in  $W/m^2$  with model wind speed in m/s.

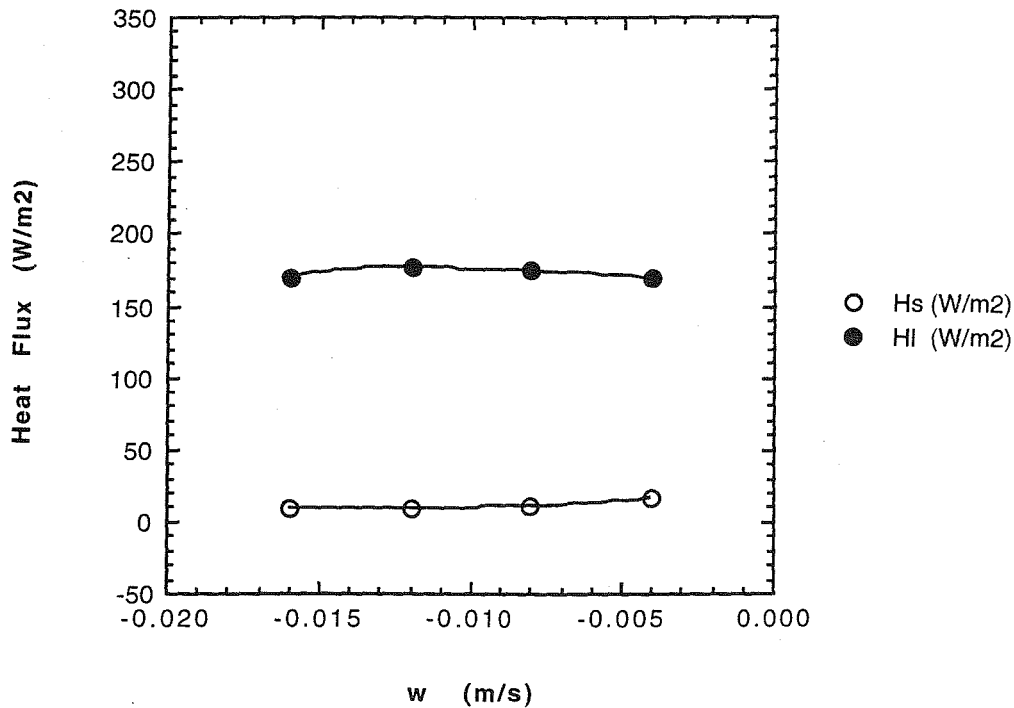


Figure 26b Variation of sensible heat flux (open circles) and latent heat flux (dark circles) in  $W/m^2$  with model vertical wind speed in m/s.

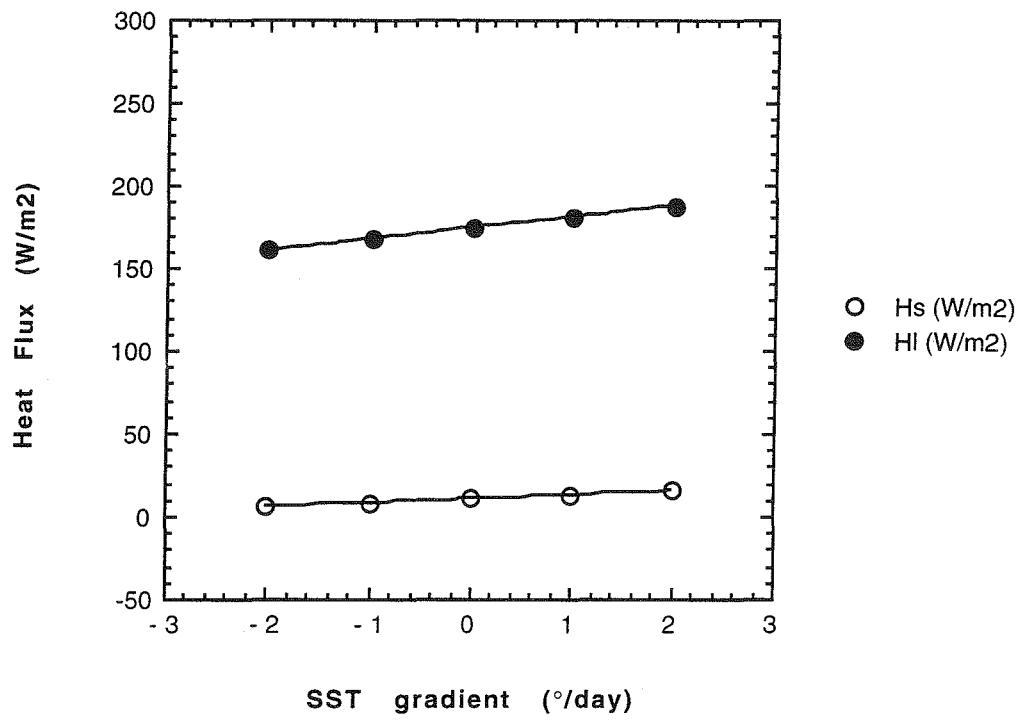


Figure 26c Variation of sensible heat flux (open circles) and latent heat flux (dark circles) in  $W/m^2$  with model SST gradient in  $^{\circ}C$  per day.

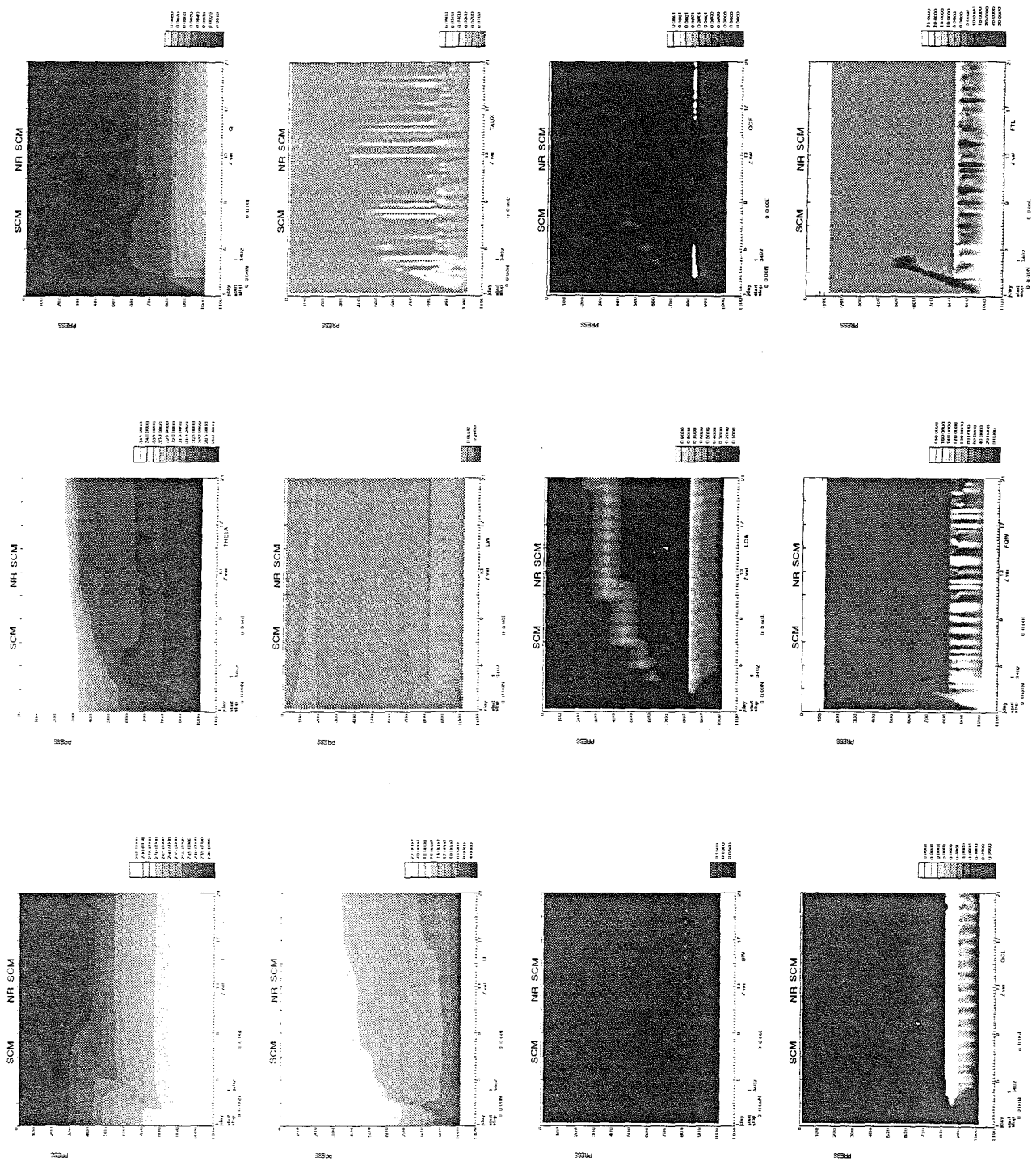


Figure 27a - Contour plots (day number, x-axis; -pressure, y-axis) of time evolution of SCM. Plots are from left to right; (top row) temperature,  $\theta$ , water vapour, (2nd row) wind speed, longwave cooling, wind stress, (3rd row) shortwave heating, cloud fraction, cloud ice content, (bottom row) cloud water content, latent heat flux and sensible heat flux.

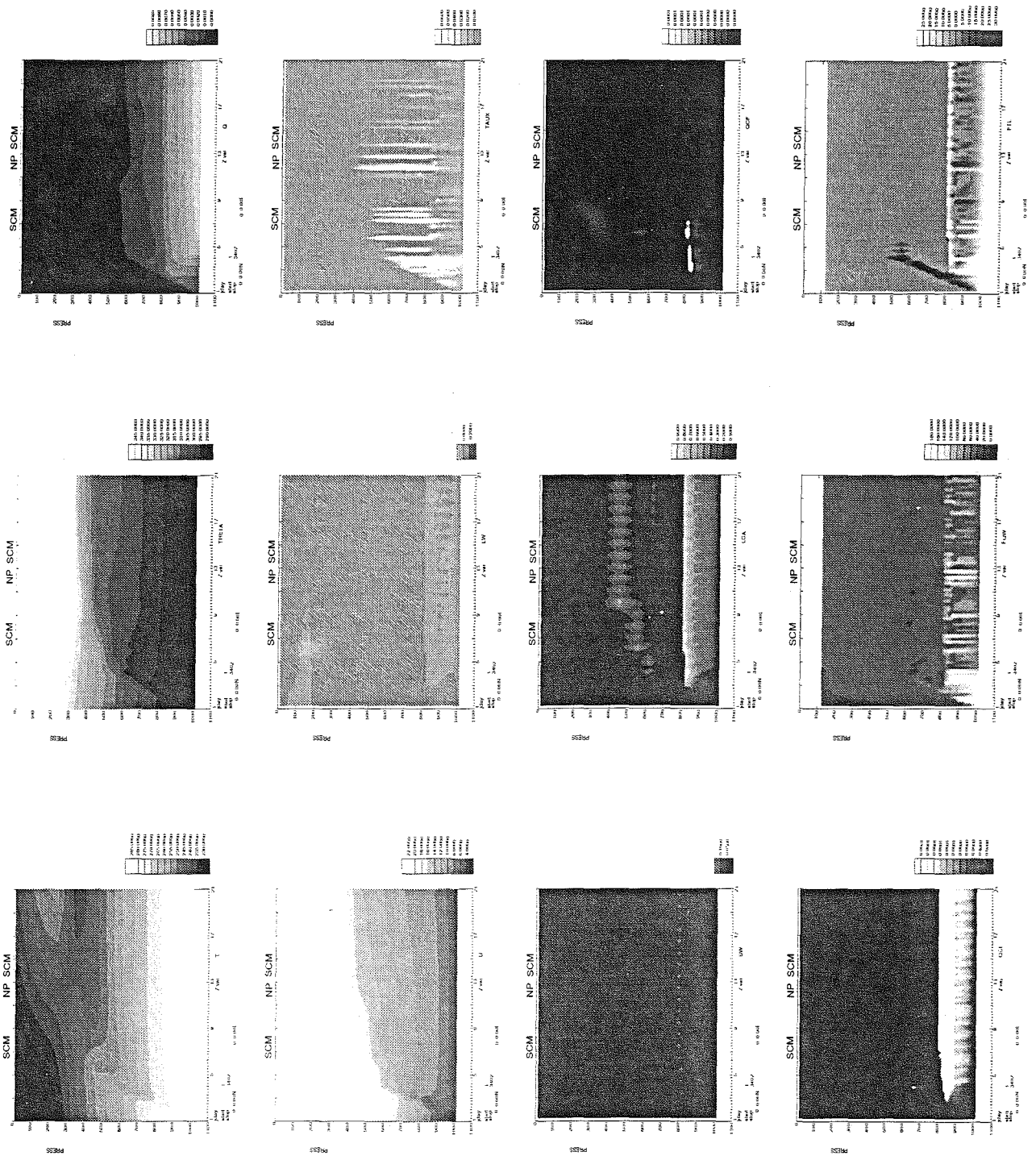


Figure 27b - As Figure 27a but with simulated vertical motion.  
 $w_{max} = 0.0006\text{m/s}$ .

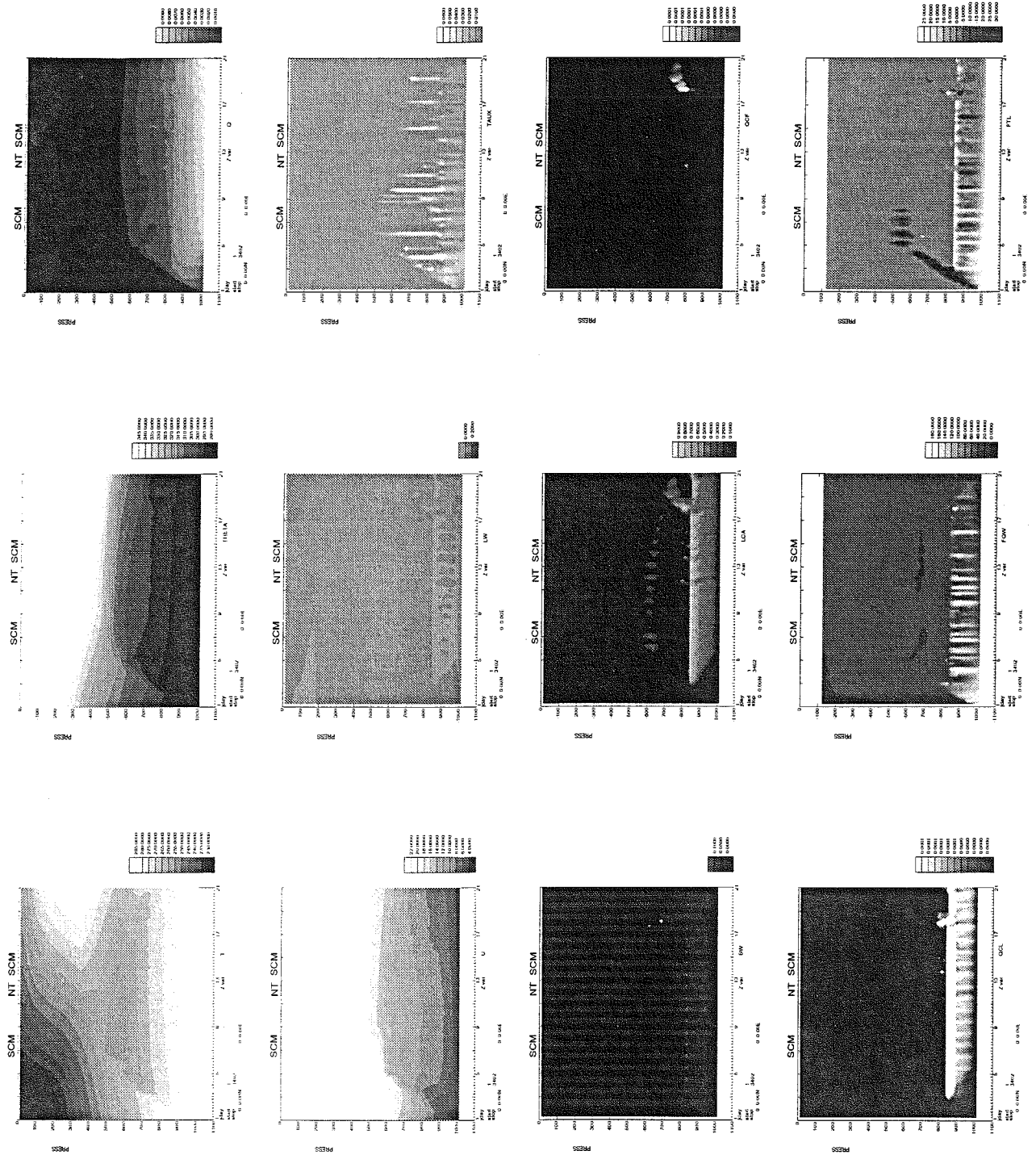


Figure 27c - As Figure 27a but with simulated vertical motion.  
 $w_{max} = 0.0012m/s.$

